LASER SPECTROSCOPY OF Eu CENTRES IN MBE GROWN CaF_2:Eu-CdF_2 SUPERLATTICES AND CaF_2:Eu THIN FILMS

A thesis

submitted in partial fulfilment

of the requirements for the Degree

of

Doctor of Philosophy

in

Physics

in the

University of Canterbury

by

Joon Koo Choi

University of Canterbury

2009

Light is sweet,

Ecclesiastes 11: 7

Abstract

Molecular beam epitaxy (MBE) grown CaF_2-CdF_2 superlattices (SLs) and CaF_2 thin films doped with Eu ions were investigated by laser spectroscopic techniques. Eu ions were selectively doped into CaF_2 layers and were used as an optical probe to the SLs and thin films. Physical properties of the SLs and thin films were inferred from optical transitions of divalent and trivalent Eu centres.

The $4f^6 5d \rightarrow 4f^7$ transition of Eu^{2+} has shown strain dependent peak shifts of the zero phonon line. These shifts were thought to be a result of deformation in the crystal structure primarily due to the lattice mismatch with the Si substrate. Based on the amount of shifts, the strains associated with the MBE samples were calculated.

Photoluminescence (PL) bleaching and its recovery of the same transition of Eu^{2+} in SLs were also explored. At low temperature the bleaching is best described as bi-exponential decay. Localisation of the liberated electrons from the $4f^6 5d$ absorption band was considered for the bleaching effect. It was observed that at elevated temperatures the PL intensity of the $4f^6 5d \rightarrow 4f^7$ transition was recovered.

Combined excitation-emission spectroscopy (CEES) was employed to investigate trivalent Eu centres in SLs. The strong $^7F_0 \rightarrow {}^5D_1$ excitation and the $^5D_0 \rightarrow {}^7F_1$ emission of Eu^{3+} were studied. A novel centre, which is assigned as I, of Eu^{3+} in SL was observed and investigated in comparison with the cubic centre (O centre) of Eu^{3+}. Relative to the O centre the I centre has shown a strong thickness dependent PL which can be demonstrated with a mono layer (1 ML = 3.15 Å) resolution. Possible transformation of the I centre to the O centre was also observed by additional thermal and UV excitations. The I and the O centres are proposed as the same centre except for having an electron in the vicinity of the I centre.

Acknowledgements

I would like to especially thank my supervisor Prof. Roger J. Reeves for his guidance and the abundant knowledge and skills he demonstrated throughout the past four years. Many thanks go to Dr. Sergey V. Gastev for his collaboration, guidance and help toward this topic. I would also like to thank his group for putting enormous effort on making the best quality films. I am also grateful to Prof. Kurt R. Hoffman, for his interest from the beginning and the useful discussion during his visit. I wish to thank Assoc. Prof. Mike F. Reid for his help on the crystal field calculation. I am grateful to Prof. Rod Syme for proofreading my drafts and indepth discussions on the topic. I also thank Alistair Lightfoot for the unofficial English lessons.

The technical staff of this department has provided tremendous assistance on the project. I would like to thank Wayne Smith, Geoff Graham, Graeme McDonald, Stephen Hemmingsen, Bob Flygenring and Russell Gillard (Chemistry) for their efforts to run the lab.

Thanks to the laser physics group for breaking up the tedium of research life; Ian Farrell: *Go raibh maith agat*, Masaed Almatori:شكرا, Song: 고마워, Martin Henseler: *Vielen dank* and to Paul Miller and Rueben Mandelsburg: Cheers mate!

Department of Physics and Astronomy and the MacDiarmid Institute for Advanced Materials and Nanotechnology are gratefully acknowledged for providing scholarships for this project.

I would like to thank my family for their support, care and cheering for the past four years. Members of CKC are very much appreciated for their loving care and support. Finally I would like to thank Jieun, my wife for her support and understanding for the journey that I pursue.

Contents

Abstract ii
Acknowledgements iii
List of figures vii
List of tables xi

Chapter 1 Introduction
1.1 Thin films of CaF_2 and superlattices of CaF_2-CdF_2 host 1
1.2 The Lanthanoids 4
1.3 Outline 6

Chapter 2 Theory 10
2.1 Introduction 10
2.2 The free-ion Hamiltonian 10
2.3 Crystal field Hamiltonian 11
2.3.1 Irreducible representations and multiplet identifications 15
2.4 Transition and polarisation selection rules 20

Chapter 3 Experimental consideration 24
3.1 MBE grown samples 24
3.2 Combined excitation-emission spectroscopy 26
3.2.1 Dye laser 26
3.2.2 CCD equipped spectrometer 26
3.2.3 Data acquisition 28
3.3 Cryogenics 29

Chapter 4 Spectroscopy of divalent Eu in CaF_2 thin films and CaF_2-CdF_2 superlattices.....30
4.1 Introduction.....30
4.2 The *f-d* transition of Eu^{2+} associated with planar strain CaF_2:Eu thin films and CaF_2:Eu-CdF_2 superlattices.....31
4.3 Photoluminescence bleaching of Eu^{2+} in CaF_2:Eu-CdF_2 superlattices and CaF_2:Eu thin films.....38
4.4 Transformation of Eu^{2+} to Eu^{3+}.....48
4.5 Recovery of Eu^{2+} by thermal excitation.....56

Chapter 5 Spectroscopy of trivalent Eu centres in symmetric CaF_2:Eu-CdF_2 superlattices.....65
5.1 Introduction.....65
5.1.1 Previous work.....66
5.2 Discussion of CEES results for Eu^{3+} centres in symmetric superlattices.....69
5.2.1 Symmetry assignments of Eu^{3+} centres in symmetric CaF_2:Eu-CdF_2 superlattices.....70
5.2.2 Thickness dependence of Eu^{3+} centres inCaF_2:Eu-CdF_2 superlattices.....82
5.2.3 Temperature dependence of Eu^{3+} PL in CaF_2:Eu-CdF_2 superlattices.....87
5.2.4 PL behaviour of Eu^{3+} centres under additional UV excitation.....97
5.3 Crystal field analysis.....105
5.4 Summary.....110

Chapter 6 Spectroscopy of trivalent Eu centres in asymmetric CaF_2:Eu-CdF_2 superlattices.....113
6.1 Introduction.....113
6.2 Discussion of CEES results for Eu^{3+} centres in asymmetric superlattices.....114
6.2.1 Temperature dependence of Eu^{3+} PL in asymmetric CaF_2:Eu-CdF_2 superlattices.....117
6.2.2 PL behaviour of Eu^{3+} centres under additional UV excitation.....124
6.3 Summary.....128

Chapter 7 Discussion of the charge compensating electron for the novel I centre in CaF_2:Eu-CdF_2 superlattices 129
7.1 Introduction.....129
7.2 Crystal structure of the Interface centre of Eu^{3+} in CaF_2:Eu-CdF_2 superlattices 129
7.3 Absorption band for the charge compensating electron 134

Chapter 8 Conclusion.....141
8.1 Summary of results 141
8.2 Future work 143

Appendix: Publications.....145

List of figures

1.1 Schematic of band gaps of CaF_2 and CdF_2 3
1.1 Schematic of charge compensation by F ions 5
2.1 Schematic of the splitting for the 4*f* electronic configuration 12
2.2 The symmetry of a C_{3v} centre with the principle axis (*z*) pointing out of the page through the centre of the inner triangle 15
2.3 Energy level splitting and its assignment for Eu^{3+} in C_{3v} symmetry centre 20
3.1 Schematic of CaF_2:Eu-CdF_2 deposition. Eu ions are uniformly deposited in the CaF_2 layers 25
3.2 Energy levels of the Eu^{3+} inside the band gap of CaF_2. 27
3.3 A contour plot of CEES for Eu^{3+} in a SL. Corresponding Eu^{3+} centres are indicated by contours 28
4.1 Energy level diagram for the $4f^7 \rightarrow 4f^6 5d$ transitions of Eu^{2+}. 33
4.2 The PL spectrum of Eu^{2+} doped in a CaF_2:Eu bulk crystal with a He-Cd laser as the excitation source 33
4.3 Normalised ZPL photoluminescence peaks of Eu^{2+} doped in (a) bulk crystal, (b) a CaF_2:Eu-CdF_2 SL, (c) a 290 nm thick CaF_2:Eu film and (d) a 70 nm thick CaF_2:Eu film 34
4.4 Splitting in the ZPL of Eu^{2+} in a 650 nm thick film (TF 1683). 36
4.5 Schematic of polarised emission set up 36
4.6 Polarised emission of the ZPLs of Eu^{2+} in a 650 thick film of CaF_2:Eu (TF1683) ... 37
4.7 Schematic of the excited state of Eu^{2+} in CaF_2.. 39
4.8 PL spectra of Eu^{2+} and Eu^{3+} in a $(CaF_2{:}Eu)_{20}$-$(CdF_2)_{20}$ SL (SL1647) measured at (a) time of 0 s and at (b) time of 580 s of UV exposure 41
4.9 Normalised PL intensity of Eu^{2+} and Eu^{3+} in a $(CaF_2{:}Eu)_{20}$-$(CdF_2)_{20}$ SL (SL1647) with time of UV excitation 42
4.10 Bi-exponential fitting of Eu^{2+} decay during UV excitation for SL 1647 44
4.11 Photobleaching of Eu^{2+} selectively doped in the middle of CaF_2 layer ($CaF_{2(20)}$-$CaF_2{:}Eu_{(20)}$-$CaF_{2(20)}$)-$(CdF_2)_{(60)}$ in ISL1686 45
4.12 Photobleaching of Eu^{2+} in a thin film (1975) of CaF_2. 46

4.13 Schematic of band structure of CaF_2 grown on a Si substrate 47
4.14 Exponential growth of Eu^{3+} PL in a $(CaF_2:Eu)_{20}$-$(CdF_2)_{20}$ SLs under UV laser excitation. Bi-exponential fitting was provided using equation (4.5) 49
4.15 Exponential growth of Eu^{3+} PL in a $(CaF_2:Eu)_{20}$-$(CdF_2)_{20}$ SLs under UV laser excitation. Bi-exponential fitting was provided using equation (4.6) 52
4.16 Probability diagram for ionised Eu^{2+} ions contributing to the cubic centre of Eu^{3+} .. 53
4.17 Sequential PL intensity of Eu^{2+} and Eu^{3+} in $(CaF_2:Eu)_{20}$-$(CdF_2)_{20}$ SL (SL1647) 54
4.18 Photobleaching of Eu^{2+} and PL of Eu^{3+} in a thin film of CaF_2:Eu (TF1975) 55
4.19 Photobleaching of Eu^{2+} in $(CaF_2:Eu)_{20ML}$-$(CdF_2)_{20ML}$ SL (SL1647) 59
4.20 Exponential fitting of PL growth of Eu^{2+} with temperature (SL1647). 60
4.21 Exponential fitting of PL growth of Eu^{2+} using two energy potentials 60

5.1 Contour plots of the Eu^{3+} cubic (O) centre in (a) bulk crystal, (b) 20ML thick SL and (c) 7ML thick SL. 67
5.2 Contour plot of the I and the O centres in a 3 ML thick SL 68
5.3 Contour plots of (a) CaF_2:Eu bulk crystal and (b) CaF_2:Eu-CdF_2 SL 70
5.4 Excitation and emission spectra of the tetragonal A centre in (a) bulk crystal and (b) in a SL 71
5.5 Excitation and emission spectra of the cubic O centre in (a) bulk crystal and (b) in a SL 72
5.6 Schematic (top view) of the polarisation anisotropy set up 74
5.7 Contour plots of polarised CEES on a 3 ML SL (SL 3173). 75
5.8 Energy levels and polarisation assignments for optical transitions of Eu^{3+} in cubic and C_{3v} symmetry. 76
5.9 Polarisation anisotropy of Eu^{3+} in trigonal symmetry (C_{3v}) 78
5.10 CEES of Eu^{3+} in a cubic centre in $(CaF_2:Eu)_{20}$-$(CdF_2)_{20}$ SL 80
5.11 Multi peak fitting results of the splitting of the O centre in (a) excitation and in (b) emission spectra 80
5.12 High resolution CEES of symmetric SLs with different CaF_2-CdF_2 thicknesses (a) 5ML (b) 3ML and (c) 2ML. 82
5.13 Profile of emission and excitation spectra of a 7 ML SL (SL3172) 83
5.14 Gaussian fittings of profiles of the CEES from various SLs 84
5.15 Diagram of Eu^{3+} deposition in a D ML thick SL 85

5.16 ratio between the I centre and the O centre with respect to the thickness of CaF_2-CdF_2 SLs 86
5.17 Schematics of conduction band electrons vicinity to the Eu^{3+} ions deposited at the 1^{st} and the D^{th} layers of CaF_2 88
5.18 Contour plots for a 5ML symmetric SL (SL3172) at various temperatures; (a) 4 K, (b) 60 K, (c) 100 K, (d) 160 K, (e) 180 K and (f) 240 K. 89
5.19 Multi peak fitting of the I and the O centres of Eu^{3+} in a 5ML SL (SL3172) with various temperatures. 92
5.20 Fitting of the electron delocalisation model to the experimental data 93
5.21 Multi peak fitting results for the 2 ML thick SL (SL1885) with respect to temperature 95
5.22 The PL intensity ratio of the O and the I centre of Eu^{3+} in a 2 ML thick SL 96
5.23 Contour plots of the 3 ML thick SL before, during and after additional UV excitation on top of the $^7F_0 \rightarrow {}^5D_1$excitation and the $^5D_0 \rightarrow {}^7F_1$ emission at 4 K 98
5.24 Multi peak fitting of the I and the O centres in SL 3173; (a) before, (b) during and (c) after the UV excitation 98
5.25 The PL intensity monitoring of the I and the O centres in (a) 7 ML thick SL, (b) 5 ML thick SL and (c) 3 ML SL under the influence of additional UV excitation 100
5.26 Linear fitting of decrease coefficient A with thickness D of SLs 103
5.27 PL ratio of normalised intensity of the O and the I centres during He-Cd laser excitation on top of the $^7F_0 \rightarrow {}^5D_1$ excitation and the $^5D_0 \rightarrow {}^7F_1$ emission of Eu^{3+} 103
5.28 PL behaviour of the I and the O centre of Eu^{3+} in a 2 ML thick SL (SL1885); (a) before UV excitation and (b) during UV excitation. 104
5.29 Cubic parameter mapping of the energy level calculations 108
5.30 The observed splitting of the cubic centre of Eu^{3+} in thick SLs (SL1649) 109
6.1 Profile of the I and the O centre PL intensity for (a) ASL1982 $(CaF_2{:}Eu)_2$-$(CdF_2)_4$ and (b) ASL1980 $(CaF_2{:}Eu)_4$-$(CdF_2)_2$ at ~4 K. 115
6.2 Emission profile of ASLs, (a) ASL 1982 $(CaF_2{:}Eu)_2$-$(CdF_2)_4$ and (b) ASL1980 $(CaF_2{:}Eu)_4$-$(CdF_2)_2$ 116
6.3 Linear fitting of the PL intensity ratio of the O and the I centres with respect to the thickness of CaF_2 layers according to (5.2) 118

6.4 CEES of the I centre in ASL 1979 $(CaF_2:Eu)_2$-$(CdF_2)_4$ in the temperature ranges between 4 to 240 K 119
6.5 CEES of the I and the O centres in ASL 1980 $(CaF_2:Eu)_4$-$(CdF_2)_2$ in the temperature range 4 to 240 K..... 120
6.6 The PL intensity ratio of the O and the I centres with respect to temperature for ASL1979 $(CaF_2:Eu)_2$-$(CdF_2)_4$..... 121
6.7 The PL intensity ratio of the O and the I centres with respect to temperature for ASL1980 $(CaF_2:Eu)_4$-$(CdF_2)_2$. 122
6.8 Calculated PL intensity ratios of the O and the I centres in (a) ASL1979, (b) SL1885, (c) ASL1980, (d) SL3173 and (e) SL3172..... 123
6.9 CEES of ASL1982 $(CaF_2:Eu)_2$-$(CdF_2)_4$ (a) before, (b) during and (c) after UV excitation on top of the ${}^7F_0 \rightarrow {}^5D_1$ excitation of Eu^{3+} 125
6.10 Gaussian fittings of emission profiles of ASL1982; (a) before and (b) during the UV excitation 125
6.11 CEES of ASL1980 $(CaF_2:Eu)_2$-$(CdF_2)_2$ (a) before, (b) during and (c) after UV excitation on top of the ${}^7F_0 \rightarrow {}^5D_1$ excitation of Eu^{3+}. 126
6.12 Gaussian fittings of emission profiles of ASL1980; (a) before and (b) during the UV excitation 126
6.13 Ratios of normalised PL intensities of the O and the I centres in various SLs and ASLs 127
7.1 Schematics of layer composition of a CaF_2:Eu-CdF_2 SL 130
7.2 The calculated energy level splitting of the ${}^7F_1$ multiplet..... 131
7.3 The observed splitting of the I centre of Eu^{3+} 133
7.4 PL intensity ratio of the O and the I centre without additional excitation and under various additional excitations 134
7.5 Schematic of the electron delocalisation upon UV excitation 136
7.6 One dimensional representation of energy barriers for the interstitial electron with respect to the lattice constant a 137
7.7 PL intensity ratios of the O and the I centres in SL 3178 under additional excitation provided by a lamp..... 138
7.7 PL ratios of the O and the I centres in SL 3178 with different power density of the He-Cd laser. 140

List of tables

2.1 Multiplication table for the trigonal C_{3v} symmetry (group) 16

2.2 The irreducible representation of the group C_{3v} 17

2.3 Character table for the group C_{3v} 18

2.4 Character of classes of irreps for C_{3v} and decomposition of D_J of $O_3 \rightarrow C_{3v}$ 19

2.5 Polarisation transition selection rules for Eu^{3+} ion in the C_{3v} symmetry. 22

3.1 Specification of investigated samples. 25

4.1 Strain measured for sample films and SL. 35

4.2 Summary of fitting parameters and coefficients using (4.4) for SL1647 43

4.3 Summary of fitting coefficients and parameters of Eu^{2+} photobleaching in isolated SL 1686 45

4.4 Summary of fitting coefficients and parameters of Eu^{2+} photobleaching in thin film of CaF_2. 47

4.5 Summary of fitting coefficients and parameters of Eu^{3+} PL growth in SL1647. 53

5.1 Polarisation transition selection rules for Eu^{3+} ion in the C_{3v} symmetry. 77

5.2 Summary of thicknesses and binding energies of SLs using (5.5). 96

5.3 Calculated energy levels of Eu^{3+} in cubic symmetry in a CaF_2 crystal and in CaF_2-CdF_2 SLs (cm^{-1} in air) 106

5.4 Crystal field parameters estimated from f-shell programme (cm^{-1}) 107

5.5 Crystal field parameters of the distorted cubic centre (C_{3v}). 109

6.1 Binding energy of electrons in CaF_2 layers. 124

7.1 Calculated energy levels of Eu^{3+} in the I centre in CaF_2:Eu-CdF_2 SLs 133

7.2 Crystal field parameters for the distorted O and the I centres (cm^{-1}) 134

Chapter 1

Introduction

This thesis examines laser spectroscopy of Europium (Eu) defect centres in thin films of CaF_2 and Superlattices (SLs) of CaF_2-CdF_2 epitaxially grown on silicon substrates. Interesting physics can be found in such materials due to the fact that they were grown artificially on different materials with a mono layer (ML) thickness control. It is essential to understand the physical properties of the epitaxial films and SLs so that the development of advanced materials would be beneficial. For example, the laser development would not have happened so rapidly in the 60s and 70s without the fundamental spectroscopic understanding of the lasing media [1].

Laser spectroscopy plays an important role in characterising material properties by means of non-contacting elucidation. Optical spectroscopy is an old experimental technique. In fact one might point out the first illustration of the optical spectroscopy in the book of Genesis [2]. The ‘sun light’ is ‘dispersed’ by rain drops and the rainbow is ‘detected’ by human eyes. In which the three components of optical spectroscopy were met; a light source, a light dispersing element and a light detector. The components have been updated to the current research standard however the experimental technique is still served as a key ingredient in this study.

In epitaxially grown CaF_2 thin films and CaF_2-CdF_2 SLs there are peculiar environments for Eu defect centres due to the fact that the hosts are artificially grown on silicon substrates as a template and, more importantly, the existence of an interesting physical environment at the CaF_2-CdF_2 interface. None of the above can be achieved by conventional crystal growth techniques. Molecular Beam Epitaxy (MBE), on the other

hand, can produce thin films and SLs with an atomic layer precision and control. Eu can be deposited in various regions of thin films and SLs using the advantages of the MBE growth technique. For this study, Eu is deposited, along with CaF_2, on a silicon (Si) substrate. This separates not only Eu being selectively doped in CaF_2 layers but also separates Eu further from being deposited closer to or remote from the CaF_2-CdF_2 interface. Usually the thickness of a mono layer (ML) determines whether the Eu centre is an interface or a remote defect for very thin SLs. Even though Eu ions are separated by ML in thin layers, one can be fully exposed to a completely different crystal environment than the other.

When Eu ions embedded in crystal lattices are subjected to the electromagnetic radiation, provided by a laser excitation, they undergo optical transitions. However these transitions can be characterised by the electric field produced by the local crystal environment of the host. Due to the non-uniform environment the position of the excited states of Eu in the interface and in the middle of the host are expected to be different. Studying optical transitions of Eu centres will assist in a fuller understanding of the interaction with the crystal host especially at the interface. Following Bhargava *et al*., nano-scaled materials doped with optically active luminescence centres will open new investigation opportunities in the structural properties of such materials [3].

1.1 Thin films of CaF_2 and superlattices of CaF_2-CdF_2 host

CaF_2 is an alkaline earth fluoride with a 12 eV [4-6] band gap which exhibits optical transparency over a wide range of wavelengths [6]. Due to its wide band gap CaF_2 is a prime candidate for many optical components such as UV laser materials, lenses and prisms [7]. CaF_2 also demonstrated a good growth on semiconductor surfaces [8] which makes the growth of heterostructures readily possible. In particular, a recent epitaxial growth of CaF_2 on Si substrate with a lattice mismatch of 0.6 % at room temperature [9, 10] made CaF_2 a material which will be useful in the development of compact three-dimensional devices [11].

Similarly, CdF_2 has a fluorite structure with a wide band gap which was measured to be from 6 to 8 eV with time [12-14]. Despite CdF_2 being an insulator, simple treatments result in a vast change to its electrical property. For example, CdF_2 exhibits an n-type semiconductor behaviour with increased conductivity of 10^7 times when doped with trivalent impurities followed by thermal annealing [15, 16]. CdF_2 also allows an epitaxial growth on Si surface due to its good lattice mismatch to Si of 0.8 % at room temperature [17].

It was demonstrated for the first time by the collaborators of the project that CdF_2 can be grown on CaF_2/Si heterostructures [17-19]. Since CaF_2 and CdF_2 are the same fluorite-type crystals, which consist of eight fluorine anions at each corner of a cube and the cations (Ca^{2+} or Cd^{2+}) in centre of alternating cubes, they grow coherently with the CaF_2 buffer layers on top of [111] oriented Si substrate.

More importantly, interesting physical phenomena have been reported by the same group. In particular, photoluminescence (PL) bleaching of the defect centre due to a possible transfer of electrons in CaF_2:Eu-CdF_2 SLs was observed [20, 21] suggesting that the interface of CaF_2-CdF_2 is responsible for such transfer. Moreover, x-ray photoelectron spectroscopy revealed that a conduction band offset of 2.9 eV exists between CaF_2 and CdF_2 [19] as shown in fig. 1.1. This effect, given that there is conduction band offset, is attractive in designing fluoride-based optical memory [22] and in resonant tunnelling diodes (RTDs).

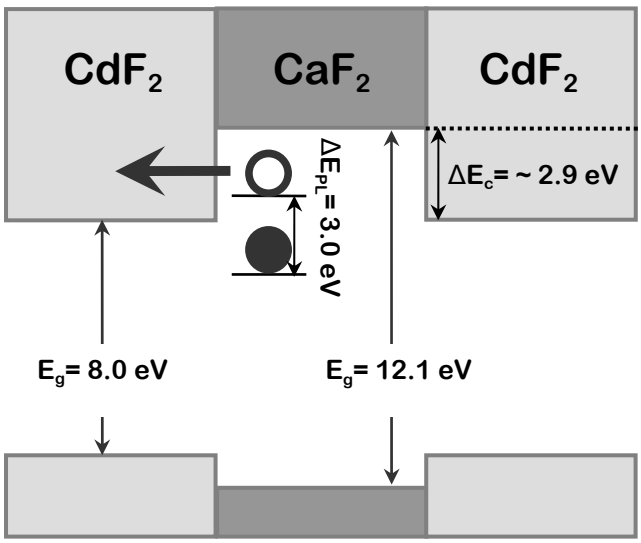

Fig. 1.1. Schematic of band gaps of CaF_2 and CdF_2. The values are 12.1 eV and 8.0 eV, respectively. The band gap offset between CaF_2 and CdF_2 is ~2.9 eV given by x-ray photoelectron spectroscopy. The excited state of Eu^{2+} is resonant with the conduction band of CdF_2. Note that the schematic is not drawn to scale.

1.2 The Lanthanoids

Eu belongs to the Lanthanoids* (or Lanthanides) which comes from the Greek word *lanthanos*, meaning hidden [23]. However the lanthanoids are said to be unhidden as they are used in many optical and photonic applications such as lasing media, phosphors, fluorescence lamps and x-ray imaging. Also some lanthanoids (Eu) are said to be used in anti-counterfeiting agents in Euro bank notes [24]. However it was commented that further investigations of the agents would be a violation of the law. Apart from some limitations the lanthanoids can be used and studied lawfully.

The lanthanoids are characterised by the filling of 4*f* shell electrons. For instance, a neutral Eu has 6 electrons in the partially filled 4*f* shell. It also naturally occurs as ionic forms by removal of weakly bound outer $6s^2$ or $5d6s^2$ electrons [25]. The filling of 4*f* electrons takes place inside the $5s^2 5p^6$ shell. Following the definition of 'inner' electrons [26], the lanthanoids commence with Cerium (Z = 58) and end with Lutetium (Z = 71).

Since the 4*f* electrons are screened by closed outer shells they behave similarly to the electrons in free ions. Hence optical transitions involved with the *f* shell of the lanthanoids consist of narrow lines. The electronic configurations of the lanthanoids are given by an assumption that the potential energy is spherically symmetric. When the lanthanoids are embedded in crystals, however, the potential is no longer spherical and the symmetry becomes lower due to the electric field produced by the crystal environment. The influence of the crystal field is considered as a perturbation to the free ion, yet effectively predicts the energy levels of the lanthanoids.

In general when trivalent Eu ions substitute for Ca^{2+} during crystal growth some extra fluorine (F^-) ions occupy interstitially to the neighbouring cubic lattice to retain the overall neutrality. Fig. 1.2 shows examples of such charge compensation by fluorine ions. Different charge compensation states can take place depends upon the orientation of the interstitial F^- ions with respect to Eu^{3+}. For example, trigonal C_{3v}, tetragonal C_{4v}, and

*IUPAC recently recommended the name lanthanoids rather than lanthanides. The suffix –ide is often used for the anions which may confuse readers.

cubic O_h symmetry can be obtained with F^- ions localised in [111], [100] directions and in remote lattice positions from Eu^{3+}.

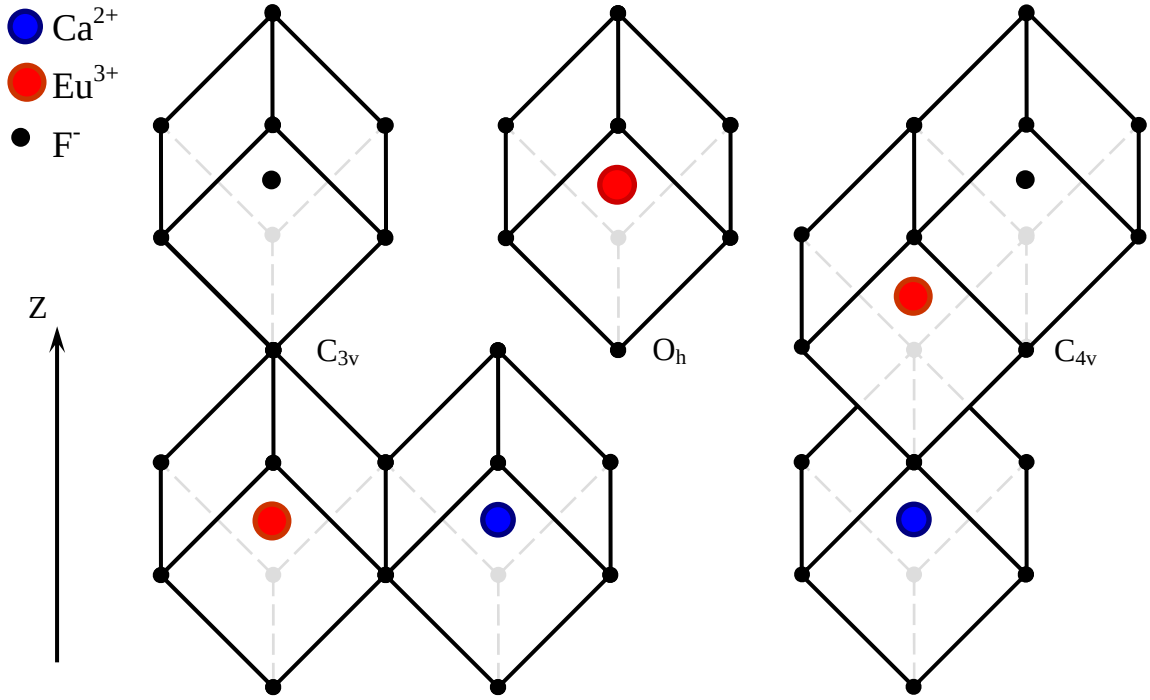

Fig. 1.2. Schematic of charge compensation by F ions. The Z axis indicates the [111] direction.

It is interesting to investigate the symmetry of the Eu^{3+} ions doped in the nano-scale MBE hosts. Due to the high pressure and temperature of the MBE growth technique, imperfections of the crystal structures, dislocations and as well as uncontrolled charge carriers are expected in SLs and in thin films. For such reasons the F^- ions are not the only charge compensations. Electrons may occupy interstitially as a charge compensator instead of the F^- ions. In addition some degree of the crystal distortion due to the imperfect growth should be taken into account for the symmetry of Eu^{3+}. As a result, an admixture of all the possibilities associated with the nano crystals, unique symmetries of Eu^{3+} centres can be observed in optical transitions. The energy levels of the individual Eu^{3+} centres can be obtained by advanced laser spectroscopic techniques. The analysis of the energy levels will ensure fuller interpretation of the crystal structures of the SLs and thin films.

Previously we have successfully reported a novel centre of Eu^{3+} [27] along with the cubic centre in SLs. The I centre is thought of as the electron charge compensated centre at the interface of the CaF_2:Eu-CdF_2 SLs. Hence the name 'Interface (I)' centre. The I centre exhibited strong thickness and temperature dependent PL intensity when excited by a tunable dye laser. It is crucial to determine optical behaviour of the Eu^{3+} centres in SLs so that the corresponding physical properties of the SLs are understood. In this investigation Eu^{3+} ions continue to serve as optical probes for the epitaxially grown SLs and thin films.

1.3 Outline

This thesis consists of the following chapters on various aspects of Eu centres in CaF_2:Eu-CdF_2 SL and CaF_2:Eu thin films.

- In chapter 2 the theoretical background determining energy levels of rare earths is discussed. Free ion Hamiltonian for the lanthanoids and the applied crystal field as a perturbation to the Hamiltonian is briefly discussed.
- In chapter 3 the combined excitation-emission spectroscopy (CEES) is introduced as the spectroscopic technique used in this study. Some other essential experimental techniques and instruments are also discussed.
- In chapter 4 spectroscopy of Eu^{2+} is surveyed in realising strain associated with thin films and SLs. PL bleaching from Eu^{2+} is also reported and subsequent growth of Eu^{3+} is suggested and tested.
- In chapters 5 and 6, PL behaviours of the I and the O centres are mainly discussed. Some physical models are proposed and tested. Additional excitations were provided to delocalise the charge compensating electron for the I centre.
- The effective role of the charge compensating electron for the formation of the I centre is discussed in chapter 7. To assist that discussion a crystal structure which incorporates the extra electron along a [111] direction is considered. Crystal field calculations are performed using the above model. Also the physical delocalisation of the electron is explained by tunnelling back and forth through the appropriate potential barriers.

- Finally the investigation is summarised in chapter 8 with further suggested research.

References

[1] A. A. Kaminskii, *Laser Crystals Their Physics and Properties*, Second ed: Springer-Verlag, 1990.

[2] *The holy Bible Genesis Chap 9*.

[3] R. N. Bhargava, D. Gallapher, X. Hong, A. Nurmikko, "Optical Properties of Manganese-Doped Nanocrystals of ZnS " *Phys. Rev. Lett.*, vol. 72, pp. 416-419, 1994.

[4] G. W. Rubloff, "Far-Ultraviolet Reflectance Spectra and the Electronic structure of Ionic Crystals " *Phys. Rev. B*, vol. 5, pp. 662-684, 1972.

[5] R. Lindner, M. Reichling, R. T. Williams, E. Matthias, "Femtosecond laser pulse excitation of electrons and excitons in CaF_2 and SrF_2," *J. Phys.: Condens. Matter*, vol. 13, pp. 2339-2346, 2001.

[6] N. S. Sokolov, S. M. Suturin, "MBE-growth peculiarities of fluoride (CaF_2-CdF_2) thin film structures," *Thin Solid Films*, vol. 367, pp. 112-119, 2000.

[7] T. Pilvi, K. Arstila, M. Leskela, M. Ritala, "Novel ALD Process for Depositing CaF_2 Thin Films," *Chem. Mater.*, vol. 19, pp. 3387-3392, 2007.

[8] V. Chakarian, T. D. Durbin, P. R. Varekamp, J. A. Yarmoff, "Formation of surface F centres on CaF_2/Si(111)," *Phys. Rev. B*, vol. 48, pp. 18332-18335, 1993.

[9] D. Rieger, F. J. Himpsel, U. O. Karlsson, F. R. McFeely, J. F. Morar, J. A. Yarmoff, "Electronic structure of the CaF_2/Si(111) Interface," *Phys. Rev. B*, vol. 34, pp. 7295-7306, 1986.

[10] S. Blunier, H. Zogg, C. Maissen, A. N. Tiwari, R. M. Overney, H. Haefke, P. A. Buffat, G. Kostroz "Lattice and Thermal Misfit and Disclocations in CaF_2/Si(111) and BaF_2-CaF_2/Si(111) Structures," *Phys. Rev. Lett.*, vol. 68, pp. 3599-3602, 1992.

[11] R. M. Tromp, M. C. Reuter, "Structure of the Si(111)-CdF_2 Interface," *Phys. Rev. Lett.*, vol. 61, pp. 1756-1759, 1988.

[12] J. S. Prener, J. D. Kingsley, "Preparation and Optical Transmission of Cadmium Fluoride Crystals," *J. Chem. Phys.*, vol. 35, pp. 2256-2257, 1961.

[13] J. P. Jouart, C. Bissieux, M. Egee, G. Mary, M. de Murcia, "Optical study of Eu^{3+} centres in CdF_2," *J. Phys. C: Solid State Phys.*, vol. 14, pp. 4923-4935, 1981.

[14] B. A. Orlowski, J. M. Langer, "Determination of the CdF_2 valence band structure by Photoemission Measurement," *Phys. Status. Solidi* vol. 91, pp. K53, 1979.

[15] J. D. Kingsley, J. S. Prener, "Free Charge Carrier Effect in Cadmium fluoride," *Phys. Rev. Lett.*, vol. 8, pp. 315-316, 1962.

[16] J. S. Prener, J. D. Kingsley, "Mechanism of the Conversion of CdF_2 from an Insulator to a Semiconductor," *J. Chem. Phys.*, vol. 38, pp. 667-671, 1963.

[17] N. S. Sokolov, S. V. Gastev, S. V. Novikov, N. L. Yakovlev, A. Izumi, S. Furukawa, "Molecular beam epitaxy of CdF_2 layers on CaF_2(111) and Si(111)," *Appl. Phys. Lett.*, vol. 64, pp. 2964-2966, 1994.

[18] A. Izumi, K. Tsutsui, N. S. Sokolov, N. N. Faleev, S. V. Gastev, S. V. Novikov, N. L. Yakovlev, "High-quality CdF_2 layer grwoth on CaF_2/Si(111) " *J. Crystal Growth*, vol. 150, 1995.

[19] A. Izumi, Y. Hirai, K. Tsutsui, N. S. Sokolov, "Study of band offsets in CdF_2/CaF_2/Si(111) heterostructures using x-ray photoelectric spectroscopy," *Appl. Phys. Lett.*, vol. 67, pp. 2792-2794, 1995.

[20] N. S. Sokolov, S. V. Gastev, A. Y. Khilko, S. M. Suturin, I. N. Yassievich, J. M. Langer, A. Kozanecki, "Tunneling-assisted autoionization of the localized impurities in nanostructures," *Phys. Rev. B*, vol. 59, pp. R2525-R2528, 1999.

[21] S. M. Suturin, S. A. Basun, S. V. Gastev, J. M. Langer, R. S. Meltzer, N. S. Sokolov, "Optical detection of electron transfer through interfaces in CaF_2:Eu-CdF_2 SLs," *Appl. Surf. Sci.*, vol. 162-163, pp. 474-478, 2000.

[22] N. S. Sokolov, S. M. Suturin, "MBE growth of calcium and cadmium fluoride nanostructures on silicon " *Appl. Surf. Sci.*, vol. 175-176, pp. 619-628, 2001.

[23] P. C. Becker, N. A. Olsson, J. R. Simpson, *Erbium-Doped Fiber Amplifiers*: Academic Press, 1999.

[24] F. Suyver, A. Meijerink, "Europium beveiligt de Euro," *Chemisch2Weekblad*, vol. 98, pp. 12-13, 2002.

[25] B. G. Wybourne, *Spectroscopic Properties of Rare Earths*: John Wiley & Sons, Inc., 1965.

[26] G. Burns, *Solid State Physics*: Academic Press, 1990.

[27] J. K. Choi, "Laser spectroscopy of Eu^{3+} ions in CaF_2/CdF_2 Super-lattices," in *M. Sc. Thesis*. Christchurch: University of Canterbury, 2004.

Chapter 2

Theory

2.1 Introduction

The Hamiltonian for a free ion has spherical symmetry so is invariant with respect to operations such as rotations, reflections and inversions. When lanthanoids are embedded in crystals the environment breaks the spherical symmetry. The non-uniform distribution of ligand charges about the lanthanoids lifts the degeneracy of multiplet and yields further splitting of the energy levels. This effect known as 'crystal field' on the 4*f* electronic configuration is described by the theoretical approach and is discussed in this chapter. The crystal field is treated as a perturbation to the free ion Hamiltonian.

2.2 The free-ion Hamiltonian

The configuration of 4*f* states of the lanthanoids are described by a set of one-electron orbitals. The Hamiltonian operator describing the 4*f* electrons in a free ion can be written as,

$$H_{\mathrm{fi}} = -\left(\frac{h}{2\pi}\right)^2 \frac{1}{2m}\sum_{i=1}^{N}\nabla_i^2 - \sum_{i=1}^{N}\frac{Z^* e^2}{r_i} + \sum_{i<j}^{N}\frac{e^2}{r_{ij}} + \sum_{i=1}^{N}\zeta(r_i)\vec{s}_i\cdot\vec{l}_i + \text{ smaller terms,} \tag{2.1}$$

where N is the number of 4f electrons. $Z^{*}e$ is the effective charge at the nucleus. Here $\zeta(r_i)$ is the spin-orbit coupling function. The terms that lift the degeneracy of the 4f configurations are the third and the fourth of equation (2.1). These terms can be identified as the mutual Coulomb repulsion and spin-orbit interaction of the 4f electrons.

The Russell-Saunders (or *LS* coupling) scheme is generally used to describe the electronic configurations of the rare earth ions. This scheme first couples the orbital angular momenta of the electrons as the total orbital angular momentum L, and the spin angular momenta as the total spin angular momentum S. The coupled L and S yields the total angular momentum J.

From the beginning, the Coulomb repulsion interaction as defined in H_{fi} is independent of J, and the matrix elements are diagonal with S and L, which splits the configuration of the 4f state into terms of ^{2S+1}X where X is labelled by different L values. Hence this is commonly expressed as ^{2S+1}L. For the spin-orbit interaction on the other hand, it is diagonal with J but not with S or L. The spin-orbit interaction lifts the degeneracy with different J values and splits the *LS* term. The notation for the *LSJ* is denoted as $^{2S+1}L_J$. However there is still degeneracy left due to the spherical symmetry of H_{fi}. The crystal field removes some of this degeneracy due to the non-uniform distribution of the charges around the free ion and is discussed in the next section.

2.3 Crystal Field Hamiltonian

When ions are embedded in a crystal lattice, the spherical symmetry in which the lanthanoids enjoy in vapour phase is lowered due to the non-spherical surroundings [1]. These resulting non-spherical electrostatic interactions, called the crystal fields, remove the degeneracy of J multiplets up to $(2J+1)$ states called the Stark levels. The symmetry about an optically active lanthanoid centre plays an important role in the degree of removal of the degeneracy. When Eu^{3+} is doped in higher local point charge symmetry such as a cubic centre, a $J = 1$ multiplet of the Eu^{3+} remains unsplit. However, taking into account a charge compensation along a [111] direction, the lower symmetry about the

Eu^{3+}-F^- centre removes the degeneracy of the parent multiplet into two split energy levels. Maximum splitting up to three ($2J$ +1 = 3) energy level configurations can be observed depending upon the symmetry about the Eu^{3+}. For the 4*f* electrons, the crystal field Hamiltonian is a small perturbation compared to the Coulomb and spin-orbit interactions and their magnitude is smaller by roughly 100 times [1]. The schematic diagram of the *4f* electronic configurations combined with free-ion and crystal field Hamiltonian is shown in fig. 2.1.

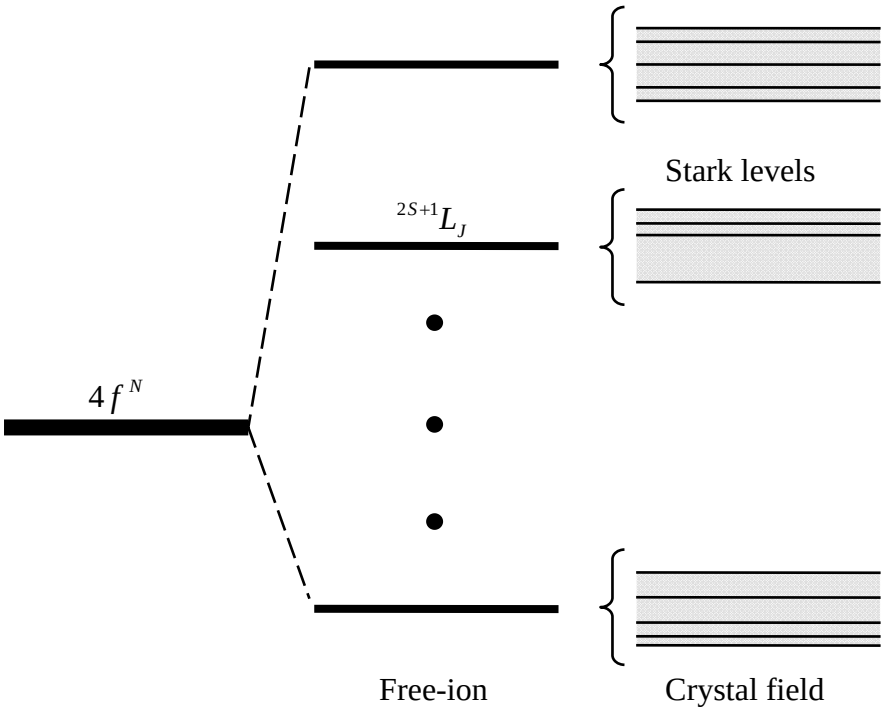

Fig. 2.1. Schematic of the splitting for the 4*f* electronic configuration.

Since the effect of the crystal field is to add a low symmetry potential [2] to the spherical potentials of the free ion, the crystal field Hamiltonian may be expanded in terms of spherical harmonics analogous to the free ion Hamiltonian. Thus the representative crystal field Hamiltonian, H_{CF} can be written as a product of a radial function and an angular function as,

$$H_{CF} = \sum_{k,q} B_q^k \sum_{i=1}^{N} C_q^{(k)}(i), \qquad (2.2)$$

where the summation is over the electrons in the $4f^N$ configuration. Here k is the rank for the operator and q is the component of the rank. The radial functions B_q^k are treated as parameters that can be found empirically from experimental data. The angular function, which is a tensor operator, $C_q^{(k)}$ is proportional to the spherical harmonics, Y_{kq}, as

$$C_q^{(k)} = \sqrt{\frac{4\pi}{2k+1}} Y_{kq}. \tag{2.3}$$

The first term of the expansion in (2.2) can obviously be obtained by letting $k = q = 0$. However this term is responsible for a uniform shift of all the energy levels as a whole and hence generally ignored. To require the Hamiltonian to be invariant, the values of k and q are limited by the point symmetry about the lanthanoid centres in crystal lattices [3]. The evaluation of the matrix elements (omitting the B_q^k parameters) of the crystal field for $4f^N$ configuration can be made with simplicity following factorisation known as the Wigner-Eckart theorem,

$$\left\langle f^N \alpha LSJM_J \left| C_q^{(k)} \right| f^N \alpha' L'SJ'M'_J \right\rangle = (-1)^{J-M_J} \begin{pmatrix} J & k & J' \\ -M_J & q & M'_J \end{pmatrix} \times \left(f^N \alpha LSJ \left\| C^{(k)} \right\| f^N \alpha' L'SJ' \right), \tag{2.4}$$

where

$$\left(\alpha LSJ \left\| C^{(k)} \right\| \alpha' L'SJ' \right) = (-1)^{S+k+J+L'} \sqrt{(2J+1)(2J'+1)} \times \begin{Bmatrix} L & J & S \\ J' & L' & k \end{Bmatrix} \left(\alpha LS \left\| C^{(k)} \right\| \alpha' L'S \right). \tag{2.5}$$

The 3j symbols $\begin{pmatrix} J & k & J' \\ -M_J & q & M'_J \end{pmatrix}$ embody the selection rules that determine the non-zero tensor operators. The 3j symbols are non zero when triangular relationship between J, J' and k is met as, $J = |k - J'|, |k - J'+1|, ..., k + J'$. As a result, the possible rank k values

for the operator for the 4*f* electrons are 2, 4 and 6. A further selection rule for the 3j symbols is when $-M_J + q + M'_J = 0$, otherwise the 3j symbols vanish. Both the 3j and the 6j $\begin{Bmatrix} L & J & S \\ J' & L' & k \end{Bmatrix}$, symbols can be computed [4, 5]. The doubly reduced matrix elements $\left(\alpha LS \left\| C^{(k)} \right\| \alpha' L' S\right)$, which are independent of *J*, are tabulated in Nielson and Koster [6].

The splitting of the 4*f* configuration due to the effect of the crystal field is characterised by the point group symmetries about the lanthanoids centre. The symmetry of the crystal field Hamiltonian is defined as 'the point group of symmetry operators which leave the Hamiltonian invariant' [4]. Now (2.2) is readily expanded considering three crystal symmetries for Eu^{3+} ions in CaF_2 crystal lattices namely, a cubic (O_h)*, a tetragonal (C_{4v}) and a trigonal (C_{3v}). The representative Hamiltonians for different symmetries are given as,

$$H_{O_h} = B_C^4\left[C_0^{(4)} + \sqrt{\frac{5}{14}}\left(C_4^{(4)} + C_{-4}^{(4)}\right)\right] + B_C^6\left[C_0^6 - \sqrt{\frac{7}{2}}\left(C_4^{(6)} + C_{-4}^{(6)}\right)\right]. \tag{2.6}$$

$$\begin{aligned} H_{C_{4v}} = {} & B_A^2 C_0^{(2)} + B_A^4\left[C_0^{(4)} - \sqrt{\frac{7}{10}}\left(C_4^{(4)} + C_{-4}^{(4)}\right)\right] + B_A^6\left[C_0^{(6)} + \sqrt{\frac{1}{14}}\left(C_4^{(6)} + C_{-4}^{(6)}\right)\right] \\ & + B_C^4\left[C_0^{(4)} + \sqrt{\frac{5}{14}}\left(C_4^{(4)} + C_{-4}^{(4)}\right)\right] + B_C^6\left[C_0^{(6)} - \sqrt{\frac{7}{2}}\left(C_4^{(6)} + C_{-4}^{(6)}\right)\right]. \end{aligned} \tag{2.7}$$

$$\begin{aligned} H_{C_{3v}} = {} & B_A^2 C_0^{(2)} + B_A^4\left[C_0^{(4)} - \frac{1}{2}\sqrt{\frac{7}{10}}\left(C_3^{(4)} - C_{-3}^{(4)}\right)\right] + B_A^6\left[\sqrt{\frac{11}{42}}\left(C_3^{(6)} - C_{-3}^{(6)}\right) + \sqrt{\frac{5}{12}}\left(C_6^{(6)} + C_{-6}^{(6)}\right)\right] \\ & + B_A^{6'}\left[C_0^{(6)} + \frac{4}{7}\sqrt{\frac{10}{21}}\left(C_3^{(6)} - C_{-3}^{(6)}\right) - \frac{4}{7}\sqrt{\frac{11}{21}}\left(C_6^{(6)} + C_{-6}^{(6)}\right)\right] + B_C^4\left[C_0^{(4)} + \sqrt{\frac{10}{7}}\left(C_3^{(4)} - C_{-3}^{(4)}\right)\right] \\ & + B_c^6\left[C_0^{(6)} - \sqrt{\frac{35}{96}}\left(C_3^{(6)} - C_{-3}^{(6)}\right) + \frac{1}{8}\sqrt{\frac{77}{3}}\left(C_6^{(6)} + C_{-6}^{(6)}\right)\right]. \end{aligned} \tag{2.8}$$

* In later chapters the cubic centre is referred as 'O' for convenience.

2.3.1 Irreducible representations and multiplet identifications

It was shown in the previous section how the crystal field symmetries are used to determine appropriate operators for the crystal field Hamiltonian. In this section identifications of the split energy levels for lanthanoids embedded in crystal lattice are discussed assisted by the theory of groups.

Let us consider a trigonal C_{3v} symmetry group which consists of symmetry operators E, C_3, C_3^2, $\sigma_\upsilon(1)$, $\sigma_\upsilon(2)$ and $\sigma_\upsilon(3)$. Here E is the identity operator which provides either 0º or 360º rotations about any axis. The C_3 and the C_3^2 operators represent $\frac{360^o}{3}$ and $\frac{2\times 360^o}{3}$ anticlockwise rotations about the principal axis, respectively. Finally $\sigma_\upsilon(n)$ are reflection operations which are equivalent to a π rotation about any symmetry axis O-*n*'s (fig. 2.2). The symmetry of the C_{3v} is schematically shown in fig. 2.2.

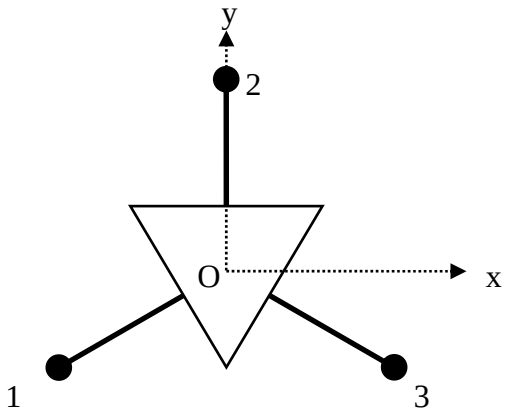

Fig. 2.2. The symmetry of a C_{3v} centre with the principal axis (*z*) pointing out of the page through the centre of the inner triangle.

By definition, the C_{3v} forms a group if the above elements (operators) of the group are satisfied properties postulated by the group theory [7]. There are five properties[*], associated with the definition of a group. An example is the existence of an inverse element which satisfies $C_3 C_3^{-1} = C_3^{-1} C_3 = E$ [7]. Also using the property that a

[*] There are only four properties discussed in Wybourne [4]. However this is not a major concern delivering the group theory into the energy level identification of the lanthanoids.

combination, $\sigma_\upsilon(1)C_3 = \sigma_\upsilon(2)$, must form an element of the C_{3v} group, one can construct a 6×6 multiplication table in terms of the given elements as shown in table 2.1. One can also confirm the table, for example, by applying $\sigma_\upsilon(1)$ first to fig. 2.2 followed by C_3 which then results in $\sigma_\upsilon(2)$.

Table 2.1. Multiplication table for the trigonal C_{3v} symmetry (group).

	E	C_3	C_3^2	$\sigma_\upsilon(1)$	$\sigma_\upsilon(2)$	$\sigma_\upsilon(3)$
E	E	C_3	C_3^2	$\sigma_\upsilon(1)$	$\sigma_\upsilon(2)$	$\sigma_\upsilon(3)$
C_3	C_3	C_3^2	E	$\sigma_\upsilon(2)$	$\sigma_\upsilon(3)$	$\sigma_\upsilon(1)$
C_3^2	C_3^2	E	C_3	$\sigma_\upsilon(3)$	$\sigma_\upsilon(1)$	$\sigma_\upsilon(2)$
$\sigma_\upsilon(1)$	$\sigma_\upsilon(1)$	$\sigma_\upsilon(2)$	$\sigma_\upsilon(3)$	E	C_3	C_3^2
$\sigma_\upsilon(2)$	$\sigma_\upsilon(2)$	$\sigma_\upsilon(3)$	$\sigma_\upsilon(1)$	C_3^2	E	C_3
$\sigma_\upsilon(3)$	$\sigma_\upsilon(3)$	$\sigma_\upsilon(1)$	$\sigma_\upsilon(2)$	C_3	C_3^2	E

Although the Hamiltonian remains invariant under the symmetry operations, physical functions, say a position function of a particular ion (fig. 2.2) is transformed upon each operation. For example, when a symmetry operator C_3 was applied to a function describing the position of an ion (n = 2), the transformed function should take the form

$$C_3\begin{bmatrix}x\\y\end{bmatrix}=\begin{bmatrix}-\frac{1}{2} & -\frac{\sqrt{3}}{2}\\ \frac{\sqrt{3}}{2} & -\frac{1}{2}\end{bmatrix}\begin{bmatrix}x\\y\end{bmatrix}.$$

This is equivalent to rotating the *x*-*y* axes clockwise by 120º. For any functions that are associated with the *x*-*y* axis (rotations and reflections regardless of the z axis), the transformed functions by the six operators should all have 2×2 matrices constructed in their functions. The generated matrix for all operators have the same multiplication

property as shown in table 2.1. For example, a matrix generated by $\sigma_\upsilon(2)$ is equivalent to a multiplication of matrices generated by $\sigma_\upsilon(1)$ and C_3,

$$\begin{bmatrix} \frac{1}{2} & \frac{\sqrt{3}}{2} \\ \frac{\sqrt{3}}{2} & -\frac{1}{2} \end{bmatrix} \begin{bmatrix} -\frac{1}{2} & \frac{\sqrt{3}}{2} \\ -\frac{\sqrt{3}}{2} & -\frac{1}{2} \end{bmatrix} = \begin{bmatrix} -1 & 0 \\ 0 & 1 \end{bmatrix}.$$

If all the matrices multiply this way they are said to form representations of the C_{3v} operations [7]. Similarly for operators associated with the functions in the z axis, the generated representations should take a form of 1×1(one dimension) matrices,

$$C_3(z) = 1z,\ C_3^2(z) = 1z,\ \sigma_\upsilon(n)(z) = (-1)z, n = 1,2,3.$$

The representations generated by the identity operator are considered as 1. Following Heine [7], a symbol E_g is used for the representations that transform the functions in the *x-y* axis. Similarly A_{2g} is used for a set of elements that transform the function in the z-axis. Finally A_{1g} is used for identity element. Now table 2.1 can be rewritten with so-called 'irreducible representations' of the group C_{3v} as shown in table 2.2.

Table 2.2. The irreducible representation of the group C_{3v}.

	E	C_3	C_3^2	$\sigma_\upsilon(1)$	$\sigma_\upsilon(2)$	$\sigma_\upsilon(3)$
A_{1g}	1	1	1	1	1	1
E_g	$\begin{pmatrix} 1 & 0 \\ 0 & 1 \end{pmatrix}$	$\begin{pmatrix} -\frac{1}{2} & \frac{\sqrt{3}}{2} \\ -\frac{\sqrt{3}}{2} & -\frac{1}{2} \end{pmatrix}$	$\begin{pmatrix} -\frac{1}{2} & -\frac{\sqrt{3}}{2} \\ \frac{\sqrt{3}}{2} & -\frac{1}{2} \end{pmatrix}$	$\begin{pmatrix} \frac{1}{2} & \frac{\sqrt{3}}{2} \\ \frac{\sqrt{3}}{2} & -\frac{1}{2} \end{pmatrix}$	$\begin{pmatrix} -1 & 0 \\ 0 & 1 \end{pmatrix}$	$\begin{pmatrix} \frac{1}{2} & -\frac{\sqrt{3}}{2} \\ -\frac{\sqrt{3}}{2} & -\frac{1}{2} \end{pmatrix}$
A_{2g}	1	1	1	-1	-1	-1

The group theory further defines the 'character (traces)' $\chi_s(P)$ of the matrix $\Gamma_s(P)$ such that [3],

$$\chi_s(P) = \sum_i \Gamma_s(P)_{ii}. \tag{2.9}$$

The summation is over the diagonal entries of the matrix in table 2.2. For the E_g irrep, the character of the matrix for C_3 is equivalent to -1 which is the same for the C_3^2 operator. The characters for the $\sigma_\upsilon(n)$ operators are all zero. Since the trace is the same for each operator in a class, the elements of the C_{3v} group can be categorised into three classes only, identity, rotations and reflections. One can see that the characters for all the matrices are the same for C_3 and C_3^2 in table 2.2. Using this fact the characterisation of the irreps for C_{3v} symmetry group can be constructed as shown in table 2.3. Since there is no difference in characters of operators within a class, separate labelling of the elements is not required.

Table 2.3. Character table for the group C_{3v}.

	E	C_3	σ_υ
A_{1g}	1	1	1
E_g	2	-1	0
A_{2g}	1	1	-1

Finally the character table for the particular symmetry group can be used to determine the number of split levels, degeneracies and energy level identifications for given J values. Let us consider a full rotation group O_3 which contains all symmetry operations. The dimension for the representation of the O_3 group entirely depends on the value of J ($2J$ +1). The ($2J$ +1) dimensional representation of the O_3 can be decomposed into irreps of C_{3v} symmetry as the C_{3v} forms a subgroup of O_3.

The character of each class provides a useful relationship between the full rotation group and its subgroup when an identical symmetry operation is applied. Accounting for the (2*J* + 1) dimension (or degeneracy) of the O_3 group the character of the classes of the C_{3v} symmetry is written as,

$$\chi(\phi) = \frac{\sin(2J+1)\phi/2}{\sin\phi/2}, \tag{2.10}$$

where ϕ is determined by physical rotations of the classes of the C_{3v}. The angle of rotation ϕ is 0, $\pm\frac{2\pi}{3}$ and π, respectively for E, C_3 and σ_υ. Now the character of the classes of the C_{3v} with respect to *J* can be determined as shown in table. 2.4. In other words the representation D_J of the full rotation group O_3 can be decomposed to the irreps of the C_{3v} symmetry.

Table 2.4. Character of classes of irreps for C_{3v} and decomposition of D_J of $O_3 \rightarrow C_{3v}$.

D_J	E	C_3	σ_υ	$O_3 \rightarrow C_{3v}$	Number of levels
0	1	1	1	A_{1g}	1
1	3	0	-1	A_{2g}+ E_g	2
2	5	-1	1	A_{1g} + 2E_g	3
3	7	1	-1	A_{1g} + 2A_{2g} + 2E_g	5
4	9	0	1	2A_{1g} + A_{2g} + 3E_g	7
5	11	-1	-1	A_{1g} + 2A_{2g} + 4E_g	9

It can be shown that all the characters of the classes determined by different *J* values are expressed in terms of the irreps for each class as shown in table 2.4. For example, the $^7F_1$ multiplet, one of the low lying energy levels of Eu^{3+} in the trigonal C_{3v}, can be split into two levels which are assigned as A_{2g} and E_g as shown in fig. 2.3. These symbols are used through out this thesis for multiplet identifications. Similarly all the energy level

splittings and identifications of Eu^{3+} in different symmetry centres can be determined in this way.

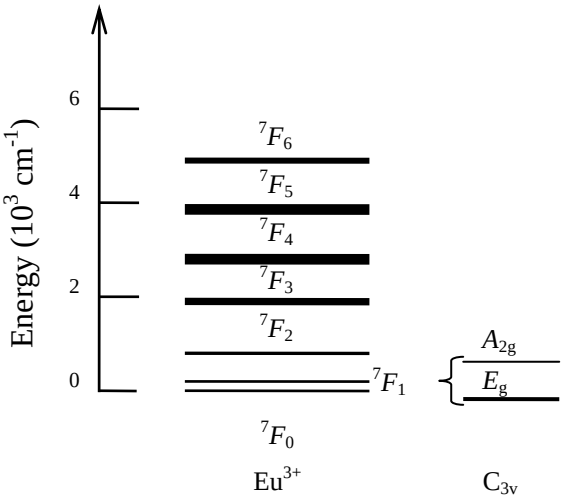

Fig. 2.3. Energy level splitting and its assignment for Eu^{3+} in C_{3v} symmetry centre.

2.4 Transition and polarisation selection rules

For free ions, the nature of optical transitions of the lanthanoids is through magnetic dipole as change of the parity is not required within the *f* shell transitions occur. In crystals the majority of the transitions occurs by an electric dipole process because the crystal field mixes in states of opposite parity such as the *d* shells [8]. Thus some admixture of the opposite parity must become involved with the configurations of the lanthanoid. Many lanthanoids centres embedded in crystals have lack of inversion [5] which allows the component of the opposite parity to the 4*f* wavefunctions [1] as, $\Psi = a\Psi\left(4f^n\right) + b\Psi\left(4f^{n-1}5d\right)$ [5]. Here $a \sim 1$ and $b << 1$. Even for the symmetry centres which contain inversion, the optical transitions often occur through the electric dipole process. It is possibly due to the tendency that the lanthanoid distort its surroundings upon embedding and removes the inversion symmetry [8]. Hence selection rules are valid for both electric and magnetic dipole transitions of the lanthanoids. The selection rules are associated with the quantum numbers *LSJ*. A transition probability (so-called transition strength, P_s) for pure magnetic dipole transitions between two states, Ψ_1 and Ψ_2

(assuming *b* is zero) is proportional to the matrix elements such as [8], $P_s \propto \langle \Psi_1 | md | \Psi_2 \rangle$, where *md* is the magnetic dipole operator. The matrix elements will be zero when the total spin difference between the states is zero, hence we expect $\Delta S = 0$ and $\Delta L = 0$. However due to the spin-orbit coupling a configuration mixing of different *S* and *L* states is allowed. As a result, in general, $\Delta S = \pm 1$ and $\Delta L = \pm 1$ transitions are valid. For example, the major transitions of Eu^{3+} centres studied in this thesis were the $^7F_0 \rightarrow {}^5D_1$ excitation and the $^5D_0 \rightarrow {}^7F_1$ emission which all satisfy the above selection rules. Similarly some selection rules for the *J* quantum number are also available. Again the pure magnetic dipole transitions are restricted to

$$\Delta J = 0, \pm 1, \text{ excluding } 0 \leftrightarrow 0.$$

The selection rules for electric dipole transitions in the lanthanoids are, $\Delta L \leq 6$, and $0 \leftrightarrow J = 2, 4, 6$. However through crystal field mixing of *J*, these rules are relaxed to some extent. Hence transitions such as the $^7F_0 \rightarrow {}^5D_1$ excitation and the $^5D_0 \rightarrow {}^7F_3$ emission are often detected [9] in particular centres of Eu^{3+} in various hosts.

Further selection rules depending upon the polarisation of excitation light are derived from the group theory for transitions in specific symmetry centres. Here we consider two polarisations with respect to the orientation of the electric field vector. For π polarised light the E vector is parallel to the principal axis which is the z-axis of the symmetry of lanthanoid centres. In the case of σ polarised light, the E vector is perpendicular to the z-axis. Also notations of π′ and σ′ are used when the magnetic field vector is parallel and perpendicular to the z-axis. Now the polarisation property of transitions can be determined by the irrep multiplication. For example, a transition under study is allowed through electric dipole process if the multiplication of irreps of the initial state and the dipole operator contains the irrep of the final state, as $\Gamma_i \times \Gamma_P^{op} \supset \Gamma_f$, where *P* is either σ or π. It should be noted that irreps D_J^- and D_J^+ of the full rotation group O_3 can be used as appropriate irreps for the electric dipole (odd parity) and magnetic dipole (even parity) operators, respectively. Further the irreps decompose differently from O_3 to the C_{3v}

symmetry according to the σ and the π polarisations. Hence the irreps of transitions operators (J = 1) in C_{3v} can be written as,

$$D_1^- \rightarrow A_{1g}(\pi) + E_g(\sigma),\ D_1^+ \rightarrow A_{2g}(\pi') + E_g(\sigma').$$

Whether a transition is allowed, as well as its polarisation nature, can be inferred from appropriate irrep multiplication by Butler [10], for example. The resulting polarisation transition selection rules for the C_{3v} symmetry are summarised in table 5.1. For example, an excitation transition from the A_{1g} level to the E_g of Eu^{3+} in the C_{3v} symmetry centre is allowed through electric dipole (σ) and magnetic dipole (σ′) process. However an excitation (or emission) transition from the A_{1g} to the A_{2g} is only allowed through magnetic dipole process in which the magnetic field vector is parallel to the z-axis. The polarised excitation and emission technique was used in this study when site symmetry is not known for Eu^{3+} centres in nano scale films and superlattices.

Table 2.5. Polarisation transition selection rules for Eu^{3+} ion in the C_{3v} symmetry.

C_{3v}	A_{1g}	A_{2g}	E_g
A_{1g}	π	(π′)	σ (σ′)
A_{2g}	(π′)	π	σ (σ′)
E_g	σ (σ′)	σ (σ′)	π, σ (π′, σ′)

References

[1] P. C. Becker, N. A. Olsson, J. R. Simpson, *Erbium-Doped Fiber Amplifiers*: Academic Press, 1999.

[2] *Handbook on the Physics and Chemistry of Rare Earths*, vol. 37. Amsterdam: North-Holland, 2007.

[3] B. G. Wybourne, *Spectroscopic Properties of Rare Earths*: John Wiley & Sons, Inc., 1965.

[4] *Crystal Field Handbook*. Cambridge: Cambridge University Press, 2000.

[5] G. H. Dieke, *Spectra and Energy Levels of Rare Earth Ion in Crystals*. New York: Interscience Publishers, 1968.

[6] C. W. Neilson, G. F. Koster, *Spectroscopic Coefficients for p^n, d^n and f^n Configurations*: MIT Press, 1963.

[7] V. Heine, *Group theory in Quantum Mechanics*. New York: Dover Publications, Inc., 1993.

[8] *Laser Spectroscopy of Solids*, vol. 49, Second ed. Heidelberg: Springer-Verlag, 1986.

[9] J. P. Jouart, M. Bouffard, G. Klein G. Mary, "Cubic Eu^{3+} centres in fluorite-type crystals," *J. Lum.*, vol. 50, pp. 273-277, 1991.

[10] P. H. Butler, *Point Group Symmetry Applications*. New York: Plenum Press, 1981.

Chapter 3

Experimental consideration

3.1 MBE grown samples

CaF_2:Eu-CdF_2 superlattices (SLs) and CaF_2:Eu thin films have been grown at Ioffe Institute, Russia by a molecular beam epitaxy (MBE) technique. 'Molecular beam' is defined as a directed ray of neutral molecules or atoms in a vacuum system. For the growth of these SLs, molten materials of CaF_2:Eu and CdF_2 in different effusion cells were sequentially deposited on a heated silicon (Si) substrate in an ultrahigh vacuum environment. The substrate was [111] oriented and its temperature was kept at 700º C for a good growth. The opposite signs of the fluoride lattice mismatches with Si allow pseudomorphic growth of the layers. For all samples, several mono layers of CaF_2 were deposited on top of the Si substrate allowing subsequent coherent growth of CaF_2:Eu layers. In general CaF_2 crystals with a concentration of 0.1~0.5% of divalent Eu ions were used for the growth which then results in a uniform distribution of Eu ions throughout the layers of CaF_2 as shown in fig. 3.1.

For the SLs, the sequential deposition of a CaF_2:Eu layer and CdF_2 layer is defined as a growth parameter 'period'. In general the number of periods in a film is inversely proportional to the thickness of deposited layers. For a symmetric SL consisting of five mono layers (1 ML = 3.15 Å) of CaF_2:Eu and 5 ML of CdF_2, the number of periods was about 30. On the other hand, the number of periods for a SL of $(CaF_2{:}Eu)_{20ML}$-$(CdF_2)_{20ML}$ was about 8. Hence the total thickness of the SLs is comparable and moreover the photoluminescence (PL) intensity of Eu centres is also comparable.

In addition to the symmetric SLs, asymmetric SLs which consist of different thicknesses of CaF_2 and CdF_2 layers were grown. The overall thickness of the SLs consists of 1-2 ML roughness judged by a high resolution transmission electron microscopy data [1]. The concentration of Eu, thickness and the number of periods of frequently used samples for this project are summarised in table 3.1.

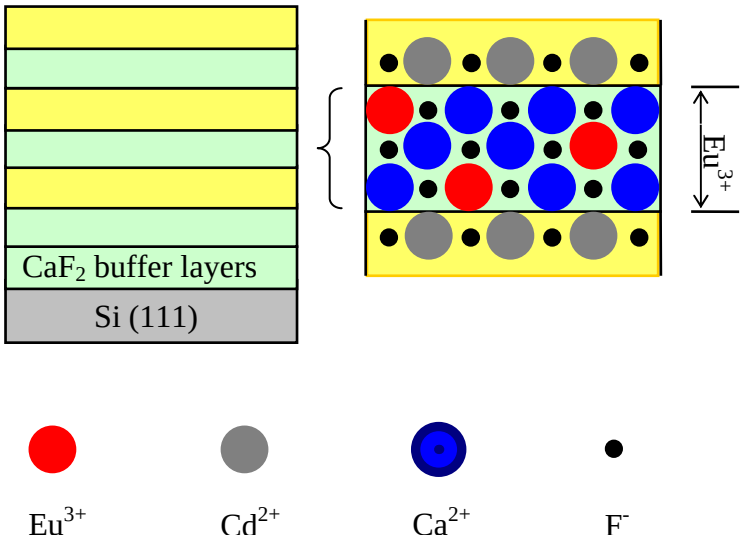

Fig 3.1. Schematic of CaF_2:Eu-CdF_2 deposition. Eu ions are uniformly deposited in the CaF_2 layers.

Table 3.1. Specification of investigated samples.

Sample code	Eu concentration (mol. %)	Thickness of layers (expressed as subscript)	Number of periods
SL1885	CaF_2:Eu 0.3%	$(CaF_2)_{2ML}$-$(CdF_2)_{2ML}$	60
SL3173	CaF_2:Eu 0.1%	$(CaF_2)_{3ML}$-$(CdF_2)_{3ML}$	50
SL3172	CaF_2:Eu 0.1%	$(CaF_2)_{5ML}$-$(CdF_2)_{5ML}$	30
SL1646	CaF_2:Eu 0.5%	$(CaF_2)_{20ML}$-$(CdF_2)_{20ML}$	8
ASL1980	CaF_2:Eu 0.4%	$(CaF_2)_{4ML}$-$(CdF_2)_{2ML}$	50
ASL1982	CaF_2:Eu 0.3%	$(CaF_2)_{2ML}$-$(CdF_2)_{4ML}$	50

3.2 Combined excitation-emission spectroscopy

As shown in fig. 3.1, the Eu centres deposited in different CaF_2 layers may form different energy level configurations due to their unique crystal environments. Also for consideration of charge compensation in Eu^{3+} centres we require a tunable excitation source so that only a particular centre of Eu^{3+} is excited. The combined excitation-emission spectroscopy (CEES) enabled us to continuously excite Eu^{3+} centres while observing their corresponding PL through a CCD detection.

3.2.1 Dye laser

The dye laser used in this study consisted of two parts, a laser head and a circulator. Since the dye laser is a liquid state laser, the Coherent model 591 circulator was used to provide a stream of dye solution to the laser cavity. The circulator was water cooled to prevent overheating of the solution. The dye solution was prepared by dissolving Pyrromethene 546 into a mixture of ethylene glycol and benzene-alcohol. The laser was optically pumped by the 488 nm line of the Spectra-Physics model 2080 argon laser with an output of 3 W. With a birefringent filter installed in the cavity, the dye laser output was ~100 mW at ~525 nm which is the transition wavelength of the $^7F_0 \rightarrow {}^5D_1$ of Eu^{3+} as shown in fig. 3.2. The birefringent filter was coupled with a mechanical stepper motor so that the output wavelength was tuned by appropriate programmes. The dye solution became unstable after ~300 hours of operation resulting in degraded performance. The maintenance of the dye laser was carried out by cleaning the optics and the circulator. Upon the cleaning, the circulator was filled with a fresh batch.

3.2.2 CCD equipped spectrometer

The Triax 320 spectrometer with an F number of F/4.1 was used for the emission study. The spectrometer is equipped with the Jobin Yvon 3000 charged coupled device (CCD) detector at the exit slit of the spectrometer. The CCD was cooled with liquid nitrogen to

minimise thermal noise. A grating of 1800 lines/mm was frequently used to observe the $^5D_0 \rightarrow {}^7F_1$ emission of Eu^{3+}. For that grating the spectral coverage with the 26.7 mm (1024 pixels) CCD was ~30 nm giving a resolution of 0.03 nm. The time of exposure of the emission onto the CCD was controlled by a mechanical shutter fitted in the entrance slit of the spectrometer.

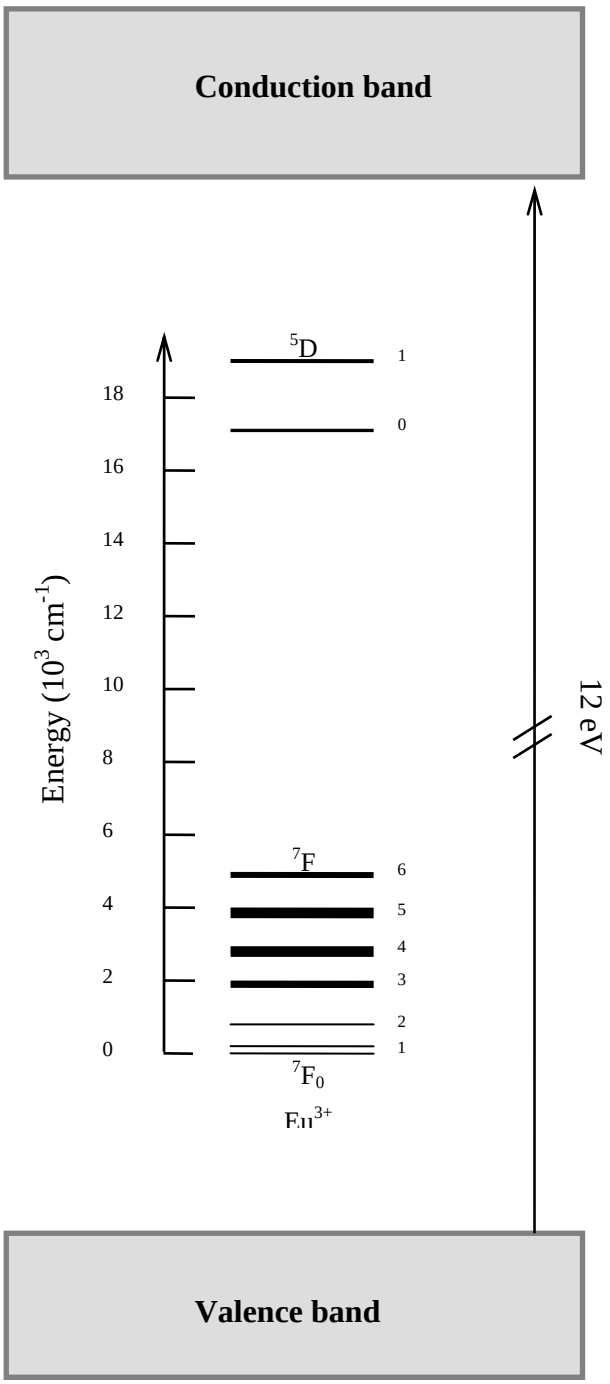

Fig. 3.2. Energy levels of the Eu^{3+} inside the band gap of CaF_2. The values of the energy levels are taken from ref. [2].

3.2.3 Data acquisition

Labview was used to control the software for the CCD-spectrometer in connection with the dye laser stepper motor in order to perform CEES. The dye laser stepper motor was designed to move to the next position while the CCD-spectrometer's shutter is closed. Sequentially when the shutter is open, the new excitation wavelength was provided by the dye laser. Hence at each step, the CCD recorded the emission of Eu^{3+} only excited by a particular wavelength provided by that step. The whole process was done continuously and the raw data is stored as a matrix form. The raw data is then represented as two dimensional contour plots generated by Igor Pro or Origin as shown in fig. 3.3. The height of the contour is equivalent as the PL intensity of Eu^{3+} and is indicated by colours. The strong signal is indicated by red and the weak signal is indicated by blue.

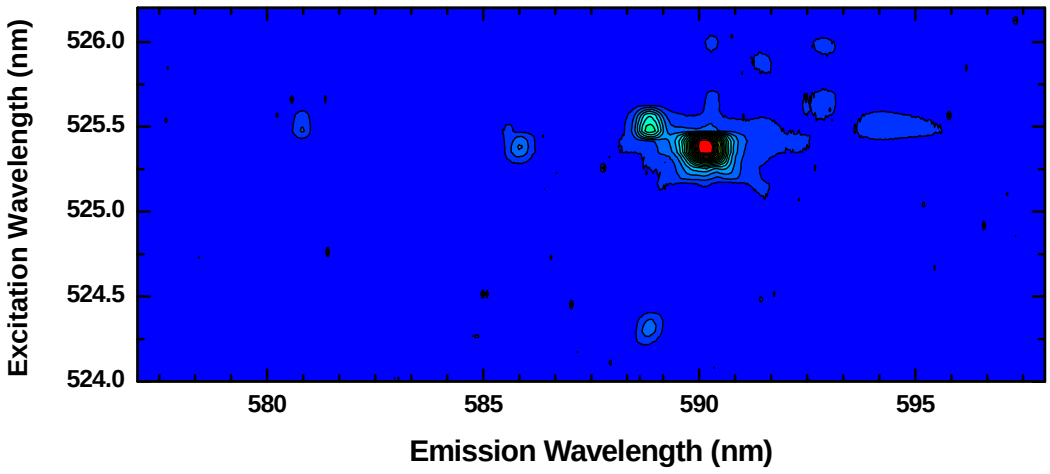

Fig. 3.3. A contour plot of CEES for Eu^{3+} in a SL. Corresponding Eu^{3+} centres are indicated by contours.

For this study the dye laser was tuned over 250 steps which is equivalent of $\Delta\lambda_{exc} \sim 0.5$ nm. The excitation wavelengths were measured by the Burleigh WA-2000 wavemeter with a resolution of 0.02 nm at 525 nm. The excitation wavelengths were linearly increased with the dye laser stepper motor. Hence only the initial and the final wavelengths were measured and the rest of the wavelengths were calculated.

3.3 Cryogenics

To minimise broadening of Eu^{3+} transitions and to occupy electrons to their ground state ($^7F_0$ for Eu^{3+}) an Oxford MicrostatHe cryostat was used in this study to keep the samples at low temperature. A conducting silver paste (1109-s) was employed to place the samples onto a copper sample holder which was then bolted to the base of the cold finger of the cryostat. The cryostat was evacuated using a diffusion pump. Liquid helium was drawn from a dewar and transferred to the cryostat using a dual tube connected with a gas pump. The base temperature of the cryostat was 3.5 K. The temperatures inside the cryostat were precisely controlled by the Oxford temperature controller assisted by a needle valve which controls the helium flow. For this study temperature was varied from 3.5 K to 300 K.

References

[1] N. S. Sokolov, S. V. Gastev, A. Y. Khilko, S. M. Suturin, I. N. Yassievich, J. M. Langer, A. Kozanecki, "Tunneling-assisted autoionization of the localized impurities in nanostructures," *Phys. Rev. B*, vol. 59, pp. R2525-R2528, 1999.

[2] P. C. Becker, N. A. Olsson, J. R. Simpson, *Erbium-Doped Fiber Amplifiers*: Academic Press, 1999.

Chapter 4

Spectroscopy of divalent Eu in CaF_2 thin films and CaF_2-CdF_2 superlattices

4.1 Introduction

It was mentioned in chapter 1 that Eu ions form themselves as optically active ions and therefore as probes to the local environment of crystal hosts. In this chapter, spectroscopy of divalent Eu is discussed in terms of revealing local strain in CaF_2 thin films and CaF_2-CdF_2 superlattices (SLs). Photoluminescence (PL) bleaching of Eu^{2+} in SLs of CaF_2:Eu-CdF_2 is also investigated to elucidate photoionisation in such heterostructures which have a unique band gap structure.

Optical transitions of Eu^{2+} (so-called *f-d* transitions) are electric dipole allowed due to the change of parity. Unlike transitions which take place within the *f* shell (*f-f* transitions), the *f-d* electronic transitions involve the outer 5*d* shell. The radial extent of the 5*d* shell electron wavefunctions is greater than that of the 4*f* shell electrons and the 5*d* electrons are strongly coupled with their crystal environment [2]. Hence absorption and emission involving the *f-d* transitions are often phonon broadened as a result of the large crystal field coupling of the 5*d* electrons [3]. The electric dipole transition is also much more efficient than the magnetic dipole transition. This is given by the fact that transition strength for electric dipole results in higher Einstein transition probability than magnetic dipole transitions [4]. The quantum efficiency of Eu^{2+} is reported as 0.62 [1].

It is well known that *f-d* transitions of Eu^{2+} and Sm^{2+} are strongly dependent on strain associated with thin crystal hosts [5-8]. MBE grown films are subject to strain due to lattice and thermal expansion mismatch to the Si substrate. PL of Eu^{2+} sensing this strain in MBE films and SLs is discussed in section 4.2. In addition to the realisation of the crystal environment of the thin films and SLs, bleaching of Eu^{2+} PL can also be used to reveal interesting physics at the interface of CaF_2-CdF_2 SLs. The photobleaching of Eu^{2+} in various SLs is discussed in section 4.3. Two mechanisms involved with the photobleaching are considered, namely tunnelling and trapping. In section 4.4 a PL growth of Eu^{3+} was discussed as opposed to the bleaching of Eu^{2+}. Here trivalent Eu^{3+} is considered as the product of the photobleaching to confirm that Eu^{2+} not only bleaches but also transforms to the trivalent state. Finally recovery of Eu^{2+} was attempted by means of additional thermal excitation and is discussed in section 4.5.

4.2 The *f-d* transition of Eu^{2+} associated with planar strain in CaF_2:Eu thin films and CaF_2:Eu-CdF_2 superlattices

Eu^{2+} spectra are used in this investigation to survey epitaxial strained MBE grown thin films and SLs. The strain is caused by lattice mismatch between the Si substrate and CaF_2 and CdF_2 layers. The strain associated with heterostructures is defined as a ratio of the difference of lattice parameters between a substrate and a deposited material over the lattice constant of the substrate [9]. Following Sokolov *et al.*, the planar strain, $\varepsilon_{||}$, is written as

$$\varepsilon_{||} = \frac{(a_0 - a_1)}{a_0}, \tag{4.1}$$

where a_0 and a_1 are lattice constants for the substrate and the unstrained deposited layer material, respectively [6]. The planar strain purely depends on the lattice constant and can be expressed as either positive (tensile) or negative (compressive) values. For example, CaF_2 films deposited on Si substrate, $\varepsilon_{||}$ is -0.6% at room temperature since the lattice constant of CaF_2 (5.46 Å) is larger than that of Si (5.43 Å) by 0.6% [10, 11]. Taking into

account that thermal expansions for Si and CaF_2 are different also means $\varepsilon_{||}$ changes with respect to growth temperatures.

In PL spectra the strain is simply observed by the peak shift from its wavelength in a bulk crystal. The strain in bulk is considered as 0% and the zero phonon line (ZPL) of the Eu^{2+} PL peak is taken as a reference unless the crystal is externally compressed. The simplest model is to assume a linear dependence of the Eu^{2+} ZPL wavelength shift on the planar strain $\varepsilon_{||}$ [6];

$$\Delta\lambda = -K\varepsilon_{||}, \tag{4.2}$$

where the K is taken as 200 nm for Eu^{2+} [6]. In this model a red shift occurs for films under compressive strain. Kaplyanskii and Przhevuskii interpreted the physics underlying such observations as perturbations of excited levels caused by the deformation of the crystal field [5]. However Kaplyanskii and Przhevuskii observed the ZPL shift when a uniaxial stress was applied along a [111] direction. Hence equation (4.2) is a link which relates the planar strain and the uniaxial strain.

Optical excitation of Eu^{2+} was provided by a He-Cd laser (λ = 325 nm) which pumps Eu^{2+} from its $4f^7$ ground state to the $4f^6 5d$ (e_g) absorption band of closely spaced levels in a cubic crystal field [1]. Two absorption bands, e_g and t_{2g}, were reported with values of ~28,000 cm^{-1} and ~45,000 cm^{-1}, respectively [12]. After excitation a non-radiative relaxation follows to the lowest ^2E (Γ_8) state from which a radiative emission to the ground state occurs[1, 3]. Energy levels of the Eu^{2+} allowing $4f^7 \leftrightarrow 4f^6 5d$ transitions are schematically shown in fig. 4.1.

The PL spectrum of the *f-d* transition of Eu^{2+} in a CaF_2 bulk crystal is presented in fig. 4.2. The spectrum consists of a sharp line at 413 nm and broad features at longer wavelengths. The emission was recorded with a CCD detection at ~4 K. The sharp peak is an electric dipole transition ($4f^6 5d \rightarrow 4f^7$) of Eu^{2+} and the broad features are phonon-assisted transitions. The *f-d* transition allows Eu^{2+} to interact with crystal lattice vibrations and such interaction is exhibited as broad features. However the pattern of the phonon-

assisted transitions is almost the same for all film samples and bulk crystal [13]. Also the PL position of the entire phonon-assisted transitions shifts correspondingly to the position of the ZPL. For that reason only the ZPLs were extracted from all observed spectra and were compared.

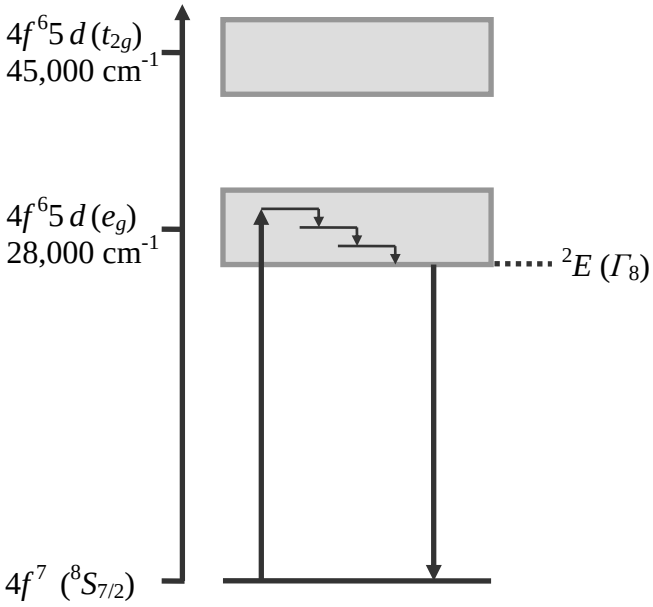

Fig. 4.1. Energy level diagram for the $4f^7 \rightarrow 4f^6 5d$ transitions of Eu^{2+}. The values and the symmetry assignments are taken from references [1, 3, 12].

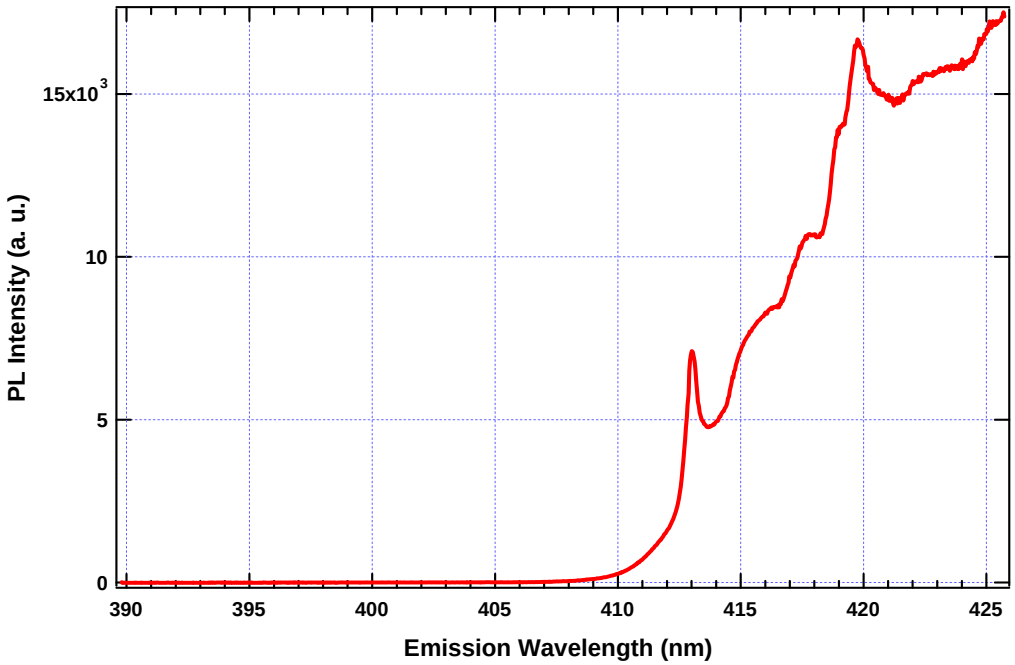

Fig. 4.2. The PL spectrum of Eu^{2+} doped in a CaF_2:Eu bulk crystal with a He-Cd laser as the excitation source. The emission was recorded at ~4K

Fig. 4.3 shows peak positions of the ZPL of Eu^{2+} doped in various films, a SL and a bulk crystal. It was observed that PL peaks were either blue or red shifted suggesting some degree of strain introduced in all films. A red shift of 0.70 nm was observed for the PL peak of a $(CaF_2{:}Eu)_{20}$-$(CdF_2)_{20}$ SL where the subscript represents the thickness of a single CaF_2 layer expressed in mono layers (ML). For thin films blue shifts of 1 nm and 2.24 nm were observed for 290 nm thick and 70 nm thick films, respectively.

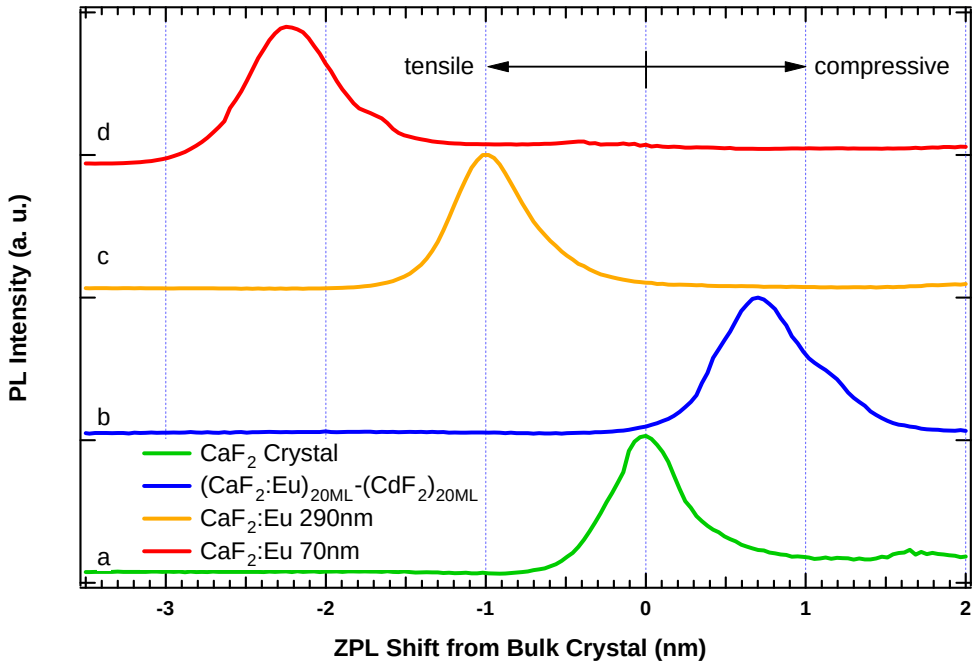

Fig. 4.3. Normalised ZPL photoluminescence peaks of Eu^{2+} doped in (a) bulk crystal, (b) a CaF_2:Eu-CdF_2 SL, (c) a 290 nm thick CaF_2:Eu film and (d) a 70 nm thick CaF_2:Eu film. The horizontal axis is rescaled to the bulk PL peak.

The PL peak shifts are somewhat thickness dependent suggesting that the strain is also influence by the thickness of samples. However the strain is rather distributed in either positive or negative sides of the bulk peak preventing precise investigation. According to Gastev *et al*. [14], the strain generally becomes compressive for thin films (~10 nm) and tends to be tensile as the thickness increases. However when the thickness of an MBE film exceeds its critical thickness, d_{cr}, which is the pseudomorphic growth limit, then the strain tends to relax. It is evident in fig 4.3 (c) that the thicker film exhibits a more relaxed strain than the thinner film (fig 4.3 (d)). The strains measured using equation (4.2) have shown good agreement with the literature [8]. The results for the strain of the samples are summarised in table 4.1. The calculation suggested in ref. [8] is also presented in the table.

Note that for the SL sample, the thickness is that of a single CaF_2 layer of 20 ML as the strain is reinitiated by the barrier CdF_2 layer.

Table 4.1. Strain measured for sample films and SL.

Sample	Thickness (nm)	Peak shift (nm)	Strain (%)
$(CaF_2:Eu)_{20}$-$(CdF_2)_{20}$ (SL 1646)	6.3*	0.70 ± 0.02	-0.35 (-0.33)**
CaF_2:Eu (TF 1978)	290	-1.00 ± 0.02	0.49 (0.47)
CaF_2:Eu (TF 1977)	70	-2.24 ± 0.02	1.12 (1.05)

*The thickness is a single layer of 20 ML thick CaF_2. The thickness of a ML is taken as 3.15 Å from reference [14].

**Note that the values inside brackets were calculated using the formula taken from ref. [8].

In addition to the strain related shift in the ZPL in thin films and SLs, a splitting in the ZPL was also observed in a 650 nm thick film. Fig. 4.4 shows ZPLs of the Eu^{2+} for two different excitation spot positions. At a particular spot position there was a splitting in the ZPL but this was not observed, as the incident laser was moved to the other spot (fig. 4.4(b)). The splitting in the ZPL is only observed from this particular sample. We did not observed any splittings from thin films. However the planar strain for this sample is thought to be minimised as the ZPL shift is least among the samples. Hence the splitting is possibly due to other factors than the planar strain.

The splitting in the ZPL was further analysed by performing multi peak fittings using Igor Pro. The line shape of the ZPLs was described as Gaussian curves. Two Gaussian curves were used in the fitting process and gave a value of the spectral splitting of 0.49 nm or an energy separation equivalent to 28.8 cm^{-1} between the peaks (fig. 4.4(a)). It is known that the ZPL of Eu^{2+} splits into a doublet when the crystal is stressed along a [100] or [110] axis [5, 8]. The observation of the ZPL splitting reflects that the strain is not uniform throughout the film and at certain localised areas there is another strain associated with an axis other than the [111] direction.

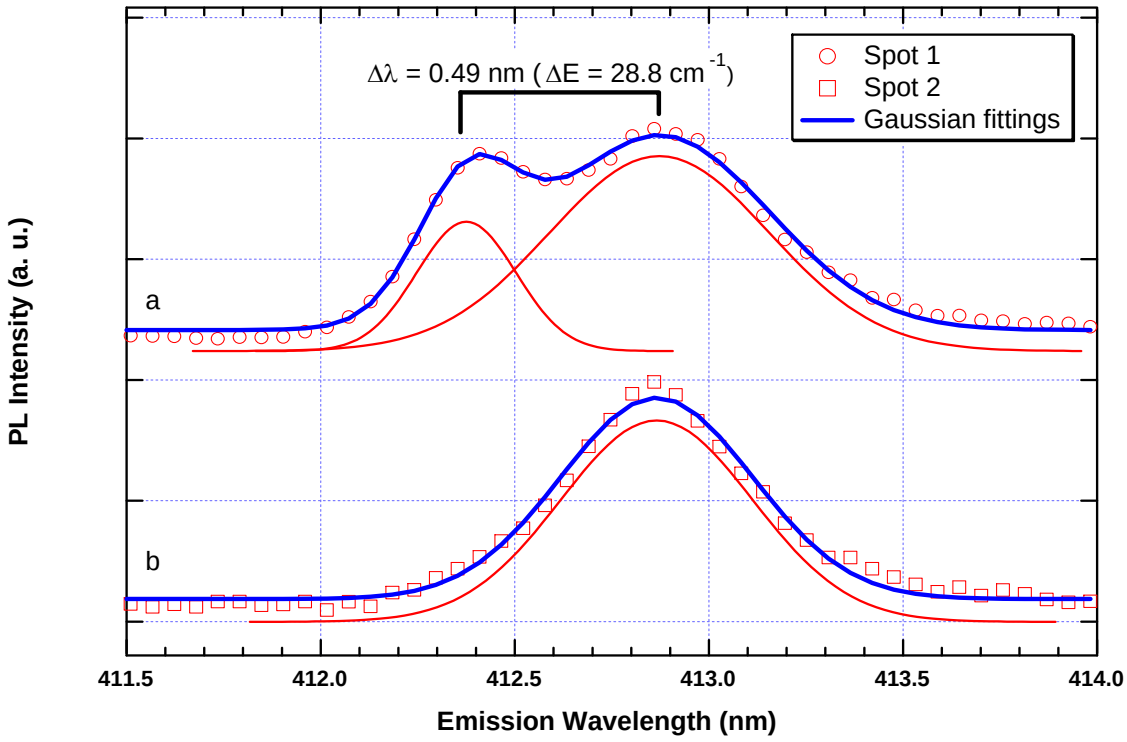

Fig. 4.4. (a) Splitting in the ZPL of Eu^{2+} in a 650 nm thick film (TF 1683). (b) The same condition at a different spot of the thin film. The spectra are only being different by means of excitation spot position. The ZPL of bulk crystal is at 413 nm.

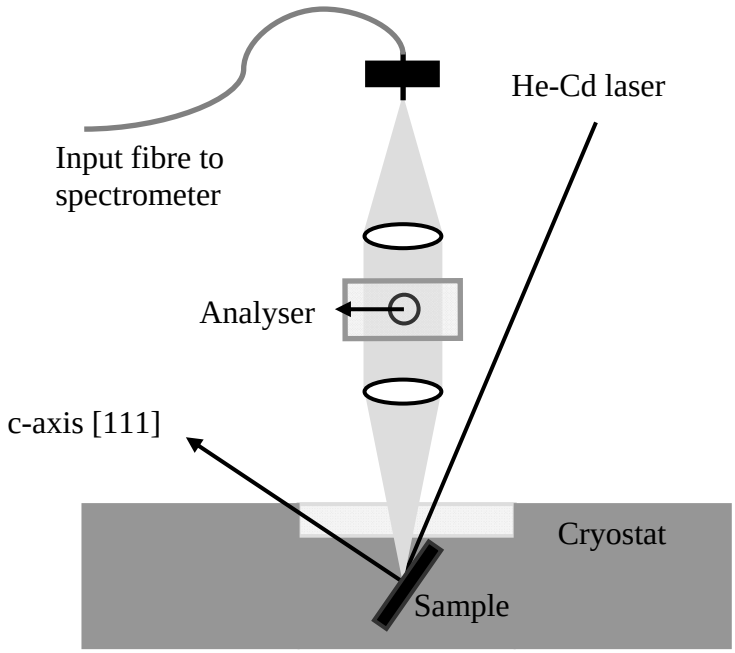

Fig. 4.5. Schematic of polarised emission set up. The E vector of the incident laser is polarised perpendicular to the c axis (E ⊥ c).

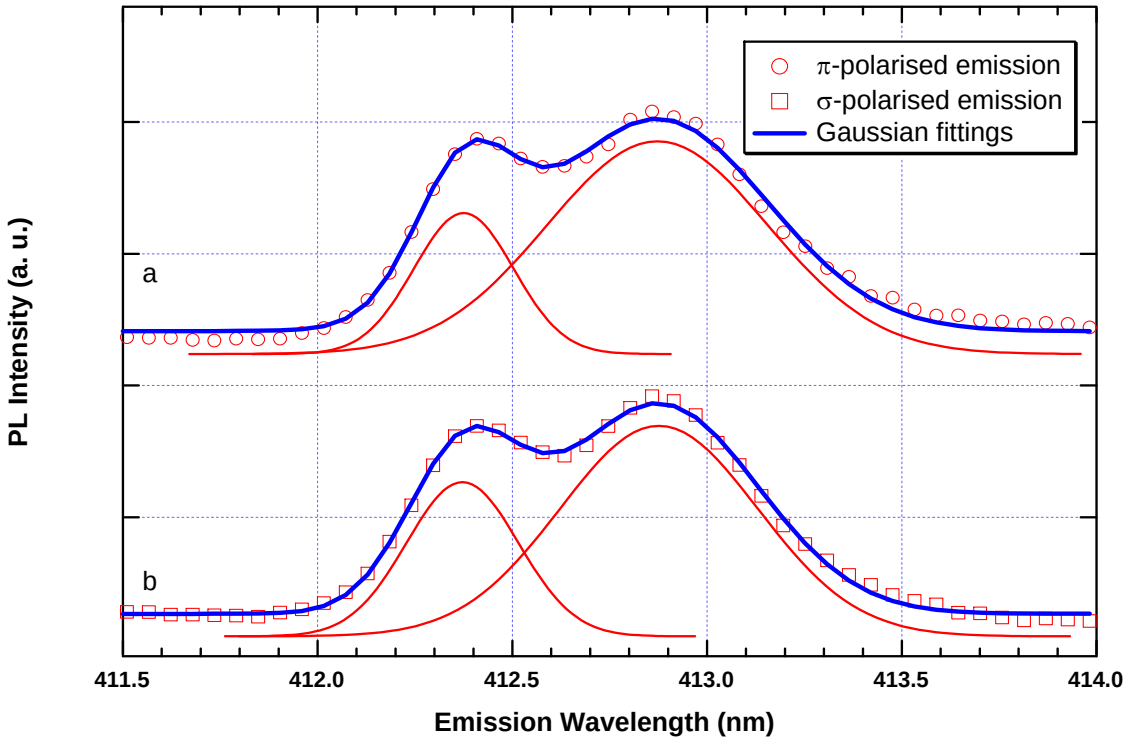

Fig. 4.6. Polarised emission of the ZPLs of Eu^{2+} in a 650 thick film of CaF_2:Eu (TF1683). (a) π-polarised emission and (b) σ-polarised emission off the same spot of laser excitation.

Polarised emission was also carried out by having the c axis of the film oriented ~60º inside the cryostat and employing an analyser in the emission path as shown in fig. 4.5. Fig. 4.6 shows the polarised emission spectra of the split ZPL in the thin film (TF 1683). It was observed that the emission pattern of the ZPL splitting almost identical for both polarisations. It is reasonable to speculate that the excited state is possibly split as there is no drastic change in the emission spectra.

It is assumed that the states allowing $4f^6 5d \rightarrow 4f^7$ transitions have mixed configuration arising from coupling of the 5*d* electrons to the $4f^{n-1}$ core [3, 5, 12]. In other words, low lying $^7F_{J(1\rightarrow 6)}$ spin-orbit multiplets of the $4f^6$ core levels are coupled to the e_g and t_{2g} orbitals of the 5*d* electron. As a result a spin orbit quartet, Γ_8, the lowest lying state is produced in the $4f^6 5d$ configuration (fig. 4.1). The splitting in the ZPL is due to the reduction of the symmetry in the excited states caused by strain [5]. In fact the crystal symmetry of the Eu^{2+} ground state is cubic, O_h, hence no splitting is expected in that state. However the excited state Γ_8 can be split under deformation of the crystal field symmetry.

No attempt was made to measure the strain associated with an axis other than [111] in this study as the splitting in the ZPL is only seen in that particular thick film and at particular spots. Also the position of the single ZPL of that sample says that the film is under tensile strain and the behaviour of the splitting in the Γ_8 state under tensile strain is yet to be investigated.

In summary, an *f-d* transition of Eu^{2+} served as a measuring tool for the strain in MBE grown films and SLs. The ZPL of each sample was either red or blue shifted from the bulk reference. The strain involved with the SLs and thin films was calculated. The 20 ML thick SL shown a compressive strain (0.35%) and other thin films showed tensile strain of 0.49% and 1.12%, respectively for 290 nm and 70 nm thick films. The reason that the SL has a compressive strain is that the host thickness is still thin so that the coherent growth with Si is allowed (which results in a compressive strain).

The ZPL of Eu^{2+} was also split in the 650 nm thick film. The splitting was measured as 28.8 cm^{-1} in the tensile stressed film. The observation of the split ZPL indicates that the strain associated with a thick film is not uniform.

4.3 Photoluminescence bleaching of Eu^{2+} in CaF_2:Eu-CdF_2 superlattices and CaF_2:Eu thin films

It is well known for many decades that crystals doped with defects, such as lanthanoids, exhibit photobleaching effects. Examples are associated with transfer of charge from one dopant to another [15-17] and with hole burning processes [4, 18]. However, regardless of the various mechanisms of the photobleaching, photoionisation is a significant contributing factor.

Previously PL bleaching of singly doped Eu^{2+} under UV excitation in CaF_2:Eu-CdF_2 has been reported by Sokolov *et al*. [14, 19]. In these particular heterostructures a conduction band offset of 2.9 eV [20] exists between CaF_2 (12.1 eV) and CdF_2 (8 eV). A schematic diagram of these energy band gaps is depicted in fig. 4.7. The excited state, e_g, of Eu^{2+}

lies inside the band gap of CaF_2. Hence the excited state is in resonance with the conduction band of CdF_2 because the bottom of the CdF_2 conduction band is lower than that of the CaF_2. The bleaching is thought to be an ionisation of Eu^{2+} followed by tunnelling and then localisation of electrons in the CdF_2 layer.

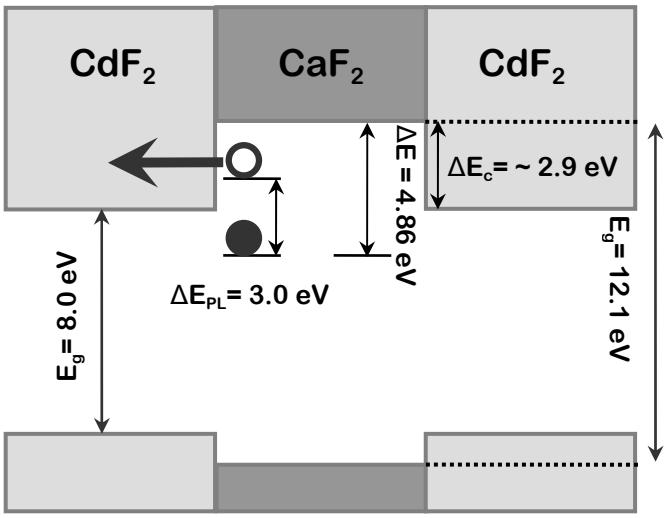

Fig. 4.7. Schematic of the excited state of Eu^{2+} in CaF_2. Band gaps of CaF_2 and CdF_2 are 12.1 eV and 8.0 eV, respectively. The conduction band offset between CaF_2 and CdF_2 is ~2.9 eV given by x-ray photoelectron spectroscopy. The excited state of Eu^{2+} is in resonance with the conduction band of CdF_2. The energy difference between the ground state of Eu^{2+} and the conduction band is taken from ref. [1]

There exists a finite probability of electron tunnelling since the wavefunctions of electrons in the Eu^{2+} excited state can extend to the conduction band of CdF_2. Some of the Eu^{2+} ions in the vicinity of the neighbouring CdF_2 are likely to be ionised to Eu^{3+} given that appropriate energy is provided. There will be Eu^{2+} remaining unchanged in the middle of the CaF_2 layers as the distance from the interfaces is too far for electrons to tunnel. The overall number of Eu ions is unchanged while their state of valence is possibly converted from divalent to trivalent during the UV excitation.

It needs to be considered whether the direct promotion of electrons from Eu^{2+} to the conduction band of CaF_2 takes place under UV excitation. Pedrini *et al*. [21] measured photoionisation thresholds for several divalent rare earth dopants (Tm, Ho, Dy) in MF_2 hosts where M = Ca, Ba, Sr. They interpreted the photoionisation threshold as equivalent to the energy difference between the ground state of the rare earths and the conduction band of CaF_2. Owen *et al*. [1] used the model of Pedrini *et al*. [22] to calculate the energy difference between the ground state of Eu^{2+} and the conduction band as 4.86 eV or equivalent to 39,000 cm^{-1}. However, Pedrini *et al*. later observed that the photoionisation

threshold for Eu^{2+} doped CaF_2 is at 3.8 eV. It was also claimed that the absorption of a photon into the first excited state of Eu^{2+} (e_g) does not lead to release of electrons to the conduction band.

The excitation source of the bleaching effect used by Sokolov *et al*. was a 337 nm line of a N_2 laser which is just below the threshold (3.68 eV or 29,700 cm^{-1}). This means that the excitation energy is not energetically high enough to promote electrons in the ground state of Eu^{2+} directly to the conduction band of CaF_2. According to Pedrini *et al*., the transition to the e_g state should not result in bleaching of Eu^{2+} PL for a CaF_2 crystal. In fact this is the case for bulk crystal of CaF_2:Eu. However for CaF_2:Eu-CdF_2 SLs the PL bleaching is observable. One can therefore expect a new physical phenomenon related to tunnelling in this type of heterostructure.

To verify the photobleaching of Eu^{2+} an experiment was carried out with similar manner and samples as described by Suturin *et al*. [23]. A He-Cd laser was used to pump Eu^{2+}at a wavelength of 325 nm. Eu^{3+} ions were simultaneously excited by a tunable dye laser and their emission detected by the CCD-spectrometer system. A mechanical chopper was used to suppress the strong dye laser line in the CCD detection range. The dye laser excitation was fixed at the cubic centre transition ($^7F_0 \rightarrow {}^5D_1$) wavelength. It was necessary to monitor Eu^{3+} transitions simultaneously to demonstrate that the product of Eu^{2+} photoionisation is Eu^{3+} [24, 25]. With the CCD detection a simultaneous monitoring of both Eu^{2+} and Eu^{3+} emission was able to be observed with elapsed time of UV exposure.

Figure 4.8 shows the spectra recorded of Eu emission at two instant times of the continuous UV excitation. It is clearly observed that the PL intensity of Eu^{2+} decreased significantly over 580 s of UV laser exposure. As described in the previous section Eu^{2+} transitions consist of a ZPL at 413 nm and phonon-assisted broad features at longer wavelengths. Even though Eu^{2+} was excited with much less intense laser power the excitation had to be lowered due to the more efficient luminescence than Eu^{3+}. Hence the He-Cd laser output had to be adjusted to avoid saturation of the CCD detector by using a series of neutral density filters.

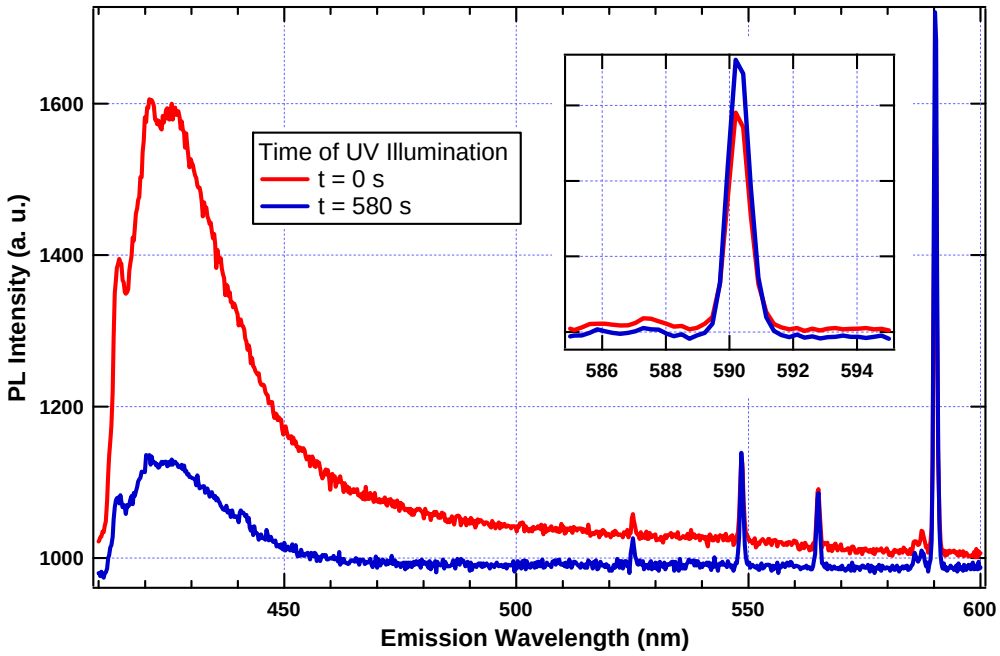

Fig. 4.8. PL spectra of Eu^{2+} and Eu^{3+} in a $(CaF_2{:}Eu)_{20}$-$(CdF_2)_{20}$ SL (SL1647) measured at (a) time of 0 s and at (b) time of 580 s of UV exposure. The broad features at shorter wavelengths are Eu^{2+} transitions and narrow peaks between 548-590 nm are Eu^{3+} transitions. Inset is Eu^{3+} transition ($^5D_0 \rightarrow {}^7F_1$) magnified in horizontal axis. Note that dye laser excitation is also shown (~525 nm) in the figure, significantly suppressed by optical chopping. PL measurements were done at ~4 K.

In fig. 4.8, the Eu^{3+} transitions are the narrow peaks at 548.48 nm, 565.12 nm and 590.19 nm which correspond to the $^5D_1 \rightarrow {}^7F_2$ (T_{2g}), $^5D_1 \rightarrow {}^7F_2$ (E_g) and $^5D_0 \rightarrow {}^7F_1$ transitions, respectively. The weak dye laser scatter is also present in the PL spectra at 525.37 nm.

In contrast to the Eu^{2+} PL spectra an increase in PL intensity was observed from all Eu^{3+} transitions during the same time of UV excitation. The most intense Eu^{3+} transition ($^5D_0 \rightarrow {}^7F_1$) is shown in the inset of fig. 4.8. The interpretation is that the bleaching of Eu^{2+} emission is a process of photoionisation to Eu^{3+}. However, it was necessary to verify that the UV laser does not directly promote Eu^{3+} transition intensity. This was carried out in two ways. Firstly, Eu^{3+} emission was measured with only the UV laser excitation, i.e. no resonant dye laser light. No Eu^{3+} transitions were observed under sole UV excitation. Secondly bulk CaF_2:Eu was used under the same experimental conditions. In the presence of UV excitation, the PL intensity of the cubic Eu^{3+} centre excited by the dye laser in the bulk crystal was constant over a period of time. These results suggest that the UV laser

neither directly pumps Eu^{3+} to its excited states nor influences Eu^{3+} emission intensity. The UV excitation, however, possibly provoked some other interactions to occur in SLs. The observation presented in fig. 4.8 is specific to SLs and is not observed in bulk crystals for the above experimental conditions.

PL decay and increase respectively for Eu^{2+} and Eu^{3+} were then monitored continuously with respect to the time of UV exposure as shown in fig. 4.9. The PL behaviours can be described as exponential decay and growth, respectively for Eu^{2+} and Eu^{3+}. It seemed that rate of Eu^{2+} PL bleaching is almost the same as the rate of PL growth for Eu^{3+}. It was suggested that Eu^{2+} ionisation is responsible for this behaviour and the process can be written as,

$$\mathrm{Eu}^{2+} \xrightarrow{h\upsilon} \mathrm{Eu}^{3+} + e^{-}_{trap,tunnel}, \tag{4.3}$$

where $h\upsilon$ is given by the He-Cd laser excitation (325 nm). Here Eu^{2+} oxidises to Eu^{3+} and releases an electron. The reaction is forward-biased until the steady state is reached based on the observation.

The PL behaviour of Eu^{2+} was exponential decay as shown in fig. 4.9. Two channels resulting in Eu^{2+} quenching were considered, namely tunnelling and trapping. Liberated electrons in equation (4.3) are subject to possible tunnelling to CdF_2 layers [19] and to be trapped by impurities in CaF_2 layers [23]. The PL intensity, *I(t)*, of Eu^{2+} with respect to time can be expressed as below,

$$I(t) = A\exp(-p_1 t) + B\exp(-p_2 t) + C,$$
$$A = \frac{N_{tunnel}}{N}, B = \frac{N_{trap}}{N}, C = \frac{N_{rem}}{N}. \tag{4.4}$$

The coefficients A and B are fractions of Eu^{2+} quenched via tunnelling and trapping, respectively. They can be defined as number density ratios of Eu^{2+} ions that are tunnelling (N_{tunnel}) and trapping (N_{trap}) over the whole optically excited Eu^{2+} population N. The coefficient C (N_{rem}) represents the portion of Eu^{2+} remaining unchanged. For normalised

PL intensity the summation of the three coefficients, *A*, *B*, and *C*, must be 1. Two decay parameters were used to fit the PL decay for Eu^{2+}, namely p_1 and p_2, respectively for tunnelling and trapping. A bi-exponential fitting was provided by Igor Pro which generated a good fit result with χ^2 value of 0.027 as shown in table 4.2 and in fig. 4.10.

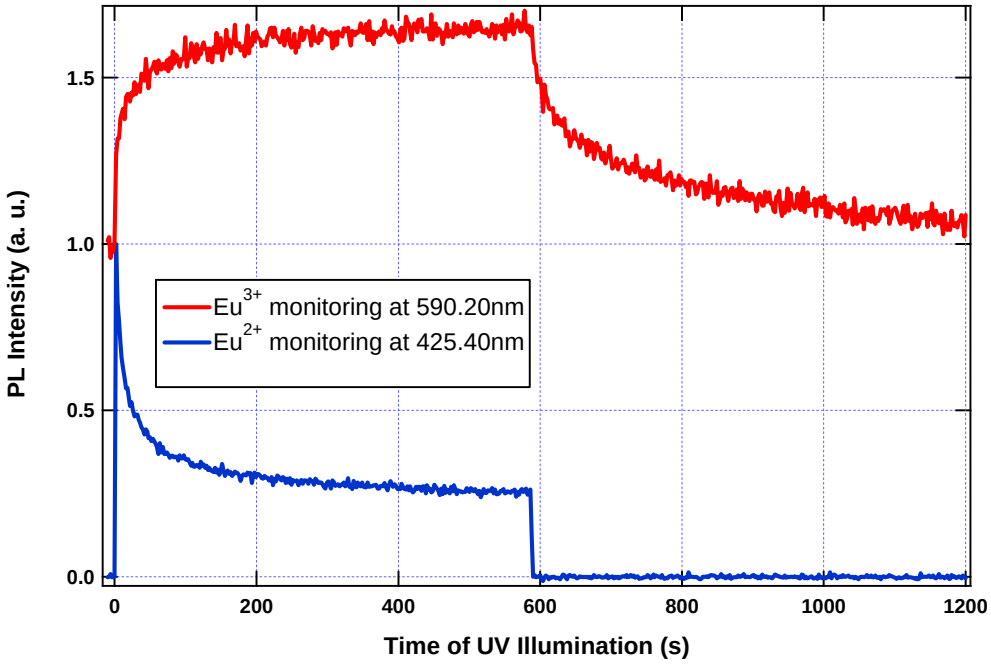

Fig. 4.9. Normalised PL intensity of Eu^{2+} and Eu^{3+} in a $(CaF_2{:}Eu)_{20}$-$(CdF_2)_{20}$ SL (SL1647) with time of UV excitation. The Eu^{2+} PL intensity was monitored at the peak of broad emission (425.40 nm) and Eu^{3+} was monitored at 590.20 nm (the $^5D_0 \rightarrow {}^7F_1$ transition of cubic centre). The UV laser is blocked just before 600 s.

Table 4.2. Summary of fitting parameters and coefficients using (4.4) for SL1647.

Coefficients		Parameters (s^{-1})	
A	0.45 ± 0.01	p_1	0.105 ± 0.004
B	0.24 ± 0.01	p_2	0.0093 ± 0.0003
C	0.260 ± 0.001	$\chi^2 = 0.027$	

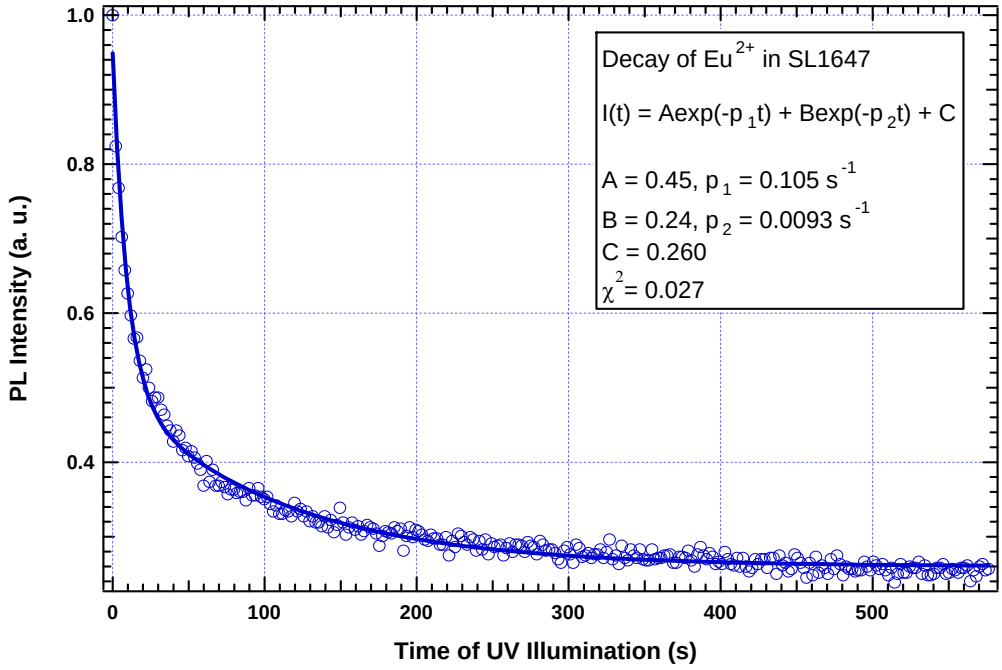

Fig. 4.10. Bi-exponential fitting of Eu^{2+} decay during UV excitation for SL 1647. All parameters are presented in the inset of the figure.

A further investigation on the PL bleaching was carried out using a selectively Eu-doped SL $(CaF_2\text{-}CaF_2\text{:Eu-}CaF_2)_{60}\text{-}(CdF_2)_{60}$. In such SL, Eu ions were only deposited in the middle of the 60 ML CaF_2 layers and were separated from CdF_2 by a distance of 20 ML. Henceforth such a SL that has isolated layers of Eu is named as an Isolated Superlattice (ISL). The same fitting was provided by Igor Pro in which the decay rates were fixed to the values obtained from the previous fitting where uniformly doped Eu^{2+} was considered as shown in fig. 4.10 and in table 4.2. The coefficients, *A* and *B*, however, were not fixed to see whether the fractions of tunnelling and trapping have been changed in the particular ISL. The bi-exponential fitting gave a good result as shown in fig. 4.11 with χ^2 value of 0.058051. The fitting results are shown in table 4.3. The coefficient *A* which represents the portion of Eu^{2+} bleached in tunnelling has decreased significantly from 0.45 (fig. 4.10) to 0.18 which suggests that the probability of tunnelling is lowered due to the larger distance between Eu activators to the CdF_2 layers. As a consequence, the coefficient *B* which represents the portion of Eu^{2+} bleaching due to trapping has shown an increased value from 0.24 (fig. 4.10) to 0.35.

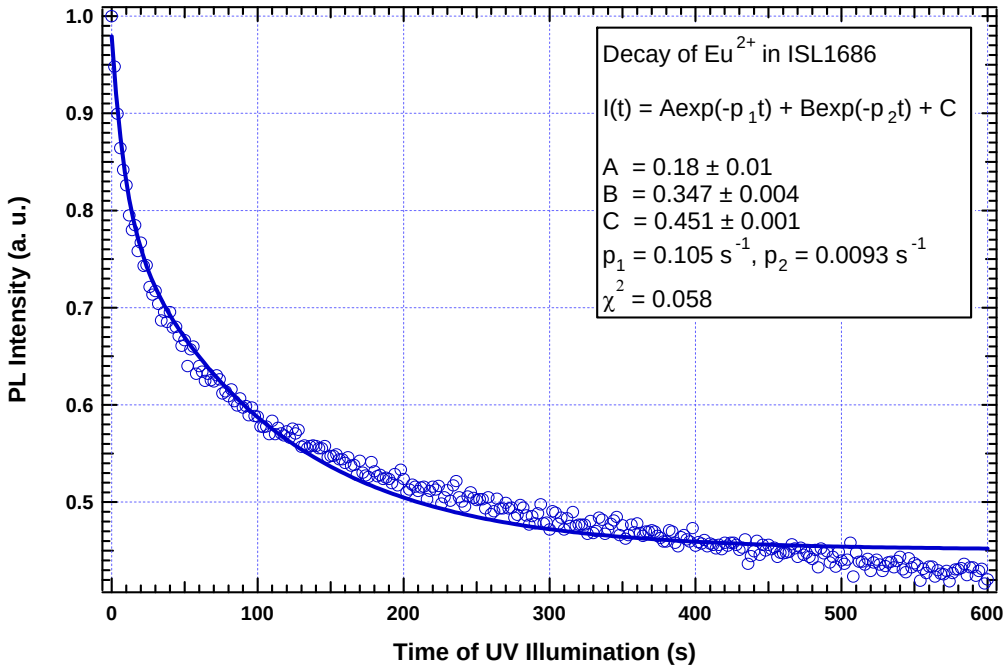

Fig. 4.11. Photobleaching of Eu^{2+} selectively doped in the middle of CaF_2 layer ($CaF_{2(20)}$-CaF_2:$Eu_{(20)}$-$CaF_{2(20)}$)-$(CdF_2)_{(60)}$ in ISL1686. Bi-exponential fitting was used and shown with solid the line. All the parameters and the coefficients are presented in the inset.

Table 4.3. Summary of fitting coefficients and parameters of Eu^{2+} photobleaching in ISL1686.

Coefficients		Parameters (s^{-1})	
A	0.18 ± 0.01	p_1	0.105
B	0.347 ± 0.004	p_2	0.0093
C	0.451 ± 0.001	$\chi^2 = 0.058$	

In the process of quenching, the ionisation of Eu^{2+} due to tunnelling occurs at a faster rate in both SL and ISL. The slow decay rate of Eu^{2+} via trapping was observed in SL and ISL regardless of the coefficients. The change of the coefficients is satisfactorily explained by the role of the 20 ML spacer used in the ISL. This reflects that more Eu^{2+} ions in the ISL lost their chances to be tunnelled than they were in uniformly doped CaF_2 layers (SL1647). It seemed that tunnelling is screened by the additional 20 ML of spacer. The spacer that separates Eu^{2+} from the CdF_2 layer significantly reduces, but does not

completely eliminate the probability of tunnelling. This is possibly due to a result of the deposition of undesired Eu^{2+} inside the 20 ML spacer which gave more probable tunnelling. Alternatively the trapping might be associated with more than one species of impurity inside CaF_2 layers giving bi-exponential decay even though the probability of tunnelling is completely eliminated.

In addition to SL photobleaching, a bi-exponential decay of Eu^{2+} in a CaF_2 thin film was observed. Fig. 4.12 shows the photobleaching decay curve for such a sample. In such a film CaF_2 layers are not sandwiched between CdF_2 layers and are solely deposited on a Si substrate. One might expect that photobleaching behaviour would be described by a single exponential decay in this film corresponding to only the trapping process. However the observed behaviour is similar to that in the SLs and hence the two channels of bleaching still remain valid. A bi-exponential fit to the data is shown in fig. 4.12 using the same decay rates as established earlier. Only the magnitudes of *A*, *B* and *C* were allowed to be varied. The parameters obtained are summarised in table 4.4.

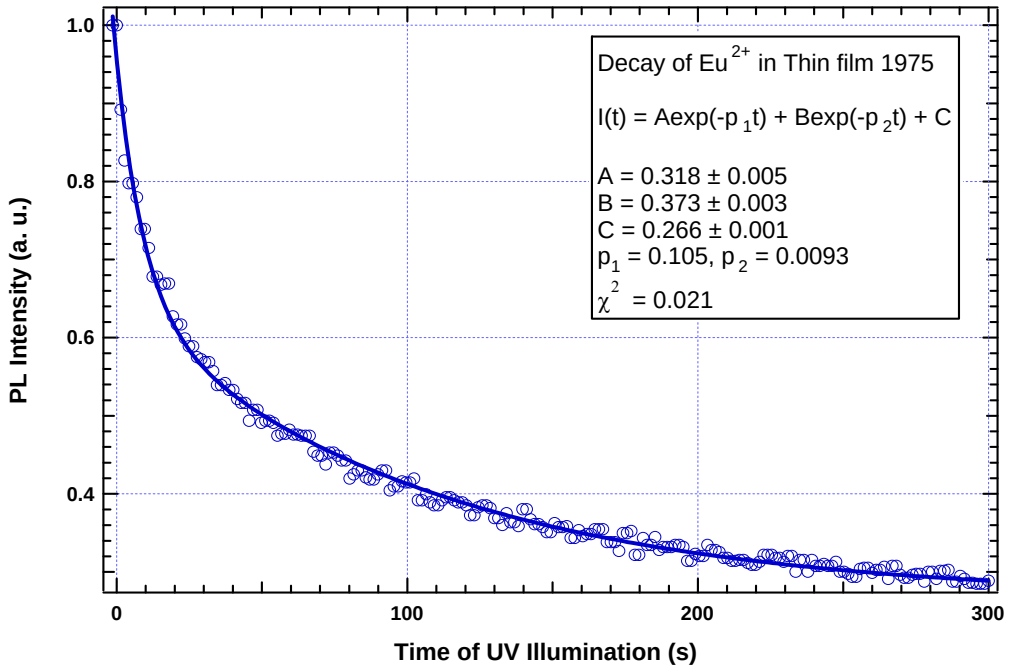

Fig. 4.12. Photobleaching of Eu^{2+} in a thin film (1975) of CaF_2. B-exponential fitting was used and shown with solid line. All the parameters and the coefficients are presented in the inset.

Table 4.4. Summary of fitting coefficients and parameters of Eu^{2+} photobleaching in thin film of CaF_2.

Coefficients		Parameters (s^{-1})	
A	0.318 ± 0.005	p_1	0.105
B	0.373 ± 0.003	p_2	0.0093
C	0.266 ± 0.001	$\chi^2 = 0.021$	

Having observed that the data suggest tunnelling contributes to Eu^{2+} bleaching in thin films, it remains to speculate on the origin of the layer involved. Fig. 4.13 shows schematic band diagram between CaF_2 and Si. Ionisation of the Eu^{2+} ions in the vicinity of the Si substrate might be assisted by tunnelling to the Si conduction band. The conduction band offset between CaF_2 and Si is ~2.3 eV [20] which allows the excited state of Eu^{2+} to be in resonance with the Si conduction band. Hence the probability of tunnelling still exists in thin films.

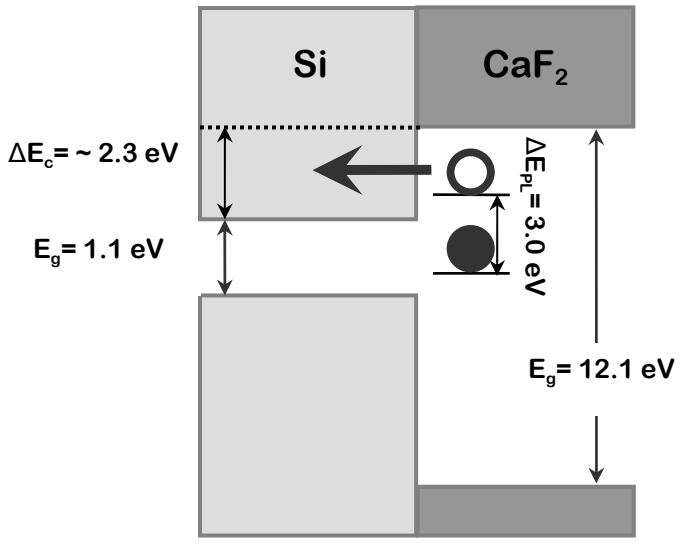

Fig. 4.13. Schematic of band structure of CaF_2 grown on a Si substrate. The values are obtained from ref. [20].

The Eu^{2+} fitting parameters here show that trapping is more probable than tunnelling in the thin film given both channels are considered. Unlike the SL and ISL, tunnelling is now made only one way, which is toward the Si substrate. Hence a smaller fraction of the Eu^{2+} ions are expected to be ionised by tunnelling.

In summary, photobleaching of Eu^{2+} from the *f-d* transition has been observed in a SL, an ISL and in a thin film due to ionisation of Eu^{2+} under UV (He-Cd laser) excitation. Two channels of ionisation are observed, namely, tunnelling and trapping. The tunnelling is migration of liberated electrons to the conduction band of CdF_2 and the trapping is the capture of liberated electrons by existing defect centres or impurities in CaF_2 layers. Bi-exponential fitting of the photobleaching decay curves suggested that tunnelling is a faster process than trapping. The tunnelling probability is significantly decreased by having undoped CaF_2 layers between Eu activators and CdF_2 layers judging from the ISL photobleaching result. This also supports the conclusion that tunnelling depends on the thickness of the CaF_2 layers as reported elsewhere. In addition to tunnelling to the CdF_2 conduction band, electrons can also migrate from a thin CaF_2 film to Si substrate with a similar mechanism. Also two different kinds of traps in the CaF_2 layers are suggested from the ISL photobleaching where the tunnelling probability is heavily reduced.

4.4 Transformation of Eu^{2+} to Eu^{3+}

Given that photobleaching occurred in SLs and thin films, it is very instructive to observe the presence of Eu^{3+} in the same host. The photobleaching is thought to be an oxidation of divalent Eu assisted by tunnelling and trapping of the liberated electrons. Hence creation of Eu^{3+} must accompany Eu^{2+} bleaching [24, 25]. This section examines Eu^{3+} as a photoproduct and correlates the observation of Eu^{3+} PL growth with the photobleaching of Eu^{2+}.

Following similar reasoning to equation (4.4), the normalised PL growth of Eu^{3+} can be written as an exponential form,

$$I(t) = I_0 + A\left(1 - e^{-p_1 t}\right) + B\left(1 - e^{-p_2 t}\right), \tag{4.5}$$

where I_0 (= 1) is the initial PL intensity of Eu^{3+} before the UV excitation. As shown in fig. 4.8, there is a population of already-existing cubic Eu^{3+} centres in the SL and suppose the population of the already-existing Eu^{3+} is comparable to that of Eu^{2+}. The coefficients A and B are the fractions of Eu^{2+} bleached by tunnelling and trapping, respectively as defined in section 4.3. Also the parameters p_1 and p_2 are the bleaching rates for tunnelling and trapping, respectively. It was proposed that the growth of Eu^{3+} is directly proportional to the decay of Eu^{2+}. A bi-exponential fitting was carried out using equation (4.5) with the coefficients and parameters obtained in section 4.3 (table 4.2) where bleaching of Eu^{2+} was considered. The resulting fit to the PL growth of Eu^{3+} in SL1647 is shown in fig. 4.14. In general, a reasonable fit was obtained with a χ^2 value of 0.647783. However the fitted line overshoots the data at longer time of UV exposure. It is worth repeating that the fit to the data in fig. 4.14 contains no free parameters.

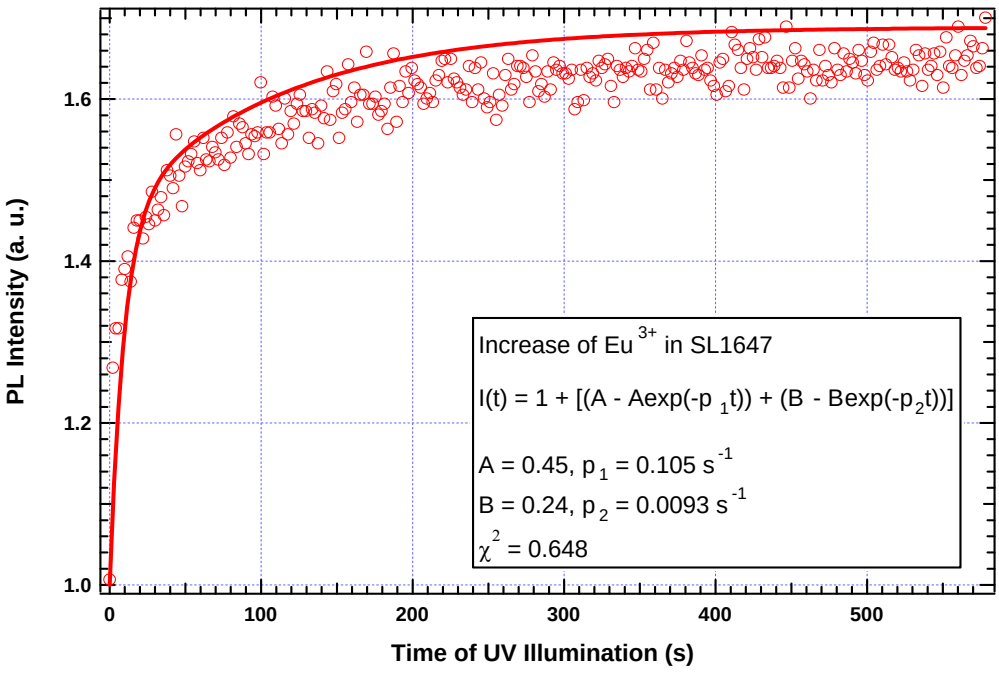

Fig. 4.14. Exponential growth of Eu^{3+} in $(CaF_2{:}Eu)_{20}$-$(CdF_2)_{20}$ SL's under UV laser excitation. Bi-exponential fitting was provided using equation (4.5). The fitting results are summarised in the inset.

In the process of PL growth, only the cubic Eu^{3+} centre was considered. This is because of the site-selective excitation provided by the dye laser. One might object that PL

intensity from non cubic centres such as trigonal (C_{3v}) or tetragonal (C_{4v}) centres might also grow as well as the cubic (O_h) grows. However at low temperature, upon the UV excitation, when cubic Eu^{2+} change its valency, it makes for F^- ions impossible to occupy interstitially to the nearest neighbour or next nearest neighbour* of Eu^{3+}. The objection can be ruled out by the fact that the mobility of F^- is too small for it to diffuse in the crystal in order to provide charge compensation at ~4 K. Also, during the epitaxial growth, Eu was doped in samples in divalent form. Charge compensation by F^- is not needed as Eu^{2+} substitutes for Ca^{2+} without changing its valency. As a consequence, any interstitial F^- ions are possibly remote from Eu^{2+} in samples and the number of the F^- charge compensators are initially minimised. Hence as Eu^{2+} converts to Eu^{3+} at low temperature any interstitial F^- remain remote from the Eu^{3+} cubic centre.

There is no doubt that some Eu ions were deposited in trivalent form during the growth at high temperature. In that case interstitial F^- can act as the charge compensator giving low symmetry Eu^{3+} centres during the growth. Non cubic centres were observed in combined excitation and emission spectroscopy as described in chapter 5. These non cubic centres are thought to be pre-existing charge compensated centres formed during the high temperature growth followed by annealing. Thus the PL intensity of the non cubic centres is not related to the photobleaching of the cubic Eu^{2+} centre provided by UV laser excitation. In fact, the tetragonal C_{4v} centre was monitored in the same way we monitored the cubic centre. Despite the low PL intensity, we did not observe any UV influenced PL growth or bleaching.

Judging from the fitting it is clear that not all the decrease of Eu^{2+} contributes to the formation of cubic centre Eu^{3+} because the data does not reach the model line. There are a couple of reasons to explain this discrepancy. Firstly, it is instructive to consider an effective role of electrons as charge compensation. Kingsley and Prener mentioned that an electron can act as a charge compensating agent in CdF_2 [26]. It is known that electrons in shallow traps or in the conduction band of CdF_2 are responsible for such charge compensation. This also might be the case for the liberated electrons in CaF_2-CdF_2 SLs. Hence an electron charge compensated Eu^{3+} centre can be produced upon Eu^{2+}

* The symmetry about the Eu^{3+} and F^- in the next nearest neighbour centre is trigonal C_{3v}. However this centre is not observed for Eu^{3+} in CaF_2 crystals. See chapter 5 for more explanation.

bleaching. Secondly the monitoring of the Eu^{3+} emission was only addressed to the $^5D_0 \rightarrow {}^7F_1$ transition. The selections rules discussed in chapter 2 allow the other transitions of Eu^{3+} cubic transitions as shown in fig. 4.8.

Hence equation (4.5) is modified below to account for the fact that not the entire Eu^{2+} cubic centre transforms to the specific transition of Eu^{3+} cubic centre. The modified PL growth of Eu^{3+} can be written as,

$$I(t) = I_0 + A_c\left(1 - e^{-p_1 t}\right) + B_c\left(1 - e^{-p_2 t}\right), \tag{4.6}$$

$$A_c = \frac{N_{tunnel}}{N} - A^*, B_c = \frac{N_{trap}}{N} - B^*.$$

The coefficients A_c and B_c are corrected portions of Eu^{2+} which contribute to the PL growth of cubic Eu^{3+} centre. The coefficient A, as defined earlier, is the portion of Eu^{2+} ionised by tunnelling and is calculated as 0.45198 in the previous section. The coefficient A^* is the fraction of those Eu^{2+} ions ionised by tunnelling that are contributing to other transitions and other centres of Eu^{3+}. This can be defined as $A^* = N_{Ctunnel}/N_{tunnel}$ where $N_{Ctunnel}$ represents the corrected number density of Eu^{2+} ions transformed to Eu^{3+} centres and emitted via other transitions than the $^5D_0 \rightarrow {}^7F_1$. The coefficient B is the portion of Eu^{2+} ionised via trapping and is calculated as 0.23685 in section 4.3. Similarly to A^*, B^* represents the fraction of ionised Eu^{2+} by trapping that does not contribute to the $^5D_0 \rightarrow {}^7F_1$ transition of the cubic centre and is defined as $B^* = N_{Ctrap}/N_{trap}$. Again bi-exponential growth is applied to the same SL (SL1647) using (4.6) and shown in fig. 4.15.

The value of χ^2 is significantly reduced to 0.158625 which indicates a better fit. The fitting results are summarised in table 4.5. Here the new coefficients A_c and B_c were reduced from A and B, respectively, indicating that some Eu^{2+} were contributing to the formation of other centres of Eu^{3+} which do not emit via the $^5D_0 \rightarrow {}^7F_1$ transition. The overall PL growth probability of the Eu^{3+} cubic centre due to the ionisation of Eu^{2+} can be represented by a simple tree diagram as shown in fig. 4.16. The probabilities are calculated using the coefficients obtained in bi-exponential fitting of Eu^{2+} photobleaching and Eu^{3+} PL growth.

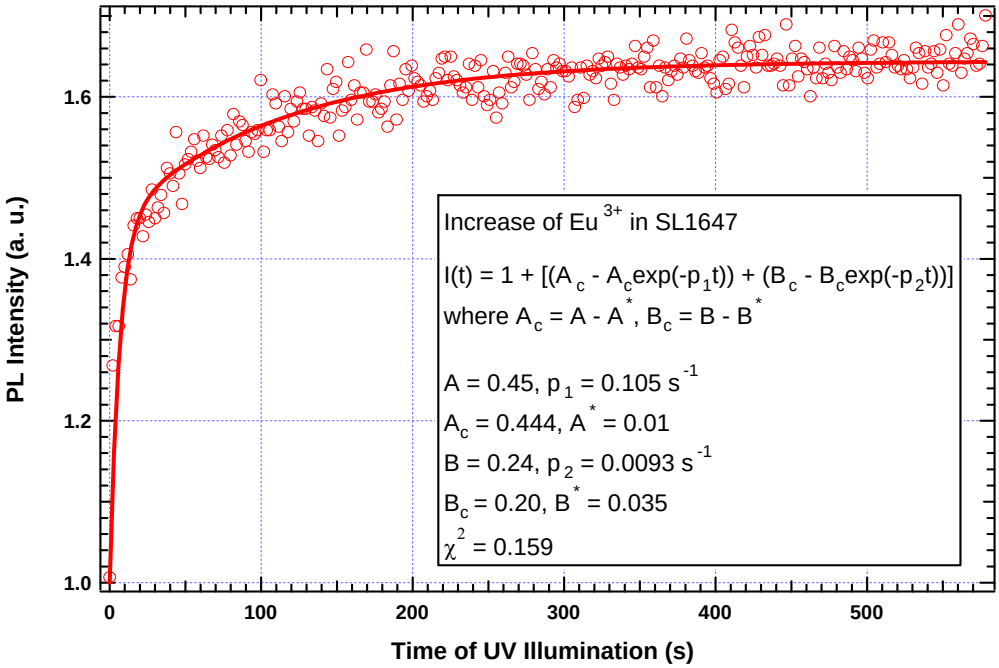

Fig. 4.15. Exponential growth of Eu^{3+} PL in a $(CaF_2{:}Eu)_{20}$-$(CdF_2)_{20}$ SLs under UV laser excitation. Bi-exponential fitting was provided using (4.6). The fitting results are summarised in the inset.

Table 4.5. Summary of fitting coefficients and parameters of Eu^{3+} PL growth in SL1647.

Coefficients		Parameters (s^{-1})	
A	0.45	p_1	0.105
A^*	0.01		
A_c	0.44	p_2	0.0093
B	0.24		
B^*	0.035	$\chi^2 = 0.159$	
B_c	0.20		

As a result, the probability of cubic Eu^{3+} PL growth fed by Eu^{2+} ionised via tunneling is 0.641 ± 6% and the probability of cubic Eu^{3+} PL growth fed by Eu^{2+} ionised via trapping is 0.294 ± 7%. For the given assumption the total probability for those ionised Eu ions contributing to the particular cubic transition ($^5D_0 \rightarrow {}^7F_1$) of Eu^{3+} is 0.94 ± 6%.

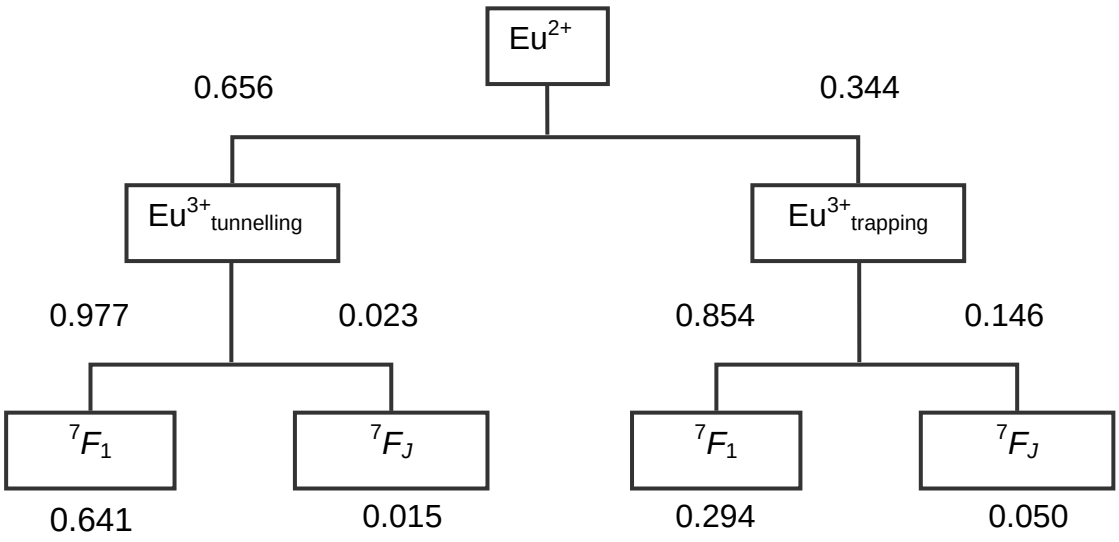

Fig. 4.16. Probability diagram for ionised Eu^{2+} ions contributing to the cubic centre of Eu^{3+}. The calculations were performed using the fitted coefficients obtained from SL1647.

Further investigation was carried out by cycling the UV laser on and off with a period of 300 s. A programmed shutter was used in the optical path. Fig. 4.17 shows corresponding results of Eu^{3+} and Eu^{2+} behaviour in SL1647 ($(CaF_2{:}Eu)_{20}$-$(CdF_2)_{20}$) over 3 cycles. Here the dye laser was continuously pumping Eu^{3+} at the cubic centre excitation wavelength even when the UV was blocked.

An almost step-like PL behaviour of Eu^{3+} was observed repeated over 3 cycles in contrast to the Eu^{2+} PL behaviour which exhibited continuous decay under the UV excitation. This puzzling observation is inconsistent with the earlier model in which PL growth of Eu^{3+} is directly fed by photobleaching of Eu^{2+} upon UV excitation. The PL growth model described in equations (4.5) and (4.6) only seems to be valid for the first cycle. In the second and the third cycles there are not enough Eu^{2+} ions to feed the Eu^{3+} PL growth.

The PL intensity of Eu^{3+} increases significantly when the UV is turned on and returns to its initial value when the UV is turned off regardless of the Eu^{2+} quenching. It is apparent that additional UV excitation influences Eu^{3+} PL behaviour regardless of the Eu^{2+} PL intensity.

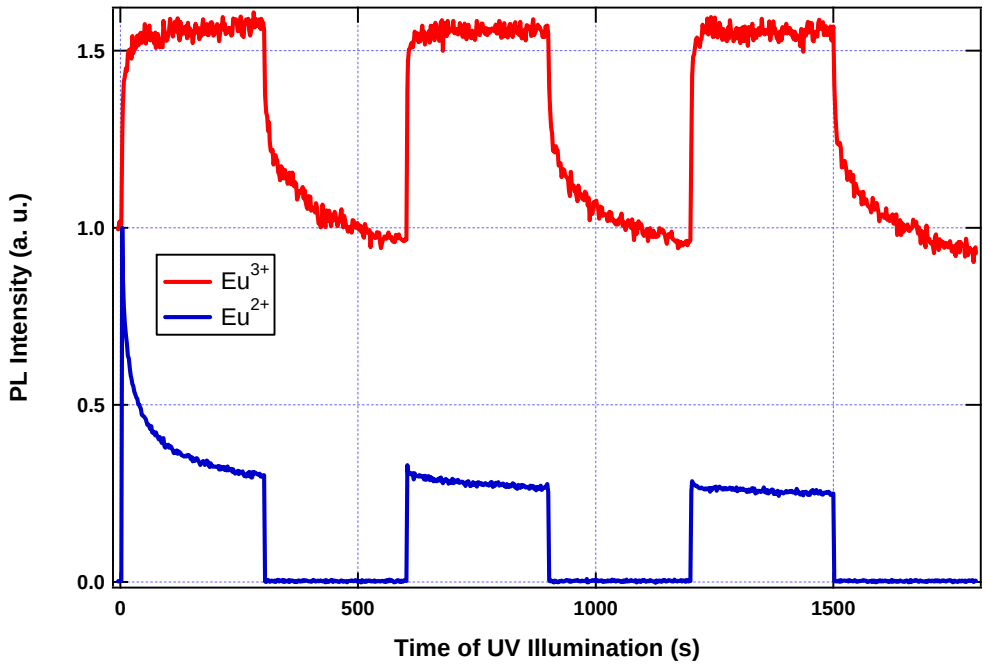

Fig. 4.17. Sequential PL intensity of Eu^{2+} and Eu^{3+} in $(CaF_2{:}Eu)_{20}$-$(CdF_2)_{20}$ SL (SL1647). The UV laser was on and off with a period of 300 s. The dye laser was operating continuously. PL intensity was monitored at the peak of broad emission (425.40 nm) and Eu^{3+} was monitored at 590.20 nm, the $^5D_0 \rightarrow {}^7F_1$ transition of the cubic centre.

Another evidence which shows the irrelevance of the $Eu^{2+} \rightarrow Eu^{3+}$ transformation can be found in thin film of CaF_2:Eu. In fig. 4.18, the usual PL bleaching of the Eu^{2+} is observed while no dramatic change in PL intensity for Eu^{3+} in observed. There was about 10% decrease in the PL intensity of Eu^{3+} at the end of the second complete cycle however this is possibly due to drift of the dye laser. Again, it is hard to relate PL growth of Eu^{3+} and the photobleaching of Eu^{2+} in the thin film. The PL growth of Eu^{3+} is only observed from SLs and ISLs in this study. Hence the PL growth of Eu^{3+} is thought to be a peculiar phenomenon only observed in SLs (and ISLs) and does not prove itself as a photoproduct of the Eu^{2+} bleaching.

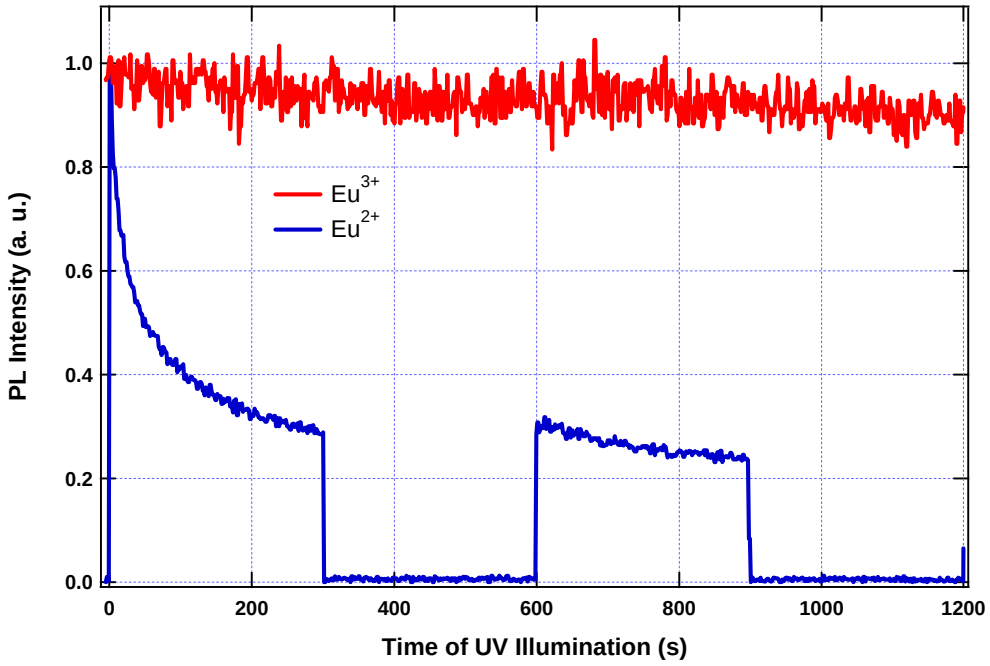

Fig. 4.18. Photobleaching of Eu^{2+} and PL of Eu^{3+} in a thin film of CaF_2:Eu (TF1975). The UV laser was on and off with a period of 300 s.

In summary Eu^{2+} photobleaching is observed in SLs, ISLs and thin films of CaF_2:Eu. Two channels of photobleaching are considered, namely tunnelling and trapping. For SLs and ISLs the tunnelling is the migration of electrons, liberated in the *f-d* transition excited by the UV laser, to the conduction band of neighbouring CdF_2 layers. For thin films, in the process of tunnelling, the electron migration is proposed to be to the conduction band of the Si substrate. Trapping is associated with impurities or defects within the CaF_2 layers. Bi-exponential fitting suggested that tunnelling is a faster process than trapping.

Eu^{3+} is initially considered as a product of the photobleaching of Eu^{2+} in SLs, ISLs and thin films. The initial PL growth of Eu^{3+} agreed well with the bi-exponential growth governed by the parameters and coefficients from the Eu^{2+} photobleaching problem. However the assumption that Eu^{2+} oxidises to Eu^{3+} does not hold when the UV excitation is repeated more than one cycle. There is insufficient experimental evidence that the photobleaching of Eu^{2+} directly increases the PL growth of Eu^{3+}. The PL intensity of Eu^{3+} itself in SLs was effectively influenced by the additional UV excitation. Hence it was concluded that the PL intensity behaviour of Eu^{3+} is independent of Eu^{2+} bleaching. Even though the PL behaviours of both Eu^{2+} and Eu^{3+} appear independent of each other, the

origin of the PL behaviours is possibly the same, i.e. transfer of electrons. The PL behaviour of Eu^{3+} is discussed further in the following chapter.

4.5 Recovery of Eu^{2+} by thermal excitation

In MF_2 (M = Alkali-earth metals) crystals doubly doped with rare earth ions, recovery of photobleaching is quite possible. For example Feofilov [15] has optically confirmed photobleaching and recovery of Eu^{2+} and Sm^{3+} doped in BaF_2. The photobleaching was done by exposing the crystal to a mercury lamp for 5 – 10 mins and the recovery of the ions was done by heating the crystal thereafter. Such observation can be written as,

$$Eu^{2+} + Sm^{3+} \underset{k_B T}{\overset{h\upsilon}{\longleftrightarrow}} Eu^{3+} + Sm^{2+}.$$

It is thought that the bleaching is by phototransfer of an electron from Eu^{2+} followed by a capture of the electron by Sm^{3+} [27]. The observation is that the photobleaching is completely reversible. For the thermal recovery of Eu^{2+}, Welber has shown that the reversible phototransfer is also possible in doubly doped CaF_2 using different frequency of light [16]. The phototransfer can be written as,

$$Eu^{2+} + Sm^{3+} \underset{h\upsilon'}{\overset{h\upsilon}{\longleftrightarrow}} Eu^{3+} + Sm^{2+},$$

where $\upsilon \neq \upsilon'$. Overall the recovery of Eu^{2+} is possible by means of optical and thermal excitation.

The recovery of Eu^{2+} photobleaching of interest in this section requires a different mechanism than the recovery reported by Feofilov [15] and Welber [16] as there is no second ion present in the SLs. In the absence of the second ion (usually a trivalent lanthanoid in cubic symmetry) one might suggest that Eu^{3+} participates in the phototransfer. In fact, electron capturing by the cubic centre of trivalent lanthanoids is expected to be far more probable than charge compensated trivalent lanthanoids [16, 17,

27]. If this is the case the PL intensity of Eu^{3+} of the cubic centre would be expected to decrease as Eu^{2+} bleaches. In section 4.4, it was shown that the PL intensity of the cubic Eu^{3+} centre increased at a similar rate to the Eu^{2+} decrease. Hence it is hard to believe that Eu^{3+} in a cubic centre captures those electrons from Eu^{2+} in the case of SLs. Furthermore it was concluded that the PL behaviour of Eu^{3+} in a cubic centre (fig. 4.17) under influence of UV laser was almost independent of the Eu^{2+} PL behaviour. This strongly disproves the assumption of Eu^{3+} being a capturing trap for an electron released from Eu^{2+}. PL behaviour of Eu^{3+} in a thin film (presented in fig. 4.18) suggests that Eu^{3+} is not related to the process of Eu^{2+} ionisation. Also the PL behaviour of Eu^{3+} in a SL (as shown in fig. 4.17) suggests that the PL behaviour is independent of the PL bleaching of Eu^{2+}. Hence the photobleaching of Eu^{2+} and the possible recovery of it should be explained without employing the cubic centre of Eu^{3+}.

These observations are somewhat similar to the photobleaching of Sm^{2+} in alkaline earth fluorohalides reported by Jang *et al*. [28]. They observed photobleaching of Sm^{2+} which can be best described as bi-exponential with respect to time while observing no increase of Sm^{3+} at the same time. They proposed the mechanism of photobleaching as,

$$Sm^{2+} + (trap) \xrightarrow{h\upsilon} [Sm^{3+}(trap)^{-}],$$

or

$$Sm^{2+} + (trap) \xrightarrow{h\upsilon} [Sm^{2+*}(trap)].$$

Either an electron released from Sm^{2+} is captured by a trap which binds to Sm^{3+} or excited Sm^{2+*} emission is quenched by a defect centre and loses its ability to luminescent [28]. In either case no Sm^{3+} emission is expected.

We propose a similar mechanism to describe the Eu^{2+} bleaching in connection with the presence of a trap. The modified PL bleaching of Eu^{2+} from (4.3.) can be written as,

$$Eu^{2+} + trap, CB \xleftrightarrow[k_B t]{h\upsilon} [Eu^{3+} \cdot trap^{-}] + [Eu^{3+} \cdot e^{-}], \qquad (4.7)$$

where *CB* is conduction band of CdF_2. Here $Eu^{3+}{\cdot}trap^-$ and $Eu^{3+}{\cdot}e^-$ are the complex centres of Eu^{3+} and an electron captured adjacent to Eu^{3+}. Here we propose that an electron released from a Eu^{2+} (thus converting Eu^{2+} to Eu^{3+}) is localised in close proximity under UV excitation. Prior to the formation of the complex centre, transfer of electrons take place in CaF_2 (trapping) and captured by a trap. Also at the same time transfer of electron takes place through the conduction band of CdF_2 (tunnelling) followed by localisation at the bottom of the conduction band as described in the previous sections. The nature of the complex centres can either be a quenching or luminescence centre. We have no knowledge of the nature of these complex centres in terms of optical transitions. Under the influence of the UV laser, however, we did not observe a creation and therefore enhancement of a Eu^{3+} centre other than already presented in SLs in monitoring optical transition wavelengths near the Eu^{3+} cubic centre. We further propose that electrons in the $Eu^{3+}{\cdot}trap^-$ and in the $Eu^{3+}{\cdot}e^-$ complex centres can be dissociated thermally. At elevated temperatures the electrons are expected to be released from the centres and recombine with Eu^{3+} giving Eu^{2+}. Hence, depending on temperature, the above equation can be reversed by heating the host SLs.

As a result, Eu^{2+} PL was restored by heating the SL (SL1647) to a temperature above 160 K. Even by heating the SL to 20 K and cooling it back to 4 K, some recovery of the Eu^{2+} PL was observed. The results are shown in fig. 4.19. The blue line in the figure represents the PL bleaching of Eu^{2+} in another excitation spot at 4 K as a reference. It is evident that PL bleaching is persistent at low temperature. However when the SL is heated up to a higher temperature and cooled back to 4 K a temperature dependent recovery is observed (red line in fig. 4.19).

A further analysis was carried out by plotting the PL growth against raised temperature as shown in fig. 4.20. Using a single exponential growth, the PL behaviour with respect to temperature, *T*, can be expressed as,

$$PL(T) = N \exp\left(\frac{-E}{k_B T}\right), \tag{4.8}$$

where N is proportionality constant expressed in arbitrary unit and k_B is Boltzmann's constant 8.167 X 10^{-5} eV/K. Here E is the energy barrier for the localised electron in the $Eu^{3+}\cdot trap^{-}$ and the $Eu^{3+}\cdot e^{-}$ complex centres. The above expression gave a good agreement with the experimental data. The calculated value of the energy, E is 50 ± 10 meV. This is equivalent to the recombination energy which allows for electrons to release from the $Eu^{3+}\cdot trap^{-}$ and the $Eu^{3+}\cdot e^{-}$ complexes and to produce Eu^{2+}. At high temperature, however all the complexes are expected to yield Eu^{2+}.

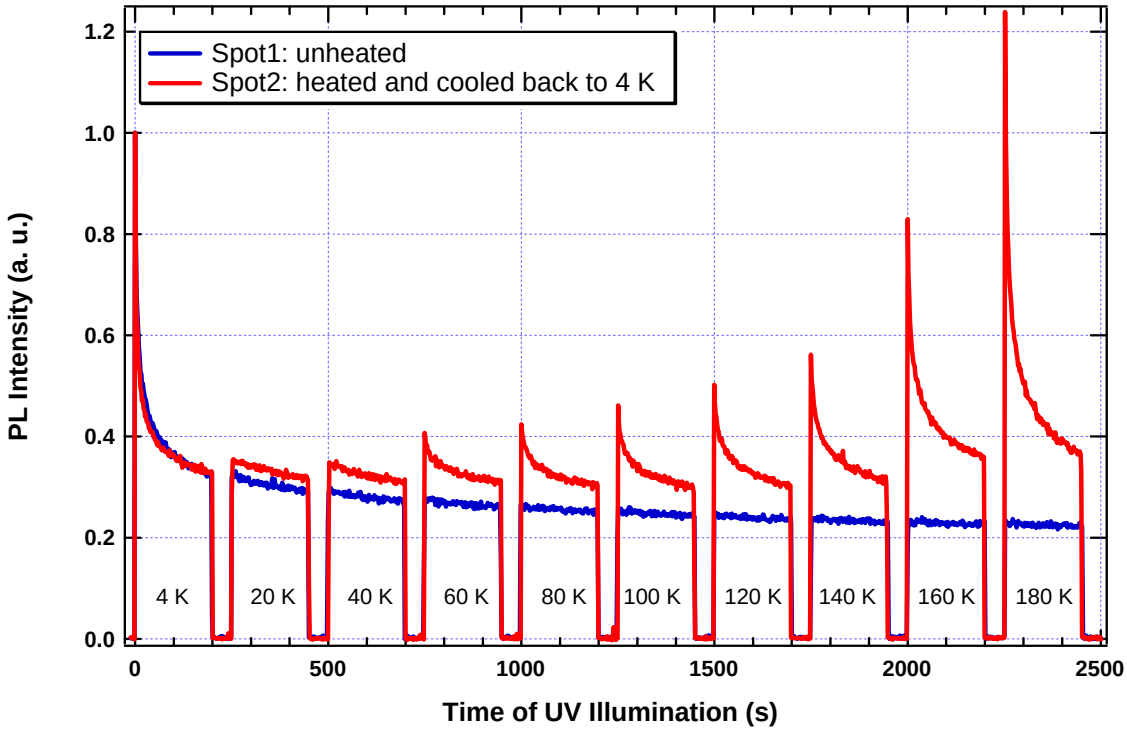

Fig. 4.19. Photobleaching of Eu^{2+} in $(CaF_2{:}Eu)_{20ML}$-$(CdF_2)_{20ML}$ SL (SL1647). The red curve shows PL bleaching of Eu^{2+} after heating to a series of higher temperatures and then cooling back to 4 K. The blue curve is shown as reference PL kept at 4 K at all times.

The exponential fitting was improved by establishing additional potential energy barrier of the liberated electrons as shown in fig 4.21. Now (4.8) is modified as shown below, including the two energy barriers due to the possible nature of the PL bleaching,

$$PL(T) = N_1 \exp\left(\frac{-E_1}{k_B T}\right) + N_2 \exp\left(\frac{-E_2}{k_B T}\right). \qquad (4.9)$$

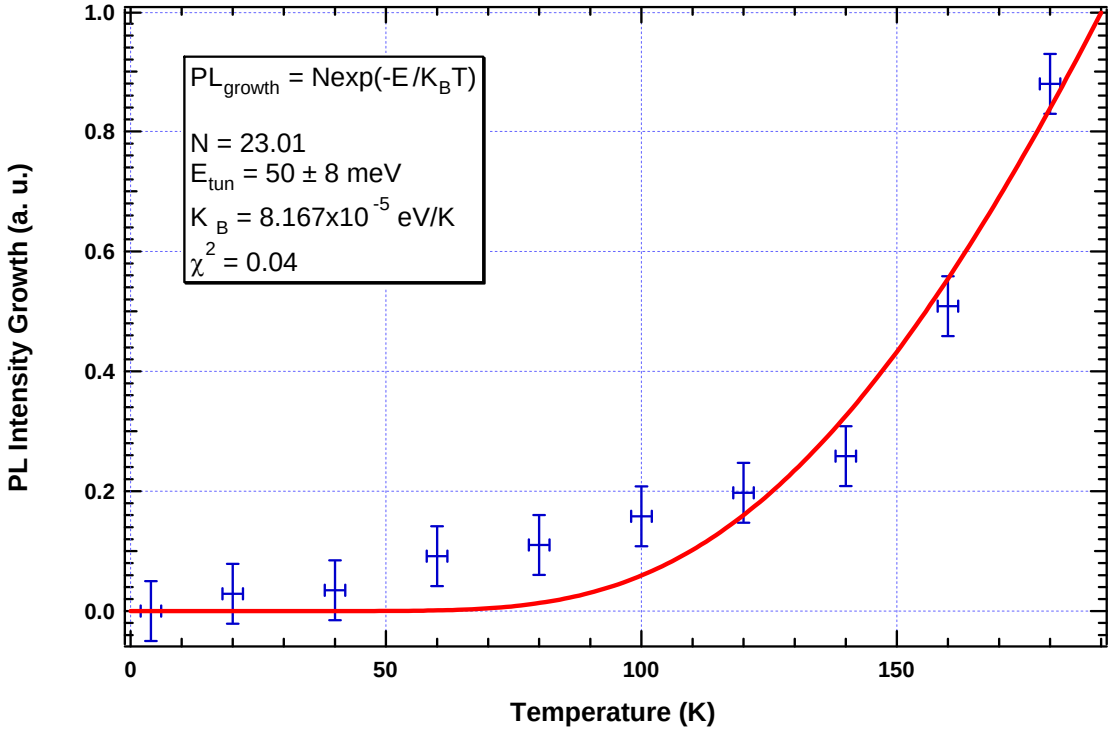

Fig. 4.20. Exponential fitting of PL growth of Eu^{2+} with temperature (SL1647).

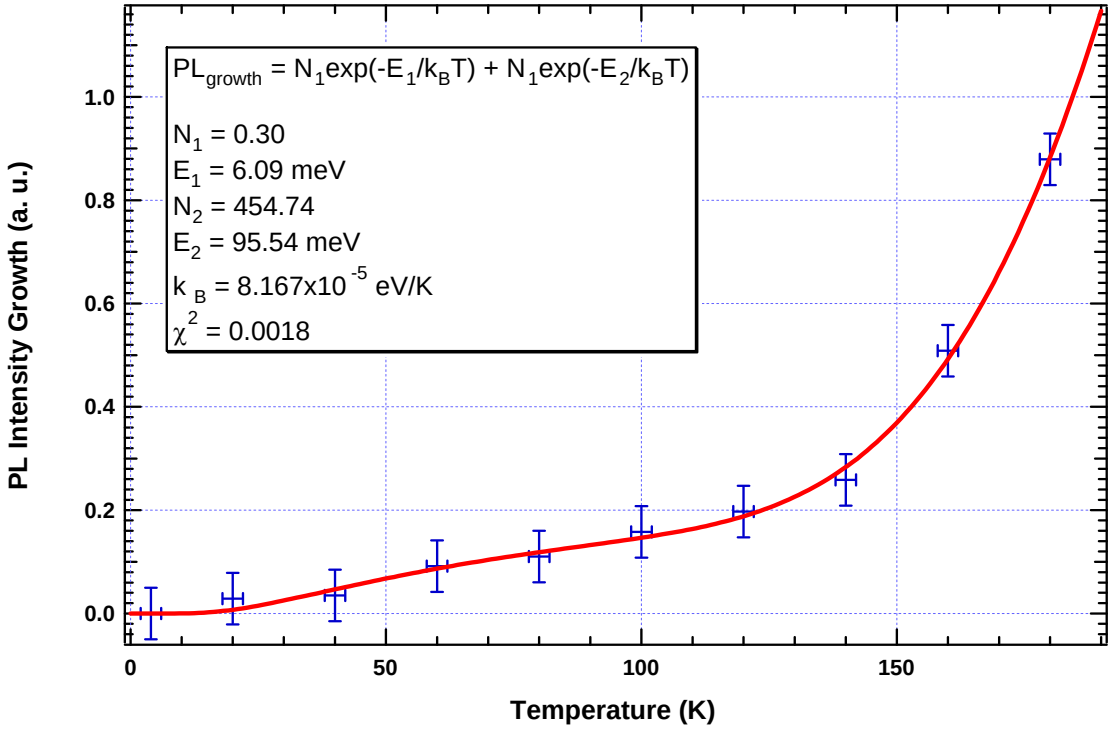

Fig. 4.21. Exponential fitting of PL growth of Eu^{2+} (SL 1647) with temperature using two energy potentials.

All the parameters and constants in (4.9) are already defined in (4.8). A better thermal recovery fitting for Eu^{2+} was obtained using (4.9). The energy barriers using (4.9) are estimated to be 6.09 meV and 95.54 meV. As it stands the values obtained from the fitting does not distinguish between the $Eu^{3+}{\cdot}trap^{-}$ and the $Eu^{3+}{\cdot}e^{-}$ complexes. However it should be noted that thermal recovery of Eu^{2+} is originated from two different agents.

The whole process of the PL bleaching and the thermal recovery of the Eu^{2+} can be summarised as follows; the UV laser generated the photoionisation of the Eu^{2+} in SLs followed by transfer of the electrons by means of tunneling and trapping. The electrons are then localized, either in conduction band of CdF_2[*] layers or in CaF_2, in the vicinity of Eu^{3+} and form complex centres. At low temperature, at the complex, the electron and the Eu^{3+} are separated by a potential barrier. When the SL is heated at sufficient temperature, the electron and the Eu^{3+} recombine to produce Eu^{2+}.

In summary, PL recovery of Eu^{2+} was optically confirmed by heating the SL up to ~180 K and cooling it back to 4 K. The $Eu^{3+}{\cdot}trap^{-}$ and the $Eu^{3+}{\cdot}e^{-}$ complex centres were proposed as a metastable agent for electron capture from Eu^{2+}. In these heterostructures it is assumed that electrons can be localised in both CaF_2 and CdF_2 layers in the vicinity of Eu^{3+}. The detailed nature of the complex is yet to be investigated. The potential barriers separating the localised electron and the Eu^{3+} are calculated to be 6.09 meV and 95.56 meV. One of which is the energy barrier for the $Eu^{3+}{\cdot}trap^{-}$ and the other energy is for the $Eu^{3+}{\cdot}e^{-}$ complex. However detailed assignment of the energy barriers is needed in future study.

[*] The localisation of electrons in the conduction band is understood as a localisation of electrons at the bottom of the conduction band where the band bending occurs.

References

[1] J. F. Owen, P. B. Dorain, T. Kobayashi, "Excited-state absorption in Eu^{2+}:CaF_2 and Ce^{3+}:TAG single crystals at 298 and 77 K," *J. Appl. Phys.*, vol. 52, pp. 1216-1223, 1981.

[2] N. W. Ashcroft, N. D. Mermin, *Solid State Physics*: Saunders College Publishing, 1976.

[3] L. L. Chase, "Microwave-optical double resonance of the metastable $4f^6 5d$ level of Eu^{2+} in the fluorite lattices," *Phys. Rev. B*, vol. 2, pp. 2308-2318, 1970.

[4] A. Winnacker, R. M. Shellby, R. M. Macfarlane, "Photon-gated hole burning: a new mechanism using two-step photoionasation," *Opt, Lett.*, vol. 10, pp. 350-352, 1985.

[5] A. A. Kaplyanskii, A. K. Przhevuskii, "Deformation splitting and enhancement of spectral lines and the structure of excited levels of Eu^{2+} in Alkali-earth Fluoride crystals," *Opt. Spectry.*, vol. 19, pp. 331-338, 1964.

[6] N. S. Sokolov, N. L. Yakovlev, "Luminescence of Rare-Earth Ions in Epitaxial Fluoride Layers," *Proc. SPIE*, vol. 2706, pp. 57-66, 1996.

[7] S. V. Gastev, N. V. Novikov, N. S. Sokolov, N. L. Yakovlev, "Molecular-beam epitaxy of CaF_2 layers on Si(111); determination of the deformation of these layers from the extrinsic photoluminescence spectrum," *Sov. Tech. Phys. Lett.*, vol. 13, pp. 401-402, 1987.

[8] X. M. Fang, T. Chatterjee, P. J. McCann, W. K. Liu, M. B. Santos, W. Shan, J. J. Song, "Molecular beam epitaxy growth of Eu-doped CaF_2 and BaF_2 on Si," *J. Vac. Sci. Technol. B*, vol. 14, pp. 2267-2270, 1996.

[9] G. Burns, *Solid State Physics*: Academic Press, 1990.

[10] N. S. Sokolov, S. V. Gastev, S. V. Novikov, N. L. Yakovlev, A. Izumi, S. Furukawa, "Molecular beam epitaxy of CdF_2 layers on CaF_2(111) and Si(111)," *Appl. Phys. Lett.*, vol. 64, pp. 2964-2966, 1994.

[11] R. M. Tromp, M. C. Reuter, "Structure of the Si(111)-CdF_2 Interface," *Phys. Rev. Lett.*, vol. 61, pp. 1756-1759, 1988.

[12] E. Loh, "Ultraviolet-absorption spectra of Europium and Ytterbium in alkaine earth fluorides," *Phys. Rev.*, vol. 184, pp. 348-352, 1969.

[13] D. M. Boye, Y. Sun, R. S. Meltzer, N. S. Sokolov, J. C. Alvarez, "Population hole burnung on the $4f^7(^8S_{7/2})$-$4f^6$5d zero-phonon transition in MBE films of CaF_2:Eu^{2+}," *J. Lum.*, vol. 66&67, pp. 29-35, 1996.

[14] S. V. Gastev, J. C. Alvarez, V. V. Vitvinski, N. S. Sokolov, A. Y. Khilko, "Bleaching Effects in Photoluminescence of Rare Earth ions in fluoride heterostructures," *Proc. SPIE*, vol. 2706, pp. 67, 1996.

[15] P. P. Feofilov, "Phototransfer of an Electron in MeF_2-Eu, Sm Monocrystals," *Optics and Spectroscopy*, vol. 12, pp. 531-533, 1962.

[16] B. Welber, "Reversible Phototransfer of Electrons between Rare-Earth Ions in CaF_2," *J. Chem. Phys.*, vol. 15, pp. 4262-4264, 1965.

[17] B. Welber, "Direct Charge Transfer by X Irradiation in the System CaF_2:Eu, Tm," *J. Appl. Phys.*, vol. 9, pp. 2744-2745, 1965.

[18] R. M. Macfarlane, R. M. Shellby, "Photoionization hole burning and nonlinear Zeeman effect in CaF_2:Sm^{2+}," *Opt, Lett.*, vol. 12, pp. 533-535, 1984.

[19] N. S. Sokolov, S. V. Gastev, A. Y. Khilko, S. M. Suturin, I. N. Yassievich, J. M. Langer, A. Kozanecki, "Tunneling-assisted autoionization of the localized impurities in nanostructures," *Phys. Rev. B*, vol. 59, pp. R2525-R2528, 1999.

[20] A. Izumi, Y. Hirai, K. Tsutsui, N. S. Sokolov, "Study of band offsets in CdF_2/CaF_2/Si(111) heterostructures using x-ray photoelectric spectroscopy," *Appl. Phys. Lett.*, vol. 67, pp. 2792-2794, 1995.

[21] C. Pedrini, D. S. McClure, C. H. Anderson, "Photoionization thresholds of dicalent rare earth ions in alkaline earth fluorides," *J. Chem. Phys.*, vol. 70, pp. 4959-4962, 1979.

[22] C. Pedrini, F. Rogemond, D. S. McClure, "Photoionisation thresholds of rare-earth impurity ions. Eu^{2+}:CaF_2, Ce^{3+}:YAG and Sm^{2+}:CaF_2," *J. Appl. Phys.*, vol. 59, pp. 1196-1201, 1986.

[23] S. M. Suturin, S. A. Basun, S. V. Gastev, J. M. Langer, R. S. Meltzer, N. S. Sokolov, "Optical detection of electron transfer through interfaces in CaF_2:Eu-CdF_2 SLs," *Appl. Surf. Sci.*, vol. 162-163, pp. 474-478, 2000.

[24] R. J. Reeves, J. K. Choi, S. V. Gastev, A. V. Krupin, K. R. Hoffman, N. S. Sokolov, "Laser spectroscopy of Eu^{3+} centers in CaF_2:Eu–CdF_2 superlattices," *J. All. Com.*, vol. 451, pp. 84-87, 2008.

[25] V. A. Chernyshev, A. V. Abrosimov, S. V. Gastev, A. V. Krupin, A. E. Nikiforov, J. K. Choi, R. J. Reeves, S. M. Suturin, N. S. Sokolov, "Energy structure of Eu^{3+} centres in CdF_2–CaF_2:Eu superlattices on silicon," *J. Phys.: Condens. Matter*, vol. 19, pp. 395023, 2007.

[26] J. D. Kingsley, J. S. Prener, "Free Charge Carrier Effect in Cadmium Fluoride," *Phys. Rev. Lett.*, vol. 8, pp. 315-316, 1962.

[27] W. Mou, D. S. McClure, "Photoionization and trapping of electrons in the system BaF_2:Eu:Sm," *Phys. Rev. B*, vol. 47, pp. 11031-11038, 1993.

[28] W. Qin, K. Jang, S. Park, Y. Lee, C. Kim, "The mechanism of photobleaching in Sm^{2+}-doped alkaline-earth fluorohalides," *J. Lum.*, vol. 113, pp. 9-16, 2005.

Chapter 5

Spectroscopy of trivalent Eu centres in symmetric CaF_2:Eu-CdF_2 superlattices

5.1 Introduction

This chapter concerns Eu^{3+} as defect centres in symmetric CaF_2:Eu-CdF_2 SLs. The definition of symmetric SLs in this study is that the thickness of CaF_2 and CdF_2 are identical within the technology uncertainty. For example a 20 ML thick SL consists of 20 ML thick CaF_2 layers and subsequent equally thick CdF_2 layers deposited repeatedly throughout the whole SL. In the previous chapter it was mentioned that Eu^{3+} can either be pre-existing or produced from the photobleaching of the parent Eu^{2+} in CaF_2:Eu host. Regardless of the origin of the Eu^{3+} it is very important to undertake laser spectroscopy of the Eu^{3+} centres as they have not previously been studied in such nano crystalline structures to be the best of our knowledge. Hence this chapter seeks to investigate fundamental similarities and differences in the spectroscopy of the Eu^{3+} centres in bulk and in nano crystals. In addition some physical models are proposed here to assist fuller understanding of the PL behaviour of Eu^{3+} centres in SLs.

Previous spectroscopic investigations of CaF_2 crystals doped with trivalent Eu^{3+} have been extensively carried out by many researchers and hence provide essential information to the current study. Especially with the advent of laser spectroscopic techniques Hamers *et al*. [1] were able to distinguish five major centres of Eu^{3+} in a CaF_2:Eu (0.1%) crystal and established energy levels, lifetimes and branching ratios for the Eu^{3+} centres. The major centres are designated as A, O, P, Q and R in which the A is tetragonal, the O is

cubic, the P is unassigned and the Q and the R are cluster centres, respectively. Jouart *et al*. [2] investigated the cubic (O) centre extensively in various hosts (CdF_2, CaF_2, SrF_2 PbF_2 and BaF_2) and provided fuller energy level configurations in the cubic centre. They also have shown that the crystal field strength depends upon the interionic distance between Eu^{3+} and various hosts. Also Eu^{3+} centres were used to study kinetics of the F^- anion which is responsible for local symmetries and distributions of charge compensated Eu^{3+} centres [3, 4].

Combined excitation emission spectroscopy (CEES) was employed in this study of SLs and thin films. Two major centres, the A and the O, and some minor centres are observed, with O the strongest. In addition to the well known centres a novel centre of Eu^{3+} in thin SLs is also revealed in high resolution CEES. This centre is designated as the I centre and has shown interesting PL behaviour upon thermal excitation, thickness of the host and additional UV excitation. In a 2 ML thick $(CaF_2:Eu)_2$-$(CdF_2)_2$ SL, for example, the cubic centre is almost absent and the I centre was solely observed, whereas the O centre is dominant, having the I centre as a weak shoulder, in thick SLs. Based on these observations various models are considered to elucidate the nature of the I centre in this chapter.

Section 5.2 discusses some physical models based on previous observations [5] of Eu^{3+} centres in CaF_2:Eu-CdF_2 and their anomalous temperature and thickness dependent PL behaviour. That section also discusses the influence of additional UV excitation on the PL behaviour of Eu^{3+} in SLs observed in the current study using an appropriate model. In section 5.3, crystal field calculations are carried out using an ‘f-shell’ program for the strongest O centre.

5.1.1 Previous work

Prior to this study, a collaborative investigation involving preliminary laser spectroscopy of Eu^{3+} centres in CaF_2:Eu-CdF_2 SLs was undertaken and reported in the Masters thesis of the author [5]. It is necessary to report the previous observations here so that some physical models proposed in the current study can be tested to assist in a fuller

understanding of the physical properties of CaF_2-CdF_2 SLs. The most significant observation from the previous work was the realisation of the novel I centre of Eu^{3+} in CaF_2:Eu-CdF_2 as shown in fig. 5.1. It only appeared in thin SLs using high resolution CEES. Its transition wavelengths are very close to that of the cubic centre. For the $^7F_0 \rightarrow {}^5D_1$ excitation of Eu^{3+}, for example, the transition wavelength difference between those two centres is 0.05 ± 0.02 nm (1.8 cm^{-1}). Similarly in the $^5D_0 \rightarrow {}^7F_1$ emission, the I centre shows a blue shift of 0.22 ± 0.02 nm (6 cm^{-1}).

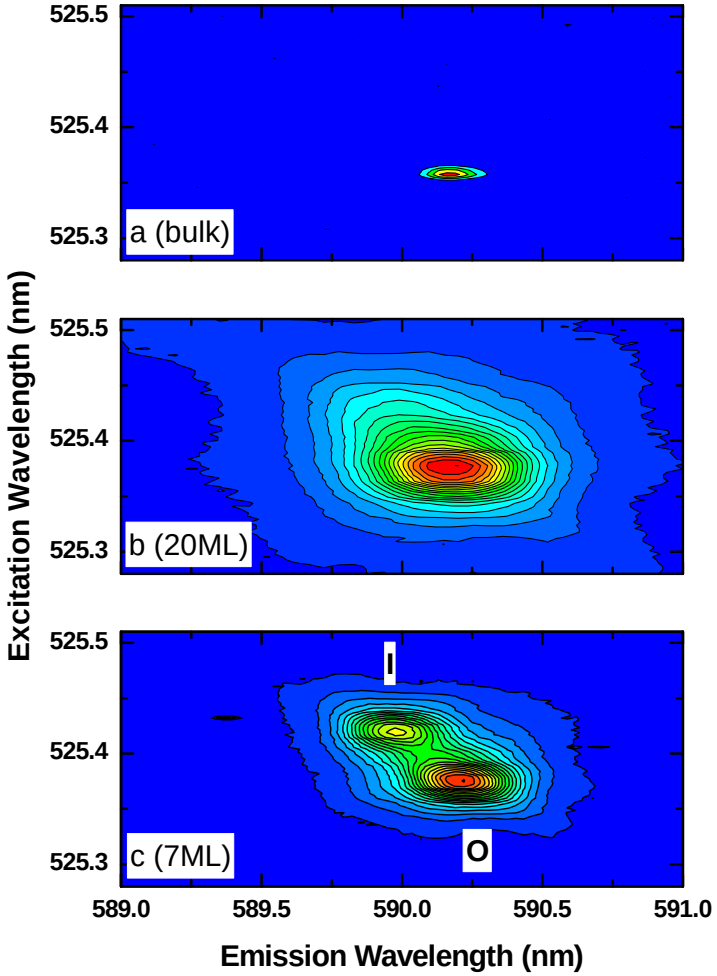

Fig. 5.1. Contour plots of the Eu^{3+} cubic (O) centre in (a) bulk crystal, (b) 20ML thick SL and (c) 7ML thick SL. The I centre can be seen in (c) and also in (b) as a weak shoulder near the cubic centre. All spectra were recorded at ~ 4K.

Despite the closeness of the I centre to the cubic centre in transition energies, it was concluded that the I centre has an axial symmetry. The basis for that conclusion was the

observation of splittings, appearing as weak shoulders, in both excitation and emission wavelengths particularly in $^7F_0 \rightarrow {}^5D_1$ and $^5D_0 \rightarrow {}^7F_1$ transitions. However those transitions for a cubic centre are not split indicating that the symmetries of Eu^{3+} in the cubic and the I centre are fundamentally different. The splittings are indicated as arrows in fig. 5.2.

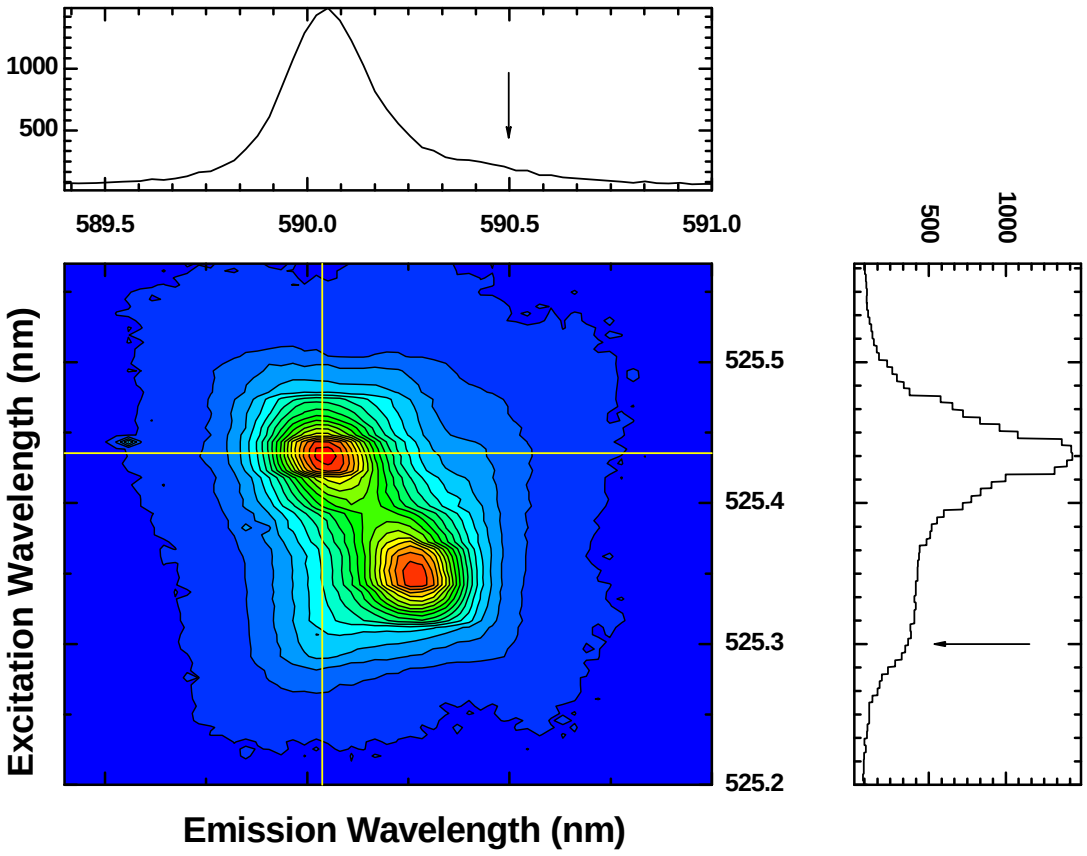

Fig. 5.2. Contour plot of the I and the O centres in a 3 ML thick SL. Each grid line represents emission spectrum (top graph) and excitation spectrum (right graph) of the I centre. The splittings of the I centre in the emission and the excitation are indicated by arrows.

It was proposed that the symmetry of Eu^{3+} defects deposited at the interface of CaF_2-CdF_2 is influenced by the local environment for two reasons and hence the name I ('interface') centre. Firstly, at the interface, Eu^{3+} sees more Cd^{2+} ions than those in deeper layers in CaF_2. Secondly, electrons in the conduction band of CdF_2 are responsible for producing such an axial field. PL behaviour of the I centre was somewhat thickness dependent. From a 20 ML thick SL to a 2 ML thick SL, the PL intensity of the I centre increased monotonically relative to the PL intensity of the cubic centre. No thickness dependent

shift in the transition wavelengths was observed which suggests that the PL intensities of the Eu^{3+} centres are rather quantised upon the thickness of SLs.

In temperature dependent PL, the I centre quenched lower temperature than the O centre at ~140 K. It was concluded that the electrons in the conduction band are delocalised due to thermal excitation and the electric field produced between the interface Eu^{3+} and the electrons are diminished at high temperatures.

5.2 Discussions of CEES results for Eu^{3+} centres in symmetric superlattices

Various aspects of CEES for Eu^{3+} centres, especially the I and the O centres, in symmetric SLs are discussed in this section. The following subsection discusses further investigation on the symmetry of the I centre by using polarised excitation and emission technique. Where the splitting in transition wavelengths became more apparent. As opposed to the earlier report [5], a more suitable symmetry assignment than 'axial' to the I centre is discussed. Based on the previous thickness and temperature dependent PL behaviour, corresponding models are proposed and fitted to the experimental results. Also observation of interesting PL behaviour provided by additional UV excitation to SLs is discussed with an appropriate model.

5.2.1 Symmetry assignments of Eu^{3+} centres in symmetric CaF_2:Eu-CdF_2 Superlattices

Symmetry assignment of Eu^{3+} centres in CaF_2:Eu-CdF_2 SLs is relatively easy apart from the I centre. The assignments were assisted by comparing to the centres already observed by Hamers *et al*. [1]. As shown in fig. 5.3 a CaF_2:Eu-CdF_2 SL and a CaF_2:Eu bulk crystal were investigated under the same excitation and emission wavelengths. Two centres of Eu^{3+} in a SL were chosen in order to compare with the centres in a bulk crystal. The tetragonal (A) and the cubic (O) centres were chosen due to the strong PL intensity. Their

transition spectra in the SL are compared with the A and the O centres in a bulk crystal and are shown in fig. 5.4 and fig. 5.5, respectively. Also the excitation and emission spectra of each center were added in fig. 5.4 and fig. 5.5 for clarification.

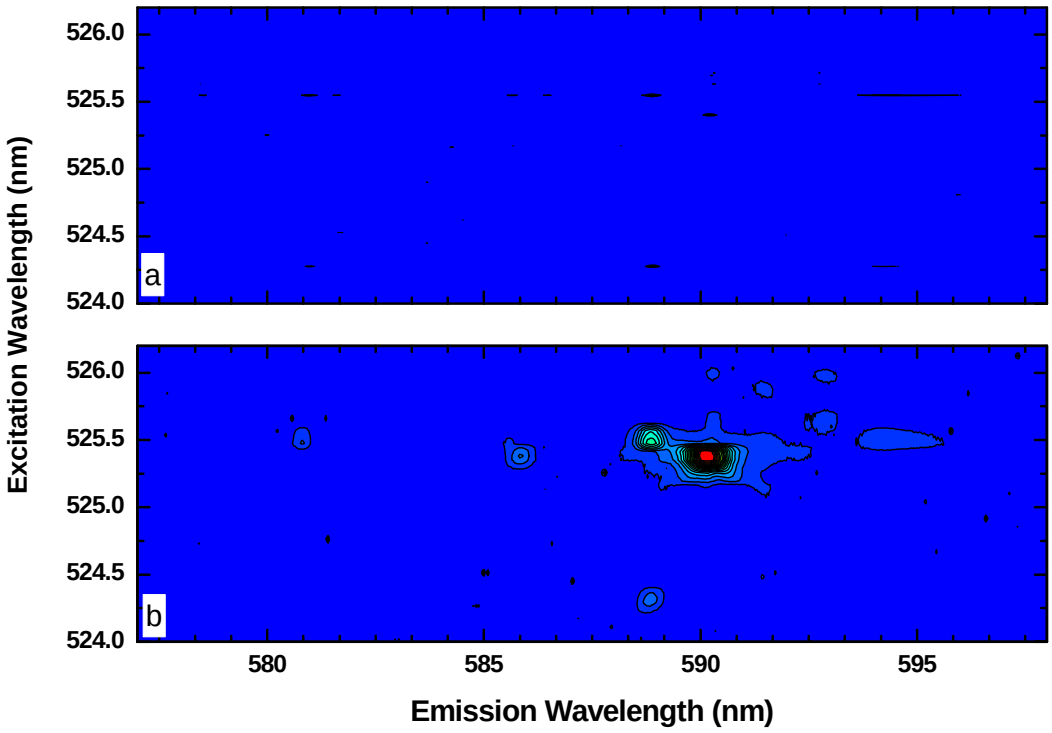

Fig. 5.3. Contour plots of (a) CaF_2:Eu bulk crystal and (b) CaF_2:Eu-CdF_2 SL. The excitation took place via the $^7F_0 \rightarrow {}^5D_1$ transition. The emission was from the $^5D_0 \rightarrow {}^7F_1$ transition. All spectra were recorded at ~ 4K.

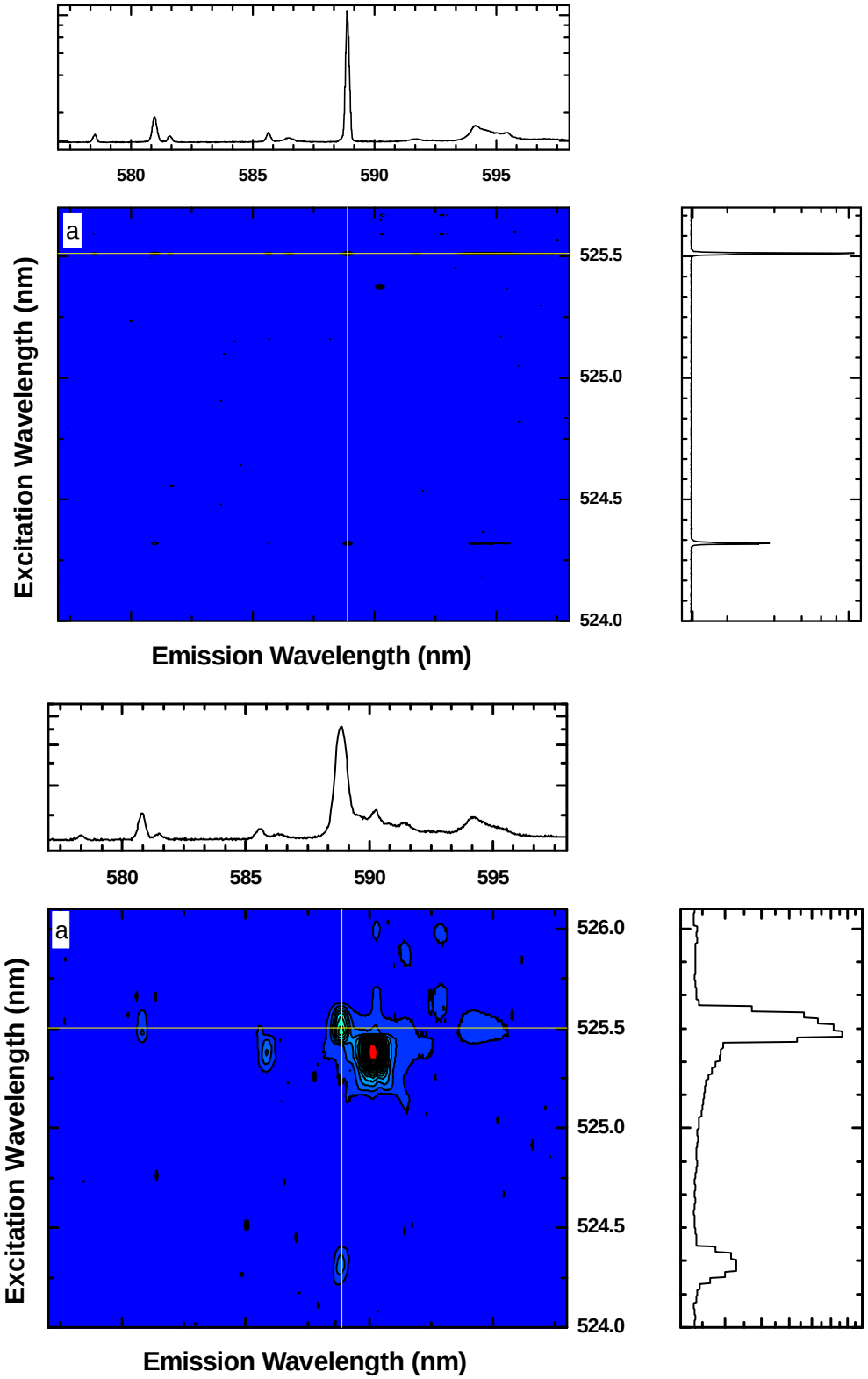

Fig. 5.4. Excitation and emission spectra of the tetragonal A centre in (a) bulk crystal and (b) in a SL. Each top graph of the contour plot represents corresponding emission spectrum and the right graphs are excitation spectra of each centre. All spectra were recorded at ~4 K.

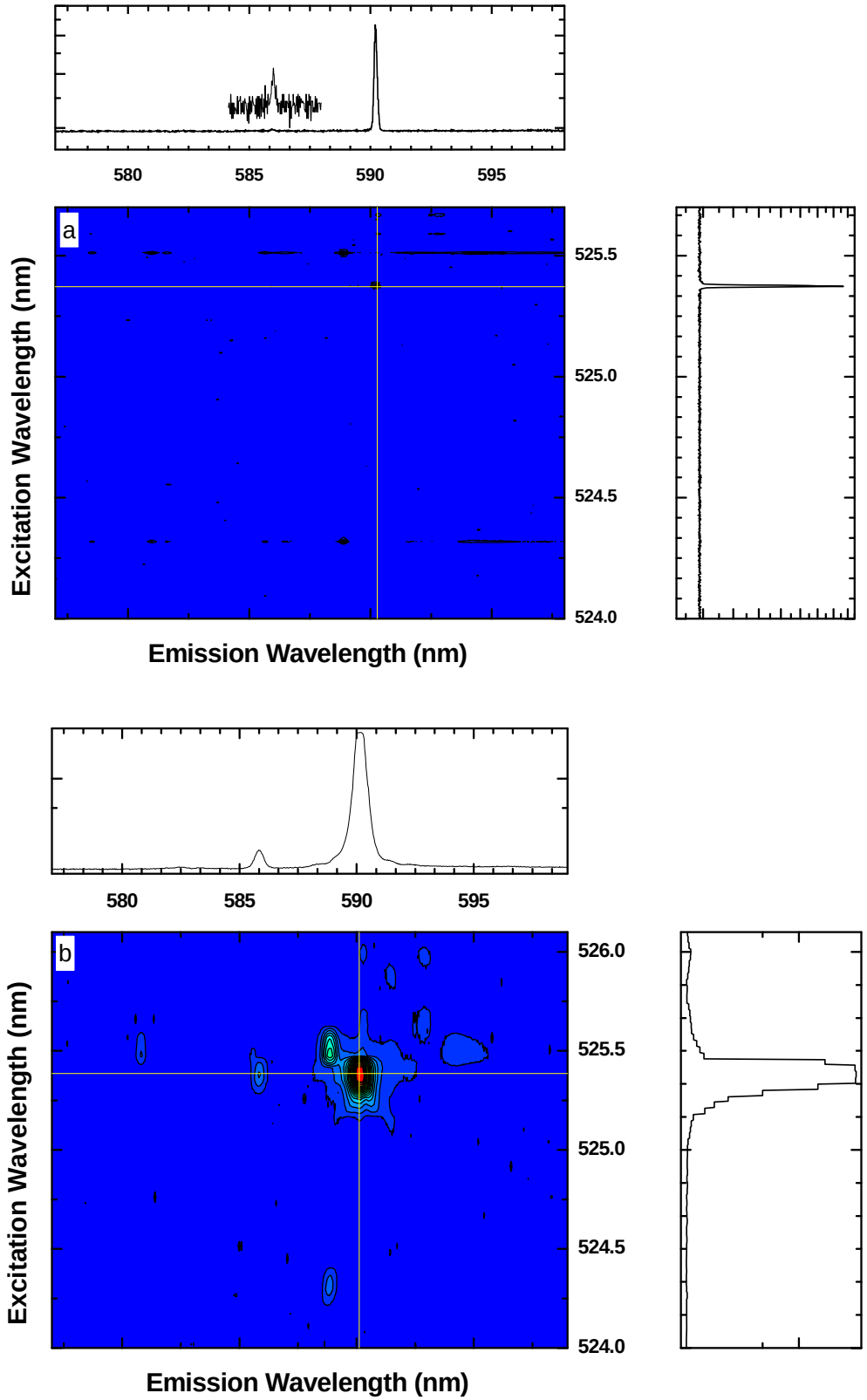

Fig. 5.5. Excitation and emission spectra of the cubic O centre in (a) bulk crystal and (b) in a SL. Each top graph of the contour plot represents corresponding emission spectrum and the right graphs are excitation spectra of each centre. All spectra were recorded at ~4 K.

In particular, transitions involved with $^7F_0 \rightarrow {}^5D_1$ excitation and $^5D_0 \rightarrow {}^7F_1$ emission of Eu^{3+} were chosen from SLs to compare with the same transitions for Eu^{3+} in a bulk crystal. For SLs, the A centre was observed with a very weak signal, however it was confirmed as a tetragonal centre. Emission and excitation spectra were coincident with the A centre transition in bulk as reported previously [1, 6]. This also implies that charge compensation took place during the MBE growth. Similarly, the O centre was observed from SLs and confirmed by comparing its emission and excitation spectra with the cubic centre transition in bulk crystal.

The PL intensity of Eu^{3+} from the O centre in SLs and in thin films was stronger than in the bulk crystal. This is possibly due to high dopant concentration of Eu^{3+} in these SLs and thin films. It is well known that the cubic centre concentration increases relative to other single Eu^{3+}-F^- paired centres, such as the A centre, with increased dopant concentration [1, 3]. A typical concentration of ~ 0.3% of Eu defects was used in the growth of the SLs and thin films. The bulk crystal used in this study contains 500 ppm (0.05%) of Eu. Hence the cubic centre is expected to be increased in the SLs and thin films.

It is the crystal directions of the interstitial F^- charge compensator which determines the local symmetry of Eu^{3+} defects. The symmetry of the A centre is tetragonal as the interstitial F^- occupies the centre of the neighbouring cube in a [100] direction. The symmetry of the O centre is cubic with the interstitial F^- remote from the Eu^{3+} site. Similarly an interstitial F^- could also occur in a [111] direction giving a trigonal symmetry, however this centre is not observed in bulk CaF_2:Eu or in SLs. It is well known that the trigonal centre is not observed for small dopants such as Eu in a CaF_2 host [4]. The trigonal symmetry is observed for heavier ions.

The bulk crystal did not provide any comparison for symmetry assignment of the I centre. For that reason polarisation anisotropy was studied for the I centre to elucidate the local symmetry of the Eu^{3+} defect. The experimental set up is illustrated in fig. 5.6. The sample inside the cryostat was rotated so that the surface normal of the sample was ~50º away from the surface normal of the cryostat window. In such a configuration the dye laser excitation was incident on the sample in a glancing angle with the E vector polarisation

either perpendicular or parallel to the c axis of the sample. In fact when the E vector is said to be parallel, denoted by an arrow, to the c axis, it means that dominant component of the vector is parallel to the c axis. The magnitude of the component can be as large as 90%, but it never reaches to 100% due to the geometrical limit. When the polarisation of the laser is rotated by 90º, represented by a circle in fig. 5.6, it makes the incident polarisation perpendicular to the c axis regardless the incident angle. Similarly collection of PL of Eu^{3+} can also be polarised by using an analyser in the collection path. The analyser only allowed PL that is either polarised perpendicular (circle) or parallel (arrow) to the c axis of the sample. Again, a component of the polarisation of the analyser is parallel with the c axis due to the geometry.

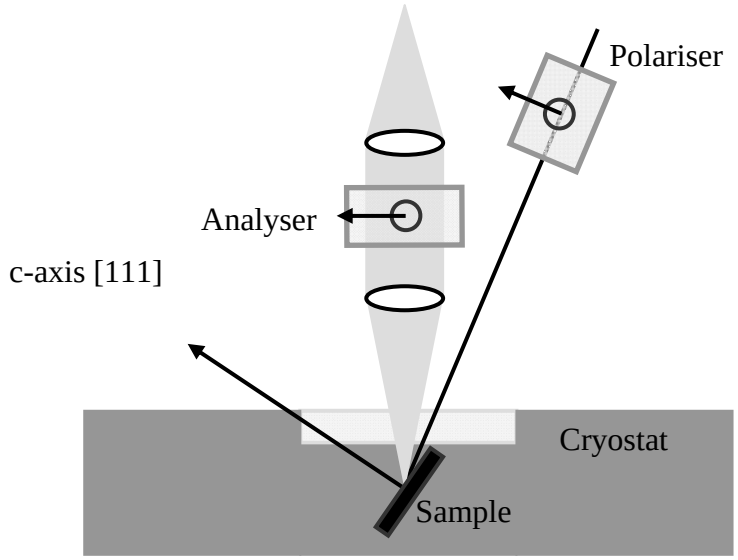

Fig. 5.6. Schematic (top view) of the polarisation anisotropy set up. Note that the circle inside the polariser indicates that the E vector of the laser is pointing out of the page. Similarly the circle inside the analyser indicates that only that vector of emission is allowed. The arrows indicate the opposite polarisation with the E vector rotated by 90º.

Notations of π and σ were used to describe polarisation of the laser and the analyser. π-polarised excitation is for the E vector parallel to the c axis (E||c [111]) of samples and σ-polarised excitation indicates the E vector is perpendicular to the c axis (E $\perp$ c [111]). In a similar sense the π-polarised analyser allows collection of emission that is polarised parallel to the c axis and the σ-polarised analyser allows emission that is polarised perpendicular to the c axis. As a result, further splitting of the $^5D_1$ and $^7F_1$ energy levels

of Eu^{3+} in the I centre were observed provided by polarised excitation and emission. It should be noted that the polarisations are expressed with respect to the E vector for the experimental convenience (fig. 5.7). To demonstrate the transition polarisation nature for the I centre, it should also be noted that π is expressed as σ′ and σ to π′ where the 'prime' is used for an indication of the magnetic vector in the case of transitions of the I centre allowed through magnetic dipole (fig. 5.8).

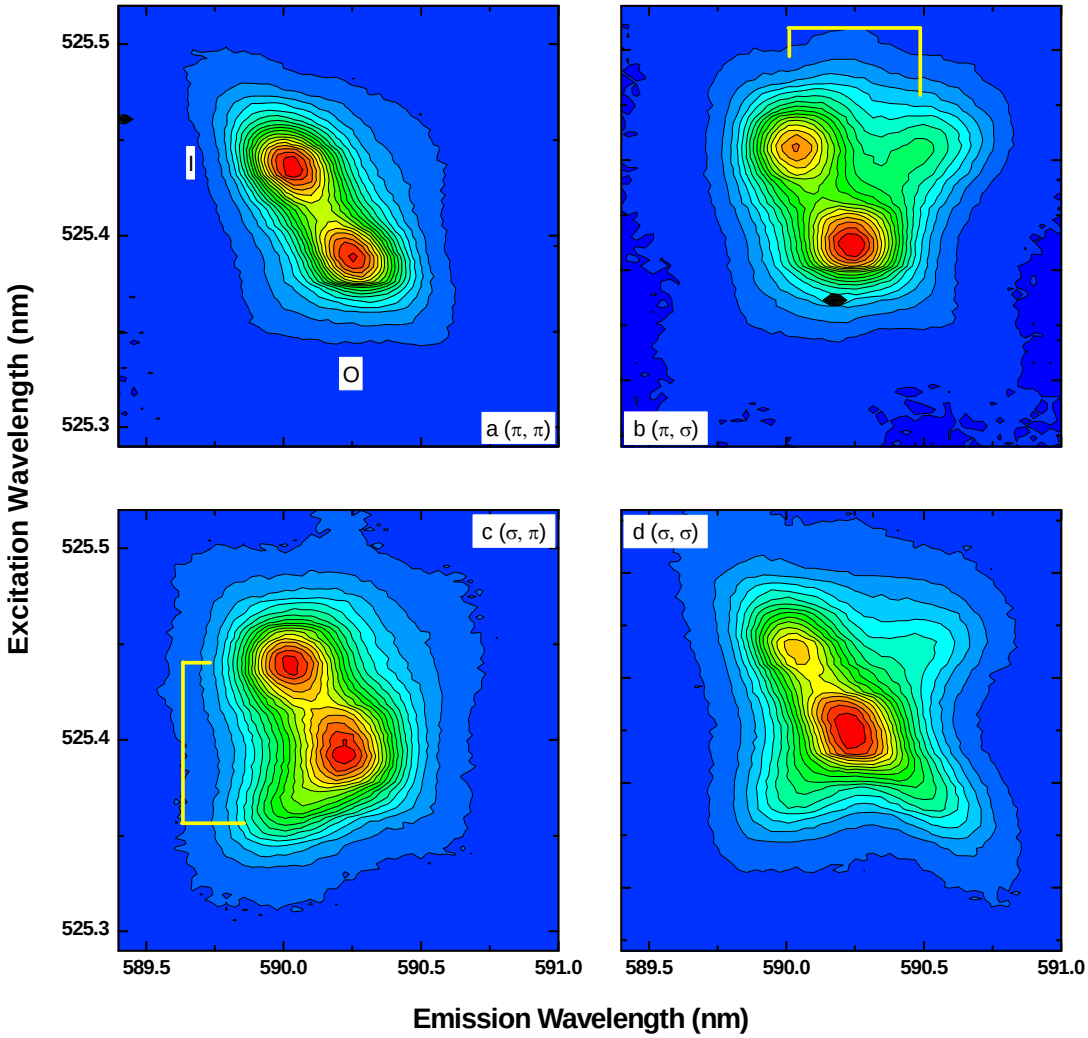

Fig. 5.7. Contour plots of polarised CEES on a 3 ML SL (SL 3173). Four combinations of polarisation in excitation and emission are considered: (a) π-polarised excitation and emission; (b) π-polarised excitation and σ-polarised emission; (c) σ-polarised excitation and π-polarised emission; (d) σ-polarised excitation and emission. All spectra were recorded at ~4 K. Note that the polarisations are expressed with respect to the polarisation of the E vector.

As shown in fig. 5.7(c), a splitting in the $^5D_1$ level is revealed under σ-polarised (π′) excitation but not under π-polarised excitation (fig. 5.7(a)). Also a splitting in the $^7F_1$ is observed under σ-polarised (π′) emission. The cubic centre is not affected by polarised excitation and emission and hence confirmed to be cubic symmetry.

Based on the polarisation anisotropy of the I centre one can construct a polarisation assignment to the energy levels of Eu^{3+} as shown in fig. 5.8. It is instructive to notice that the splitting (regardless the magnitude) of the energy levels provided by polarised excitation and emission are exactly matching with the expected polarisation selection rules for the trigonal (C_{3v}) symmetry which is also represented in table 5.1.

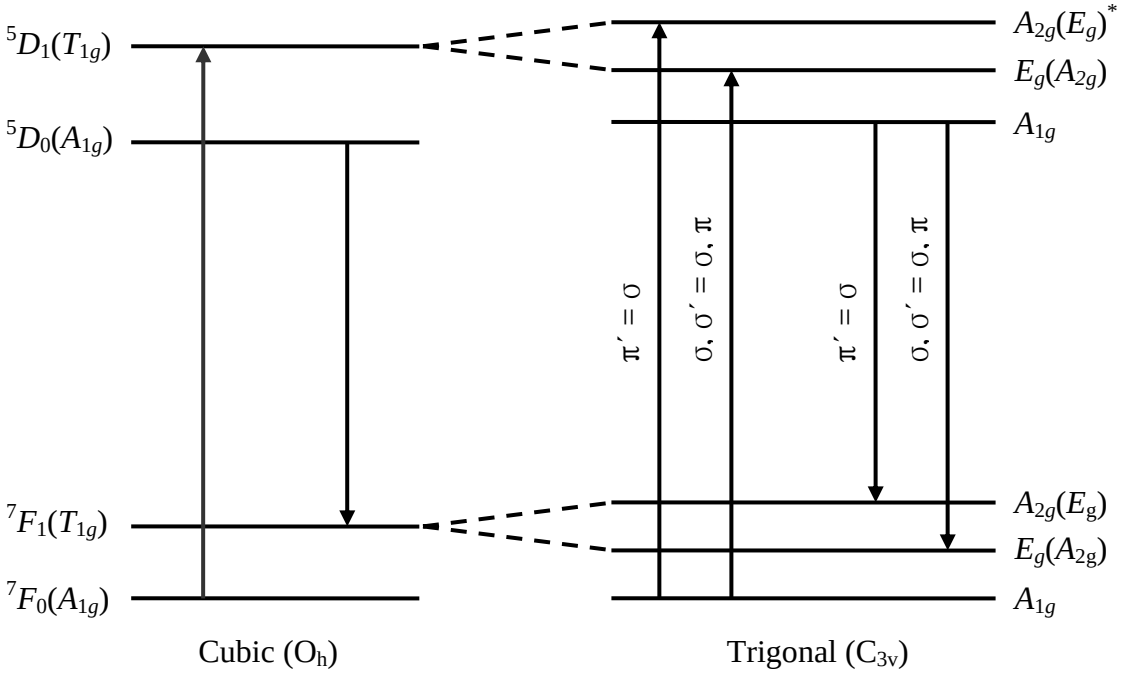

Fig. 5.8. Energy levels and polarisation assignments for optical transitions of Eu^{3+} in cubic and C_{3v} symmetry. The energy levels are not drawn to scale.

*The values inside the brackets are the polarisation assignments for a distorted O centre in thick SLs as discussed in later section.

Table 5.1. Polarisation transition selection rules for Eu^{3+} ion in the C_{3v} symmetry. The prime indicates the magnetic dipole transitions

C_{3v}	A_{1g} (Γ_1)	A_{2g} (Γ_2)	E_g (Γ_3)
A_{1g} (Γ_1)	π	(π′)	σ (σ′)
A_{2g} (Γ_2)	(π′)	π	σ (σ′)
E_g (Γ_3)	σ (σ′)	σ (σ′)	π, σ (π′, σ′)

In C_{3v} symmetry of Eu^{3+}, the $^5D_1$ and $^7F_1$ levels (J = 1) are split into two levels [7]. As discussed in chapter 2 these levels are identified with irreps of A_{2g} and E_g. However the $^5D_0$ and the $^7F_0$ remain unsplit (A_{1g}). In the $^7F_0 \rightarrow {}^5D_1$ transition of Eu^{3+} in C_{3v} symmetry, provided by σ-polarised excitation, the A_{2g} level is excited. It should be corrected, according to the selection rules, the $A_{1g} \rightarrow A_{2g}$ transition is only allowed through magnetic dipole process. Hence the polarisation should be denoted as π′ knowing that σ and π′ are orthogonal. For the $A_{1g} \rightarrow E_g$ transition, two transitions are allowed through magnetic (σ′) and electric (σ) dipole processes. Here σ′ is re-written as π. This explains why we observe the dominant I centre under both polarisations of excitation light. Hence the weak shoulder appearing in the excitation wavelength is assigned as A_{2g} while the dominant peak is assigned as E_g. The same selection rules are invoked for the emissions and the results are the same. Hence the symmetry assignment for the I centre is most likely to be trigonal C_{3v}.

The energy separations in the $^5D_1$ and in the $^7F_1$ splittings were extracted by projecting Gaussian curves beneath the emission and the excitation spectra of the I centre. Multi peak fitting from Igor Pro was used and the fitting results are shown in fig. 5.9. The energy separation in the $^5D_1$ splitting was obtained by resolving three peaks under the excitation spectrum shown in fig. 5.9(d). As the I centre and the O centre were energetically very close to each other, including a peak representing the cubic transition gave a more precise fit. The position of the cubic excitation peak was found beforehand and was fixed during the fitting. The resulting energy level splitting in the $^5D_1$ level is 2.5 cm^{-1}. Similarly for the $^7F_1$ level, using two peaks in the fitting, the splitting of that level is

given by 13.2 cm^{-1}. These values are used in energy level calculations which are discussed in chapter 7.

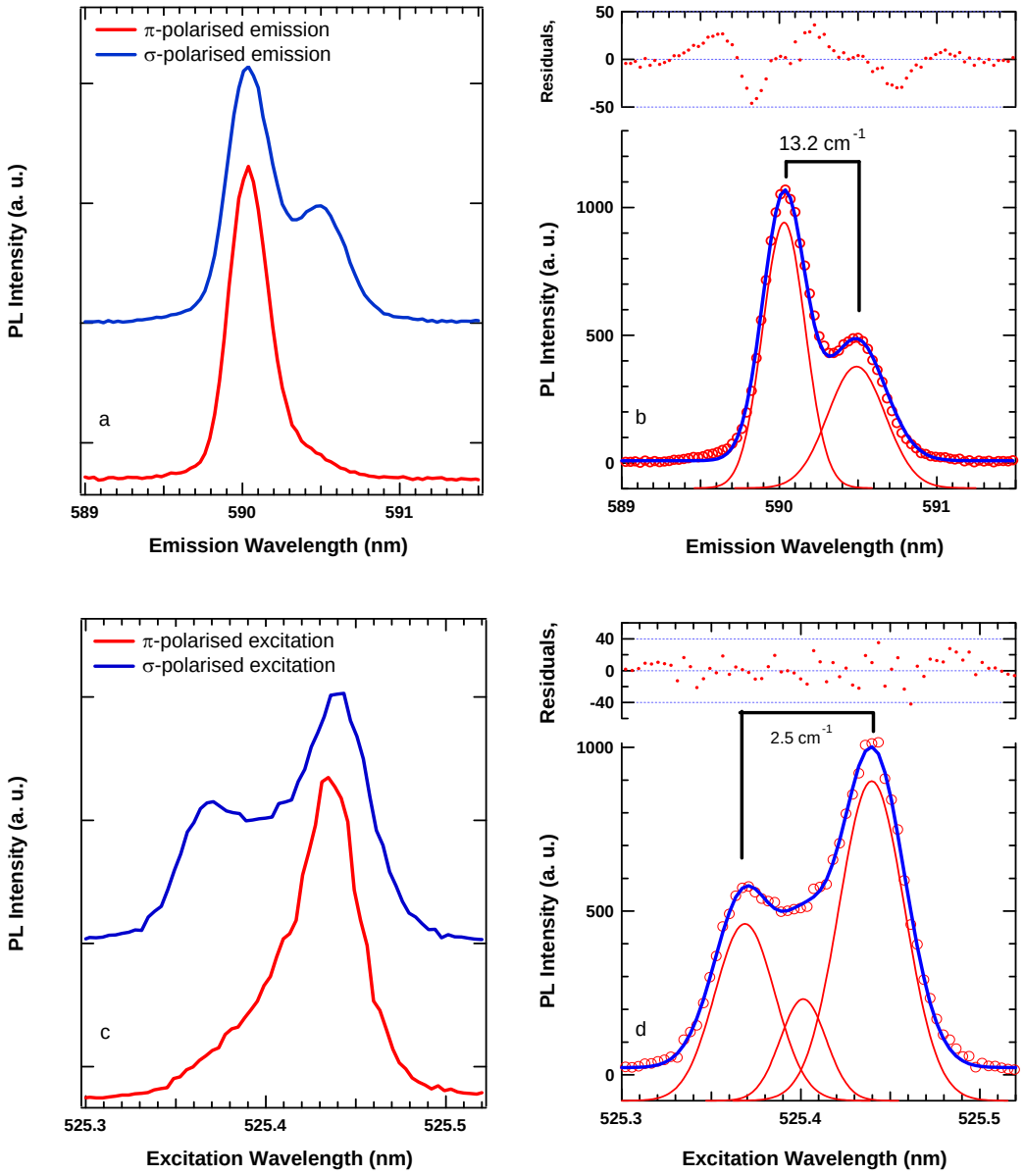

Fig. 5.9. Polarisation anisotropy of Eu^{3+} in trigonal symmetry (C_{3v}) for (a) polarised excitation and (c) polarised emission. Multi peak fitting from Igor Pro was used to determine the PL position of the weak shoulders appearing in (b) emission and (d) excitation. Note that three Gaussian curves were used in (d) for better fitting. Cubic transition was included in the fitting as the transitions were too close to each other (refer to fig. 5.7(c)).

It is instructive to address the possible role of Cd^{2+} ions in the formation of the interface centre which only seems to be present in SLs. In the consideration of Cd^{2+} ions in the vicinity of Eu^{3+}, the energy levels of the I centre are shifted from the O centre due to a different symmetry caused by Cd^{2+} ions at the interface. In fact, at the interface there are three neighbouring Cd^{2+} ions seen from a Eu^{3+} ion whereas a cubic Eu^{3+} sees twelve Ca^{2+} cations. Jouart *et al*. [2] reported the transition energy level ($^5D_1$) for the cubic centers respectively in CaF_2 and CdF_2 as 19,030 and 19,023 cm^{-1} which show a 7 cm^{-1} shift when all 12 cations around the Eu^{3+} are changed from Ca^{2+} to Cd^{2+}. In fact 3/12 of this shift is 1.8 cm^{-1} which is very close to the observed shift which is observed as 1.8 ± 1.4 cm^{-1}. On the other hand, the $^5D_0 \rightarrow {}^7F_1$ emission transitions for the cubic centers in the two pure crystals are within $\pm$ 1 cm^{-1} whereas here we observe an emission shift for the I and the O centre of 6 ± 1 cm^{-1} [8]. Hence the symmetry change due to Cd^{2+} ions is not believed to be sufficient to explain the shift of transition energies.

A more convincing scenario is the possible role of electrons in the vicinity of Eu^{3+}. It was suggested in chapter 4 that PL growth of the Eu^{3+} in cubic centre under UV excitation at low temperature is related to transfer of electrons. The basis of that assumption is valid through an existence of electron charge compensated centre of Eu^{3+}. The transfer of the electrons suggested is thought as delocalisation of charge compensating electrons which only have mobility at low temperature. The electrons either in CaF_2 or in the conduction band of CdF_2 are possibly subject to charge compensation. In fact, Kingsley and Prener [9] have reported that charge compensation can be provide by electrons in the conduction band or in shallow traps in the case of trivalent lanthanoids doped in CdF_2. It is quite possible for electrons, whether they are in conduction band of CdF_2 or in traps of CaF_2, are responsible for charge compensation. As a result, deformation of the cubic centre due to extra charge is expected by the presence of electron in the vicinity of an otherwise uncompensated Eu^{3+}. For that reason the I centre is quite possibly formed by electron charge compensation. Hence this centre is expected to exhibit PL bleaching connected with the PL increase of the cubic Eu^{3+}. In the following sections delocalisation of electrons and therefore transformation of the I centre to the O centre is discussed.

In addition to the I centre energy level splitting, the cubic centre also shows possible splittings under polarised excitation and emission spectra. Such a splitting is not observed for thin SLs. Two thick SLs $(CaF_2{:}Eu)_{20}$-$(CdF_2)_{20}$ were chosen and investigated in the same way as the polarisation anisotropy was studied for thin SL (as shown in figs 5.7 and 5.9). In the investigated SLs, both consisting of 20 ML thick CaF_2 layers, the cubic centre was split in σ-polarised excitation (E ⊥ c [111]) and emission. The CEES for one of the sample is shown in fig. 5.10.

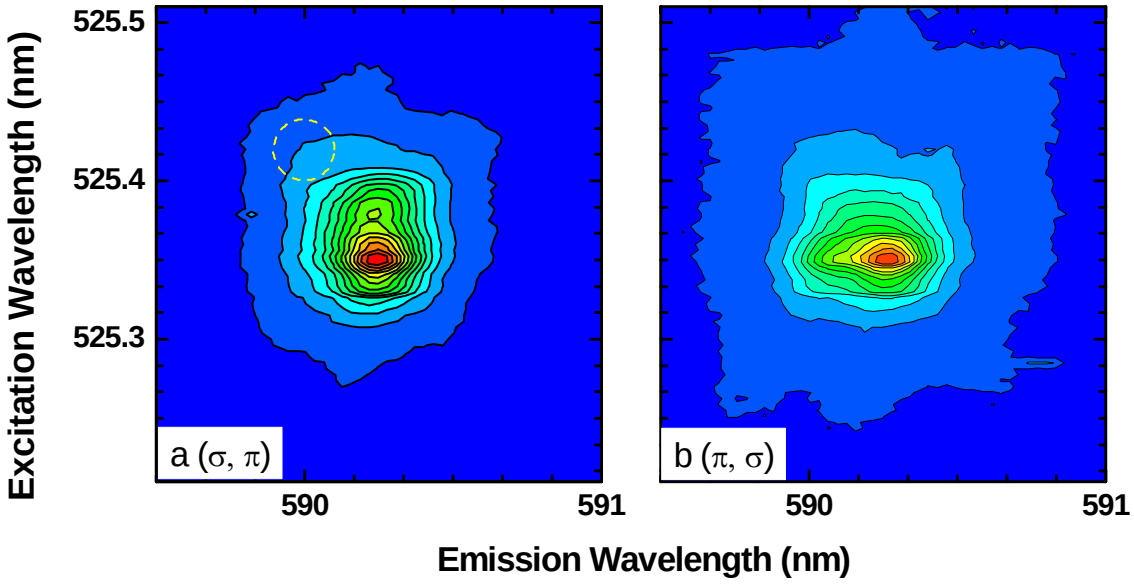

Fig. 5.10. CEES of Eu^{3+} in a cubic centre in $(CaF_2{:}Eu)_{20}$-$(CdF_2)_{20}$ SL. (a) σ-polarised excitation and π-polarised emission and (b) π-polarised excitation and σ-polarised emission. The expected transition wavelengths of the I centre are indicated by a dashed circle. All spectra were recorded at 4 K.

It should be noted that, compared to the splitting observed for the I centre, the degree of splitting of the O centre is different and the level assignment is opposite. The splittings are further analysed by multi peak fittings, as shown in fig. 5.11, and the values are obtained as 1.38 cm^{-1} and 6.4 cm^{-1}, respectively for in the $^5D_1$ and the $^7F_1$ multiplets. For comparison the I centre splittings are 2.5 cm^{-1} and 13.2 cm^{-1}. The degree of the splitting for the O centre is around half that of the I centre. It was also found that the doublet (E_g) is higher in energy in the $^5D_1$ and the $^7F_1$ multiplets as opposed to the I centre. It is hard to believe that a charge-compensating electron is the major cause of the splitting. In fact, one can see a weak shoulder appearing near to the O centre in the longer excitation and the shorter emission wavelengths at which the I centre was observed from thin SLs (fig.

5.10). Hence apart from the already existing I centre, the cubic centre is further perturbed by the additional crystal environment. The fact that the splitting in the O centre is associated with the thick SLs suggests that the splitting is associated with strain of the SLs [10]. The XRD data for the SLs have shown that there is possible deformation of the crystal structure from cubic to lower symmetry structure in SLs [10]. Hence the reduction of the symmetry is influential for the splitting of the cubic centre.

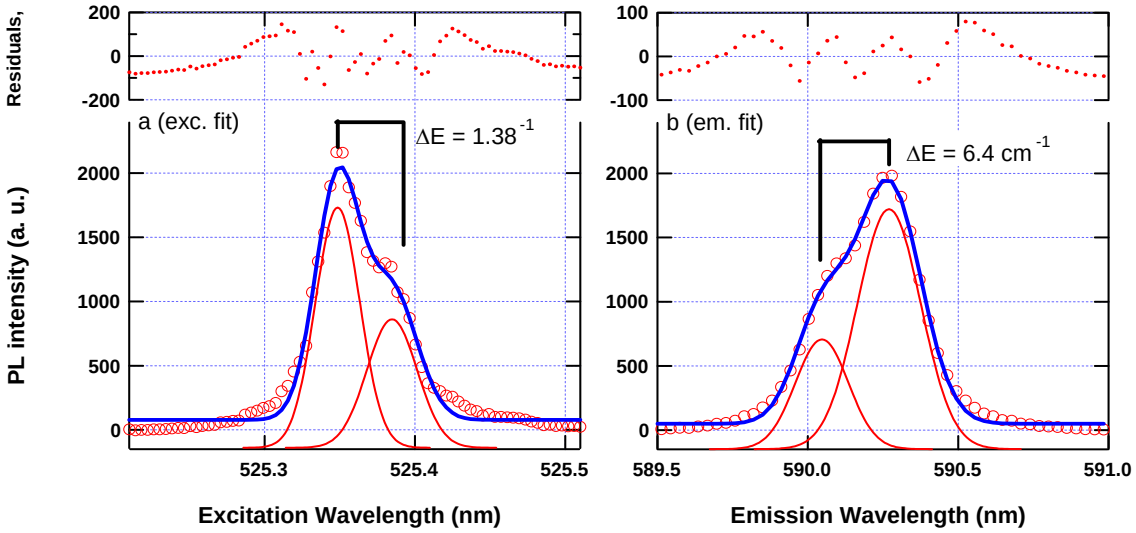

Fig. 5.11. Multi peak fitting results of the splitting of the O centre in (a) excitation and in (b) emission spectra. The doublets are energetically higher than the singlet for both $^5D_1$ and the $^7F_1$ multiplets.

By examining table 5.1, the polarisation selection rules for the 'distorted' cubic transitions are consistent with the C_{3v} symmetry. The weak splitting of the O centre in σ polarisation is considered as a singlet (A_{2g}) which is an allowed transition through magnetic dipole (π´). The dominant O centre transition is then doublet (E_g) which is allowed in both polarisations (fig. 5.8). However the transitions for the singlet are forbidden in either σ´ (π) polarised excitation or emission. Based on these observations we conclude that the symmetry of the distorted O centre is best described as a C_{3v}.

In section 5.3, the splitting of the O centre is considered as a result of the distortion of the crystal structure of the SLs. The values of the splitting are used in calculation of the appropriate crystal field parameters.

5.2.2 Thickness dependence of Eu^{3+} centres in CaF_2:Eu-CdF_2 superlattices

As described in section 5.1, PL of the I centre has shown anomalous behaviour on varying thickness of CaF_2-CdF_2 SLs. As shown in fig. 5.12, the PL intensity of the I centre is very sensitive to the thicknesses of the host CaF_2 layers. It was observed that transition wavelengths of the I centre, relative to the cubic centre, were not changed while its PL intensity changed with the thickness. In other words no change in PL wavelengths between the I centre and the O centre is observed. This suggests that the PL intensity is quantised by the thicknesses of SLs and also rules out the possibility that I centre is derived from O centre due to the thickness changes in SLs. Moreover in a 2 ML thick SL, the I centre was dominant while the cubic centre was almost undetectable (see also fig. 5.14).

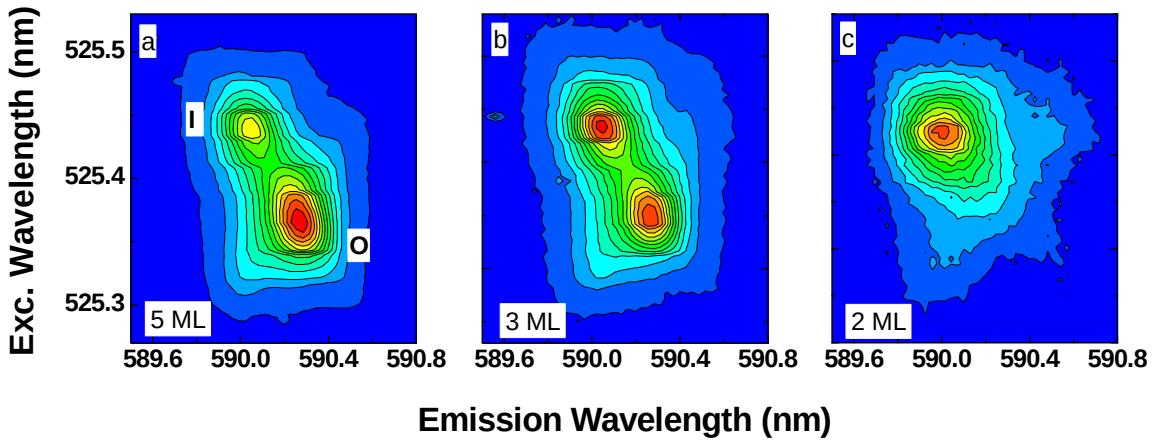

Fig. 5.12. High resolution CEES of symmetric SLs with different CaF_2-CdF_2 thicknesses (a) 5ML (b) 3ML and (c) 2ML. All spectra were recorded at 4K.

In this subsection PL intensities of the I and the O centre were compared with respect to the thickness of various SLs. This was carried out by selecting elements of the raw data matrix which projects both peaks of the I and the O centres as shown in fig. 5.13. Then the profiles of emission and excitation can be re-plotted. Multi peak fitting using Igor Pro enabled peak values of the I and the O centres to be found. Fig. 5.14 shows PL intensities, as well as Gaussian fittings, of the I and the O centres in various SLs hosts of different thickness.

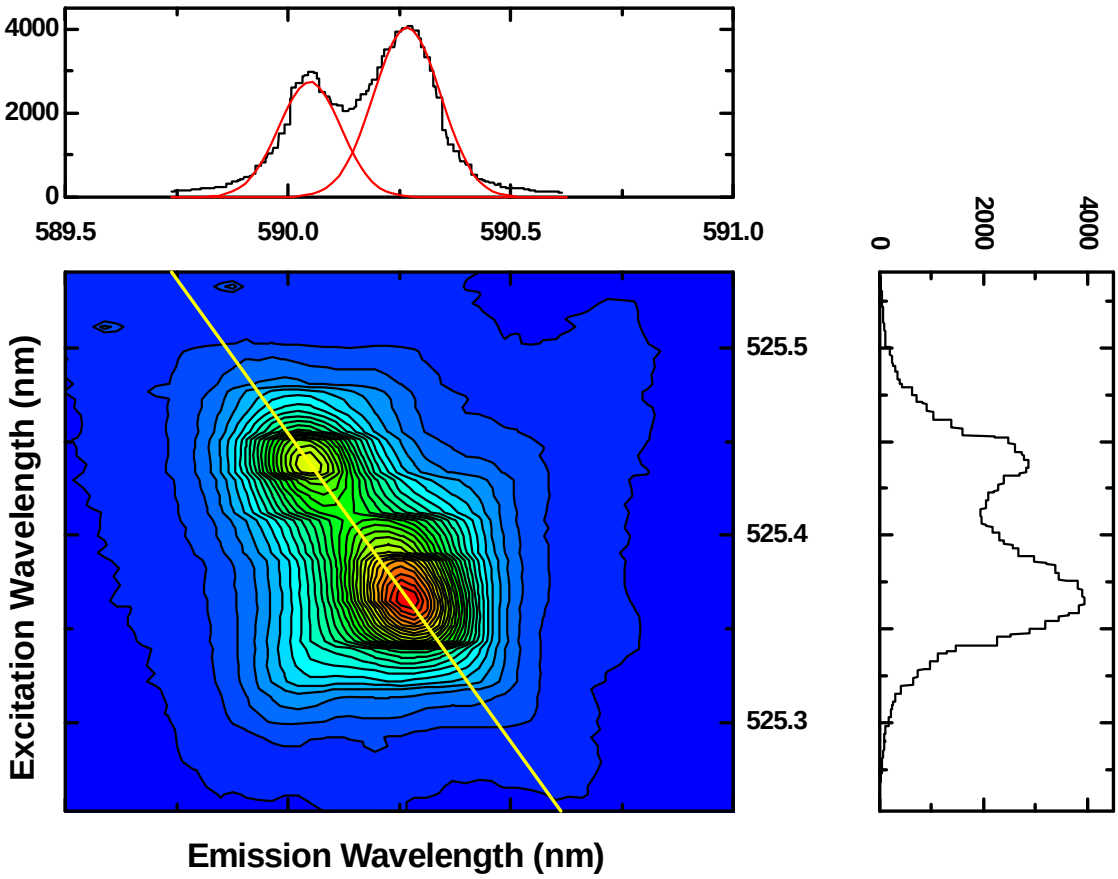

Fig. 5.13. Profile of emission and excitation spectra of a 7 ML SL (SL3172). Two Gaussian peaks were used to resolve the PL spectrum linking the I and the O centres. The top graph shows the emission profile of the I and the O centre with two Gaussian peaks beneath the PL spectrum and the right graph shows the excitation profile of the centres.

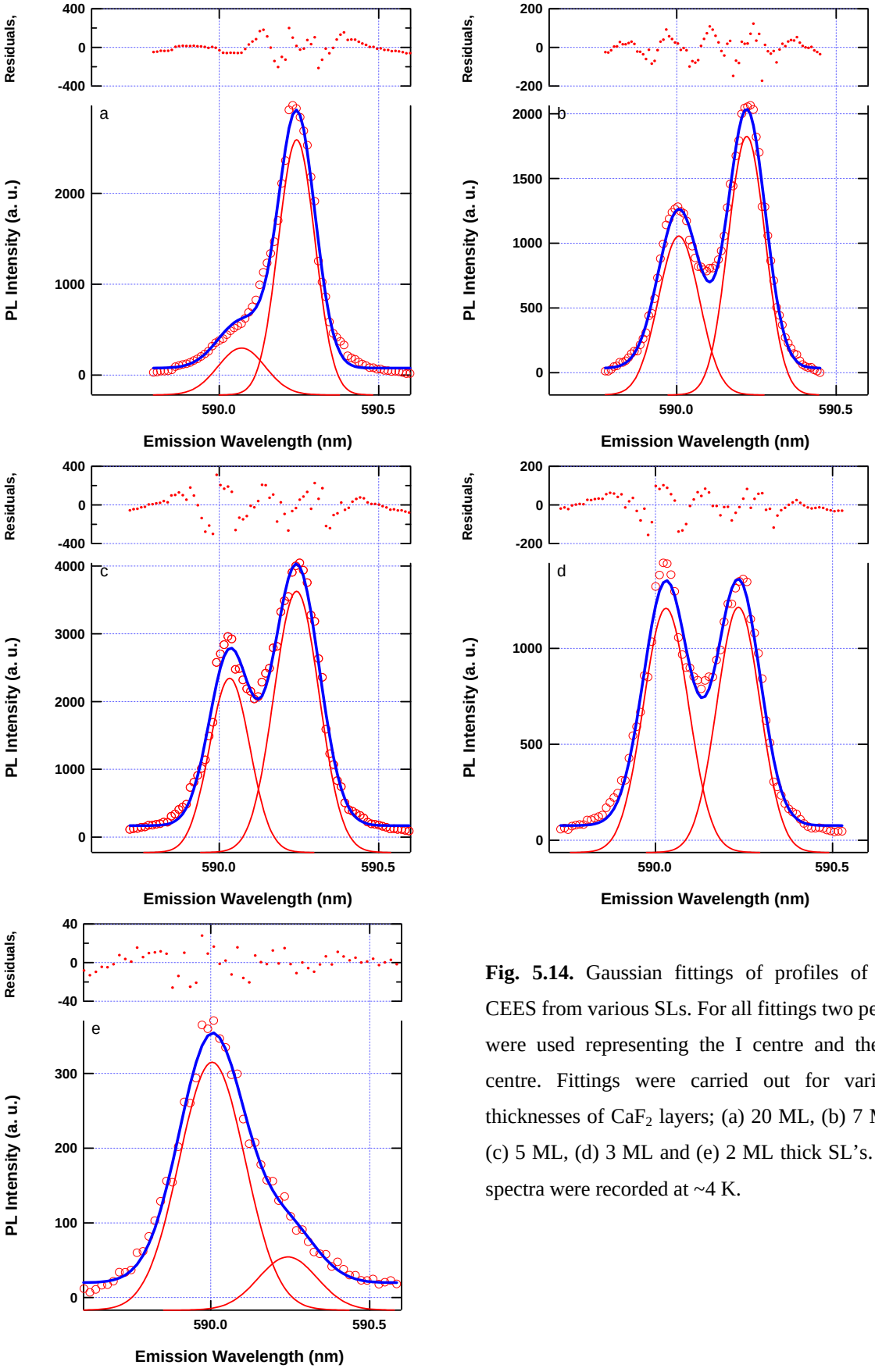

Fig. 5.14. Gaussian fittings of profiles of the CEES from various SLs. For all fittings two peaks were used representing the I centre and the O centre. Fittings were carried out for various thicknesses of CaF_2 layers; (a) 20 ML, (b) 7 ML, (c) 5 ML, (d) 3 ML and (e) 2 ML thick SL's. All spectra were recorded at ~4 K.

As a result, the PL intensities of both centres were significantly influenced by the thickness of the hosts. For example, in a 20 ML thick SL, the I centre appeared as a weak shoulder relative to the O centre (fig. 5.14(a)), however this was reversed in a 2 ML thick SL (fig. 5.14(e)). Based upon the observations it was realised that the PL intensities of the I (PL_I) and the O (PL_0) centres, at low temperature, can be written in terms of the layer thickness, D, as ,

$$PL_O \propto (D-2)N,$$
$$PL_I \propto 2N, \qquad (5.1)$$

where N is the number density of excited Eu^{3+} ions equally distributed in CaF_2 layers. This is because the formation of the I centre is only possible at the top and at the bottom of the CaF_2 layers regardless their thickness. It is schematically shown in fig. 5.15 that the 1st and the D^{th} layers are responsible for the formation of the I centre. The layers between the 2nd and the (D-1)th layers are believed to contain normal cubic centre.

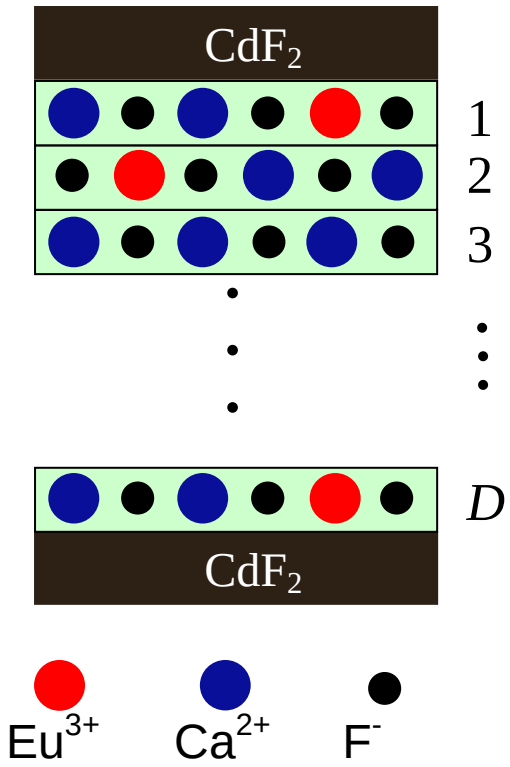

Fig. 5.15. Diagram of Eu^{3+} deposition in a D ML thick SL. The I centre is only formed at the 1st and the D^{th} layers of CaF_2. The normal cubic (O) centre forms between the 2nd and the (D-1)th layers.

For example, in a given SL which is 10 ML thick, the proportion of Eu^{3+} ions that contribute to the I centre is 0.2, and 0.8 is the proportion of Eu^{3+} that are contributing to the cubic emission. Hence the PL ratio between the O and the I centre is readily expressed in terms of MLs. One can modify (5.1) by introducing a proportionality constant, *C* and then the PL ratio becomes as below

$$\frac{PL_O}{PL_I} = \frac{(D-2)C}{2} + B, \quad (2 \le D < \infty). \tag{5.2}$$

Here *B* is not fixed at zero as the cubic centre is still detectable from a 2 ML thick SL. According to equation (5.2) a linear relationship of PL ratio between the O and the I centre with the thickness of SLs is expected.

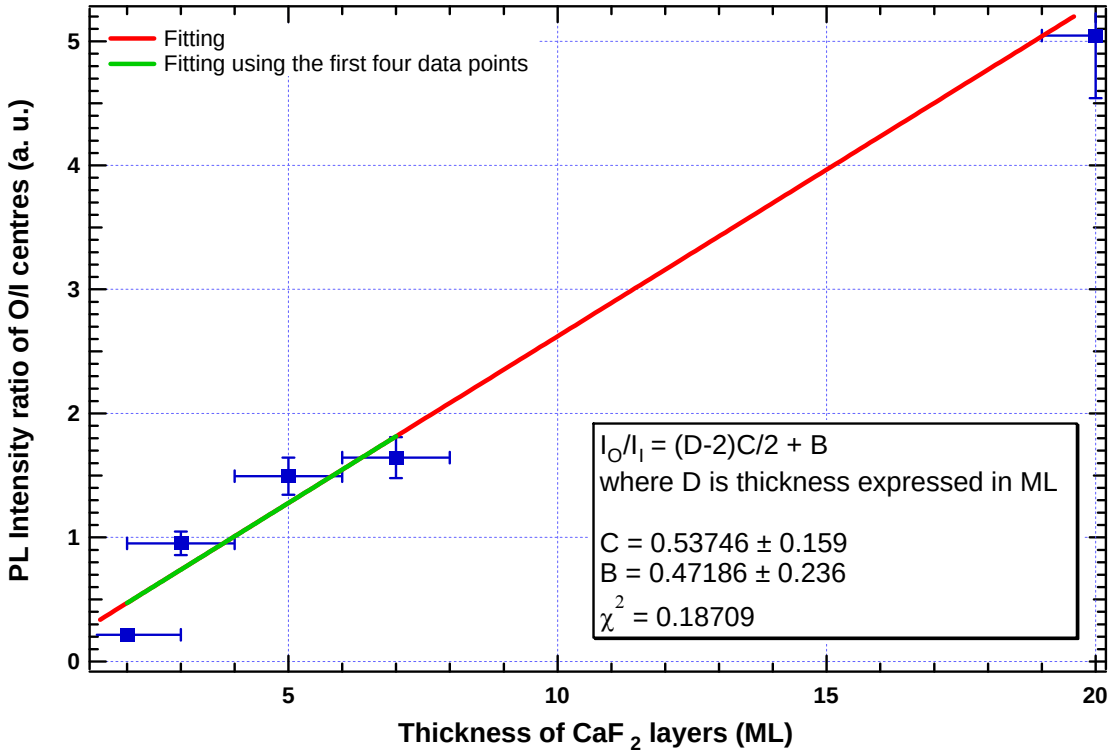

Fig. 5.16. PL ratio between the I centre and the O centre with respect to the thickness of CaF_2-CdF_2 SLs. The thickness is expressed in ML with technological uncertainty of ± 1 ML. Linear fitting was also carried out using (5.2) and the fitting coefficients are shown in the inset.

Fig. 5.16 shows a good fitting result of (5.2) with experimental data with χ^2 value of 0.18709. The error bars are provided by the technological limit of $\pm$ 1 ML thickness control in MBE growth. Here 1 ML is defined to be a complete F-Ca-F layer grown on Si [111] substrate [11, 12] whose thickness is 3.15 Å [12]. Also the errors in the PL ratios are found by evaluating intensity difference between the raw data and the fitted value at each peak. It should be noted that the 20 ML SL has a larger uncertainty in the PL ratio due to the resolving limit of the peaks. Additional fitting which exclude the 20 ML data point in fig. 5.16 also gave the same fitting results. Hence the 20ML SL is well inside the trend of the rest of the samples. The above relationship confirms that the PL intensity ratio between the O and the I centre is quantised with the thickness of CaF_2 layers. The possible number of layers that contain the I centre of Eu^{3+} is fixed as two regardless of the SL thickness. These layers are described as the first and the last layers, or, the top and the bottom layers of the given CaF_2 layers. The crystal environment of these interface layers is obviously different in comparison to the layers deposited in the middle (from the 2^{nd} to the $(D\text{-}1)^{th}$ layers) of the CaF_2.

5.2.3 Temperature dependence of Eu^{3+} photoluminescence in CaF_2:Eu-CdF_2 superlattices

As mentioned in section 5.1, the PL behaviour of the I centre with temperature is somewhat different to the cubic centre. To follow up the previous observation that the PL intensity of the I centre quenched faster than the O centre, an electron delocalisation model was proposed. It was first assumed that the electrons are responsible for the formation of the I centre. In fact, Kingsley and Prener have reported that electrons in the conduction band or in shallow traps can be act as charge compensator in CdF_2 [9]. Similar to the latter case, the existence of traps inside the CaF_2 host, was not considered previously [5], however, it should be considered here. Following chapter 4 some electrons are likely to be trapped inside CaF_2 layers. Hence the electrons trapped in the vicinity of the interface Eu^{3+} ions possibly result in charge compensation. The lower crystal symmetry of Eu^{3+} centre at the top and the bottom of CaF_2 layers is likely provided by a localised electron along the [111] axis as schematically shown in fig. 5.17. These

electrons are provided by ionisation of the Eu^{2+} excited state as described in the previous chapter and reported by the collaborators elsewhere [13-15]. However as described in chapter 4, there is lack of experimental evidence that the released electrons are contributing to the charge compensation. Regardless of their origin, the electrons are not localised in the vicinity of those Eu^{3+} ions in the middle of the CaF_2 layer leaving Eu^{3+} centres uncompensated.

It was further assumed that the electrons are localised at the bottom of the conduction band of CdF_2 and become a bound state at low temperature having binding energy, E_b. Similarly the same situation holds for the trapped electrons in the CaF_2 layer. The bound electrons are said to be delocalised when they gain sufficient energy by thermal excitation. Upon this delocalisation the electric field produced between the bound electron and the Eu^{3+} no longer holds. This eventually makes no difference in terms of charges surrounding Eu^{3+} ions between cubic and interface (trigonal at low temperature) centres. One might therefore expect to see transformation of the I centre into the O centre at elevated temperatures. The observed CEES results of the I and the O centres with different temperatures are shown in fig. 5.18.

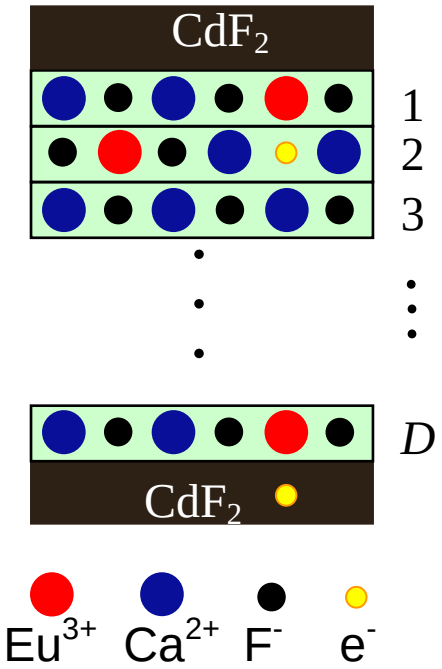

Fig. 5.17. Schematics of conduction band electrons vicinity to the Eu^{3+} ions deposited at the 1st and the Dth layers of CaF_2.

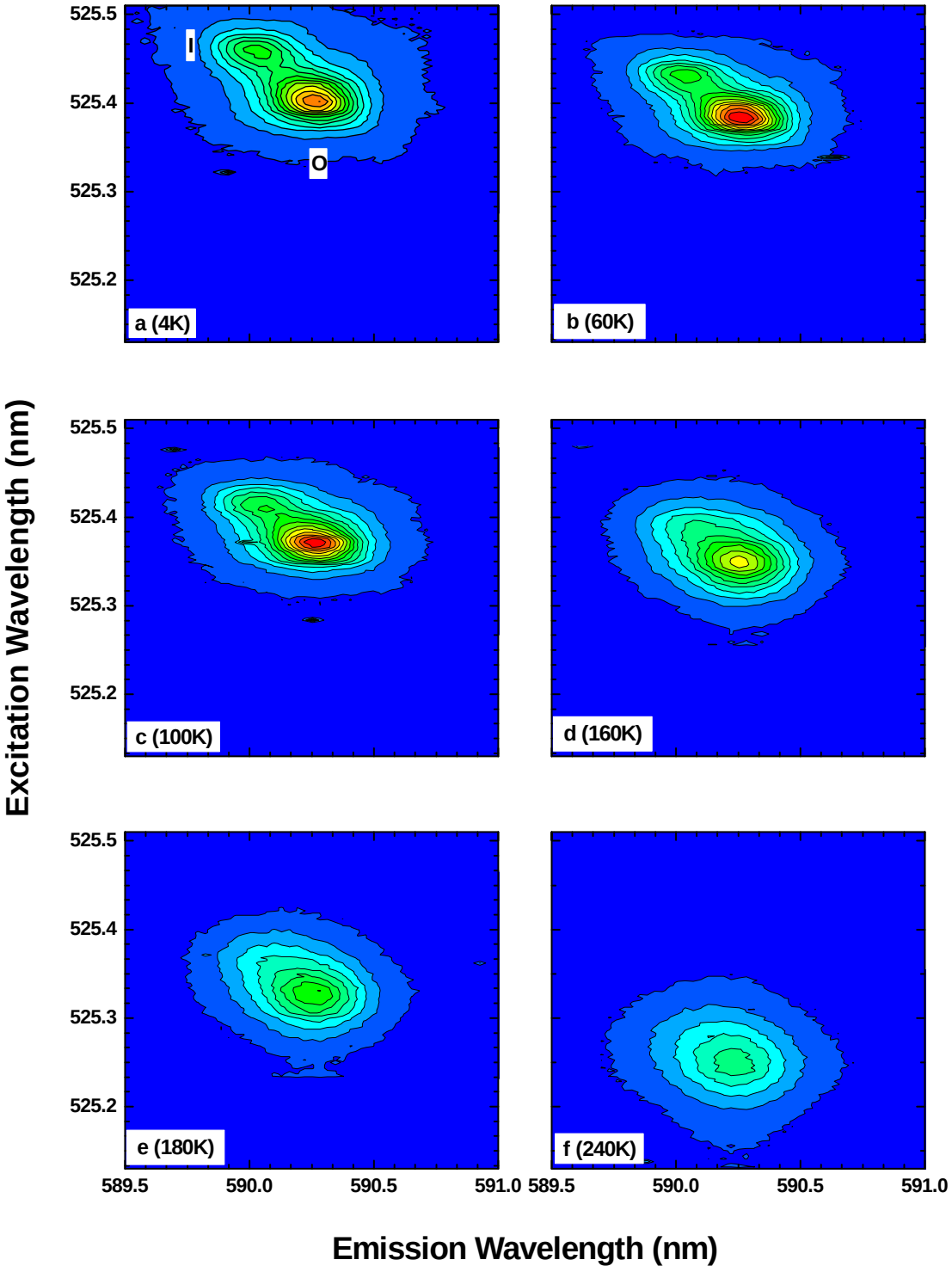

Fig 5.18. Contour plots for a 5ML symmetric SL (SL3172) at various temperatures; (a) 4 K, (b) 60 K, (c) 100 K, (d) 160 K, (e) 180 K and (f) 240 K.

The two centres are clearly distinguishable at low temperature. However the PL intensity of the I centre showed faster quenching, apparent from 100 K, than the cubic centre (fig. 5.18 (c)). The cubic centre remained detectable at 260 K and even up to room temperature while the I centre was completely quenched (fig 5.17(f)). It seemed that the PL intensity behaviour of the I centre was influenced by thermal excitation. When the same thermal relaxation, due to depopulation of the ground state, was considered for both centres the faster decreases of the I centre supports the idea of the delocalisation of the electrons. In other words, the electrons are freed from the bound state and the crystal field of the Eu^{3+} at the interface is somewhat restored to cubic. Consequently, this would cause the PL intensity of the I centre to decrease with raised temperatures. In addition the PL intensity of the O centre is then expected to be fed by the decrease of the I centre at higher temperature. Thus the decomposition of the I centre provided by the electron delocalisation model would lead to increase of the O centre.

Under this model the variation of the PL intensity of the I centre with respect to temperature, *T*, can be written as below

$$PL_I(T) \propto 2N\left\{1-\exp\left(\frac{-E_b}{k_B T}\right)\right\}R(T). \tag{5.3}$$

Here *N* is defined in (5.1) and k_B is Boltzmann's constant. A temperature relaxation term, *R(T)* is introduced accounting for depopulation of the ground state of Eu^{3+} due to thermal excitation. E_b is the binding energy of electron localised at the bottom of the CdF_2 conduction band and in the CaF_2 layers. The factor of 2 in (5.3) represents the portion of Eu^{3+} ions exposed to the electron-induced interaction (the 1st and the Dth layers in fig. 5.17) in trigonal symmetry. On the other hand, the PL increase of the O centre can be similarly written as below,

$$PL_O(T) \propto N\left\{(D-2)+2\exp\left(\frac{-E_b}{k_B T}\right)\right\}R(T), \tag{5.4}$$

where D is the thickness of the CaF_2 layers expressed in ML. The same amount of PL decay from the I centre is added to the PL intensity of the O centre. Assuming that the temperature relaxation term is the same for both centres and the N is uniform among the layers, one can express the PL intensity ratio of the O and the I centres with respect to temperature, T, as below,

$$\frac{PL_O}{PL_I} = \left\{ \frac{D}{2\left(1-\exp\left(-E_b / k_B T\right)\right)} \right\} - 1. \tag{5.5}$$

The binding energy can be found by plotting the PL ratio of the O and the I centre with respect to temperature. A similar analytical technique was used as that described in section 5.2.2 (fig. 5.14). The peak values were again obtained by performing two Gaussian fits using Igor Pro. The fitting result for a 5 ML thick SL (SL3172) is shown in fig. 5.19. During the evaluation, broadening was ignored as the integrated intensities ratios gave similar results as the PL intensity ratios at each temperature. Hence the peak values after fitting were considered for the model. The residuals of the fitting at the peak positions were taken as uncertainties in the PL intensities of each centre. In general, the fitting became very hard or impossible to perform at high temperatures with two Gaussian curves (T > 260 K). As a result, large uncertainties were obtained for the I centre at high temperatures.

Multi peak fittings were carried out for three SLs having different thicknesses; 3 ML, 5 ML and 7ML thick SLs. Subsequently the PL ratios of the O and the I centres were plotted against temperatures as shown in fig. 5.20. Theoretical fittings using (5.5) are also presented. In general, the electron delocalisation fittings and the experimental data agreed throughout the whole temperature region. For each calculation, D and E_b were varied in order to yield the minimum χ^2. The calculated value, D, for the 3 ML thick SL (SL3173) is 4.1 ML which is allowed by MBE technology limit. For the 5 ML (SL3172) and 7 ML (SL3178) thick SLs the parameter D values were (5.6 ± 0.3) ML and (5.2 ± 0.2) ML, respectively making them indistinguishable. Again these are allowed by MBE roughness. According to (5.2), the 5 ML and the 7 ML thick SLs are best described as equally thick

as their PL ratios are the same at 4 K. Alternatively non uniform thickness distribution might have caused this result which giving a similar PL ratios.

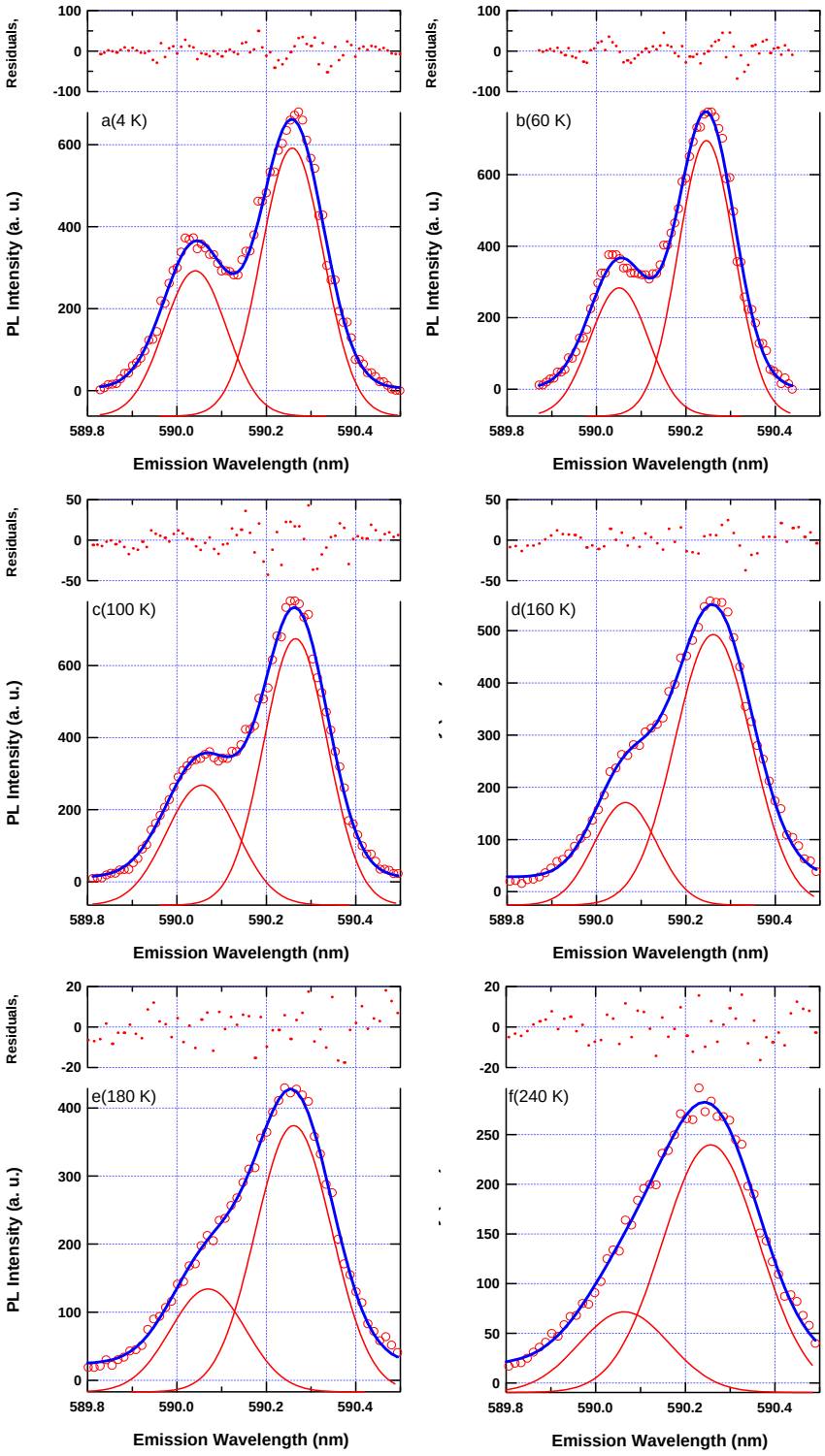

Fig. 5.19. Multi peak fitting of the I and the O centres of Eu^{3+} in a 5ML SL (SL3172) with various temperatures.

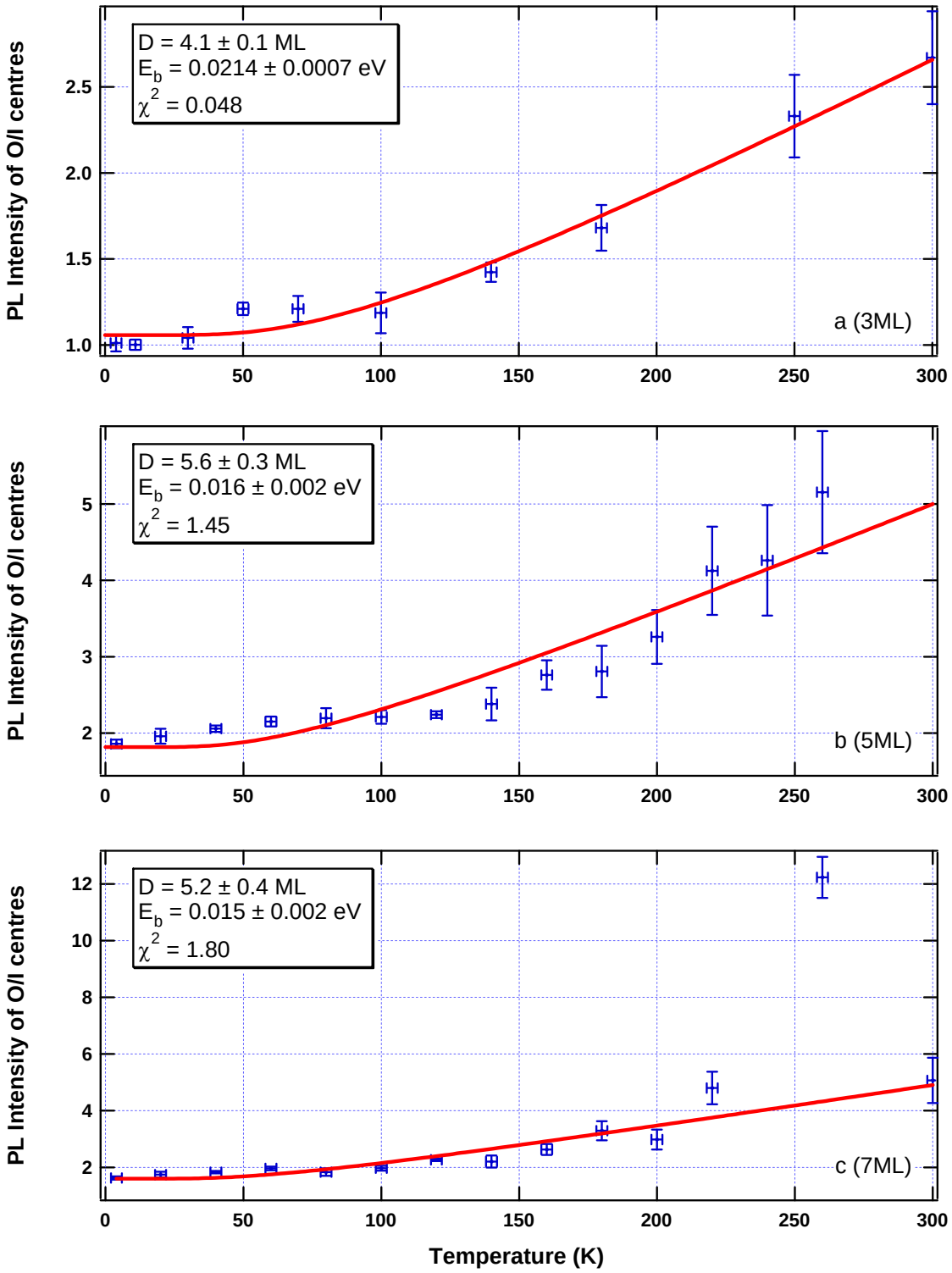

Fig. 5.20. Fitting of the electron delocalisation model to the experimental data. Three samples were used; (a) 3 ML thick SL, (b) 5ML thick SL and (c) 7 ML thick SL. Note that the data point at 260 K in (c) was ignored in calculation.

It is instructive to notice that the binding energies are not the same for all samples. For example the binding energy for trapped electrons in a CaF_2-CdF_2 SL that has a thickness of 3 ML is larger than that for 5 ML or 7 ML thickness. The calculated binding energy, E_b, for the 3 ML thick SL is (21.4± 0.7) meV. The binding energies for the 5 ML and the 7 ML thick SLs are given by (16 ± 2) meV and (15 ± 2)meV, respectively. This reflects that the binding energy for layers of similar thickness are the same however the binding energy becomes different as the thickness of layers varies. Note that the data point at 260 K for SL3178 (fig. 5.20 (c)) is ignored in calculation as it does not follow the trend. It was felt that a low signal to background ratio limited the multi peak fitting in this particular case.

The temperature dependence of Eu^{3+} PL in a 2 ML thick SL (SL1885) was also investigated. No direct evidence of an I → O centre transformation was observed to support the electron delocalisation model. However multi peak fitting was carried out since the weak shoulder, as shown previously (fig. 5.14 (e)), which thought to tbe the O centre, was detected in longer emission wavelength and shorter excitation wavelength from the I centre in CEES. Judging from previous multi peak fittings (fig. 5.19) the PL position of the O centre did not shift with temperature. Hence one of the Gaussian curves was fixed at the O centre emission wavelength during the multi peak fitting and some of the fittings are shown in fig. 5.21 for example. The thermal relaxation of the centres however limited the measure of peak intensity values at high temperatures. As a consequence peak values of the centres up to only 170 K were obtained.

Again equation (5.5) was applied to the results from the multi peak fitting for SL1885 as shown in fig. 5.21 (a). As a result, D is calculated as (2.37 ± 0.01) ML and the binding energy, E_b is calculated as (31 ± 1) meV. The binding energy is greater than that of the 3 ML thick SL. The calculated electron delocalisation model is also represented in fig. 5.22 for a comparison (b).

The binding energies for these SLs evidently show an inverse proportionality to the thickness of SLs. The binding energies, E_b and the layer thicknesses, D for the investigated SLs are summarised in table 5.2. It was suggested that possible size

confinement of the CaF_2-CdF_2 SL might have caused such increase in the binding energy with reducing thickness. Whether electrons are trapped in the conduction band of CdF_2 or trapped within the CaF_2 crystal, the binding energy is somewhat influenced by the physical size of the SLs.

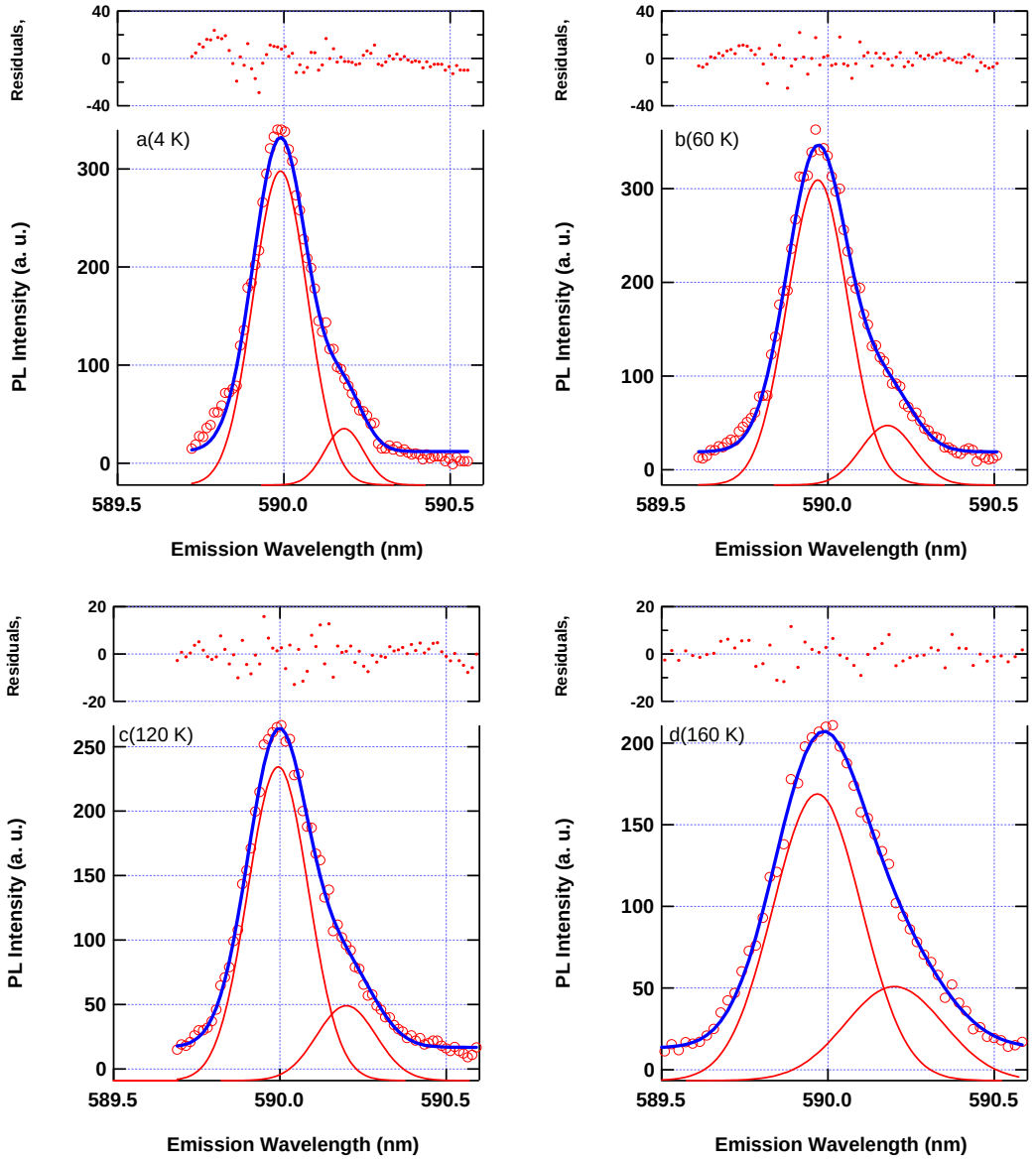

Fig. 5.21. Multi peak fitting results for the 2 ML thick SL (SL1885) with respect to temperature. Note that PL position of the O centre was fixed during the fitting process.

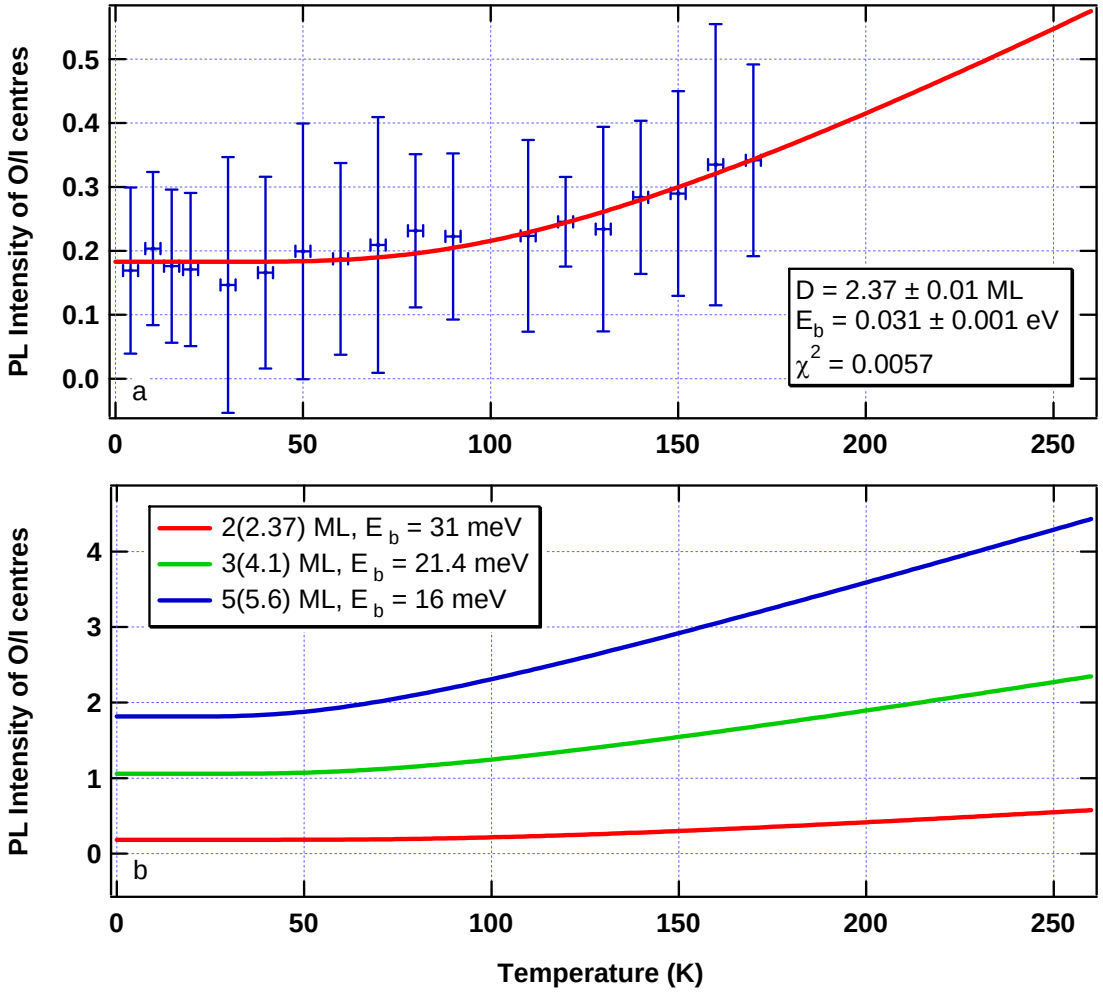

Fig. 5.22. (a) The PL intensity ratio of the O and the I centre of Eu^{3+} in a 2 ML thick SL (SL1885). The electron binding energy using (5.5) is displayed in the inset. (b) Calculated PL intensity ratios if the O and the I centres with respect to temperature. The values inside brackets are provided by calculation which gave the least χ^2 fit to the experimental data.

Table 5.2. Summary of thicknesses and binding energies of SLs using (5.5).

Superlattices	Normal thickness	Corrected thickness, D (ML)	Binding energy, E_b (meV)
SL3178	7	5.2 ± 0.4	15 ± 2
SL3172	5	5.6 ± 0.3	16 ± 2
SL3173	3	4.1 ± 0.1	21.4 ± 0.7
SL1885	2	2.37 ± 0.01	31 ± 1

There is still an unanswered question as to whether these binding energies are dependent on the thickness of CaF_2 layers or CdF_2 layers or even both. For that reason a growth of asymmetric SLs (ASLs) was proposed. For example, SLs of $(CaF_2:Eu)_2$-$(CdF_2)_4$ and $(CaF_2:Eu)_4$-$(CdF_2)_2$ will allow further investigation of binding energy with thicknesses. In either SL, for instance, the binding energy could reflect either a symmetric $(CaF_2:Eu)_2$-$(CdF_2)_2$ SL or a $(CaF_2:Eu)_4$-$(CdF_2)_4$ SL. This might not only reveal the nature of the binding energy, but also reveal the location of the charge compensating electrons with certainty. The electron delocalisation model is applied to ASLs and discussed in the following chapter.

5.2.4 PL behaviour of Eu^{3+} centres under additional UV excitation

Following the previous subsection, delocalisation of the charge-compensating electrons was investigated by means of optical excitation. The 325 nm line from a He-Cd laser was employed to excite SLs additionally on top of the dye laser excitation. Corresponding PL behaviour of the I and the O centres under additional UV excitation is reported here. As this was done at low temperature, the monitoring of peak intensities of the I and the O centres was easier with the thermal relaxation and broadening minimised. It was first confirmed that, in the absent of dye laser excitation, UV excitation did not directly excite of the Eu^{3+} centres. The effect of the UV laser was only evident when Eu^{3+} ions are simultaneously excited by the dye laser. In general, all SLs (except for the 2ML one) showed increase in PL intensity from the cubic centre and decrease from the interface centre, during UV excitation. Fig. 5.23 and 5.24 show the PL intensity behaviour of the I and the O centres in the 3 ML thick SL (SL3173) and their multi peak fittings, respectively. The dye laser and the UV laser were incident onto the same spot of the SL and CEES was performed three times; before UV, during UV and after UV excitation. In this particular SL, UV excitation caused a PL intensity decrease of 20% in the I centre from its initial state (fig. 5.24(a)). On the other hand, there was 38% increase for the O centre (fig. 5.24(b)). Upon ceasing UV excitation the PL intensities of the centres almost returned to their initial values (fig. 5.23(c)). It was observed that UV excitation does not destroy the I centre completely and the decrease of the I centre is not persistent.

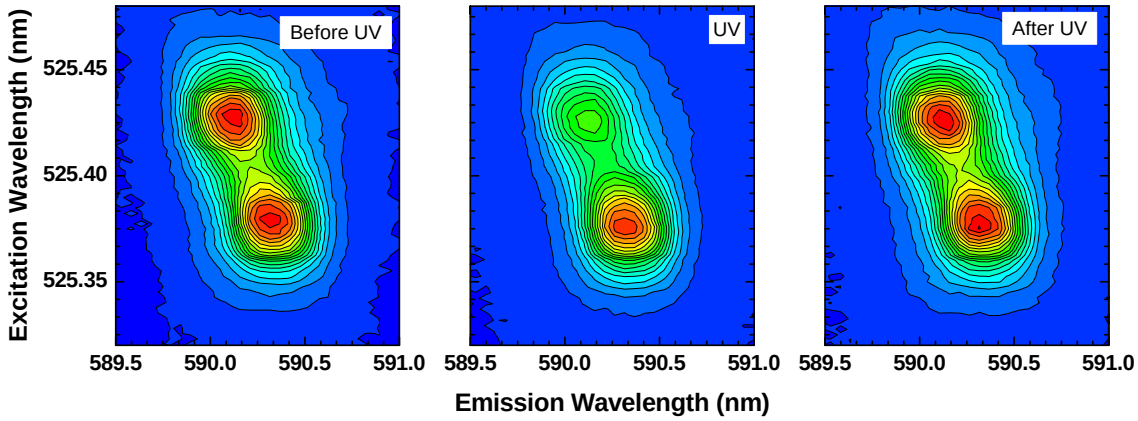

Fig. 5.23. Contour plots of the 3 ML thick SL (SL3173) before, during and after additional UV excitation on top of the $^7F_0 \rightarrow {}^5D_1$excitation and the $^5D_0 \rightarrow {}^7F_1$ emission at 4 K.

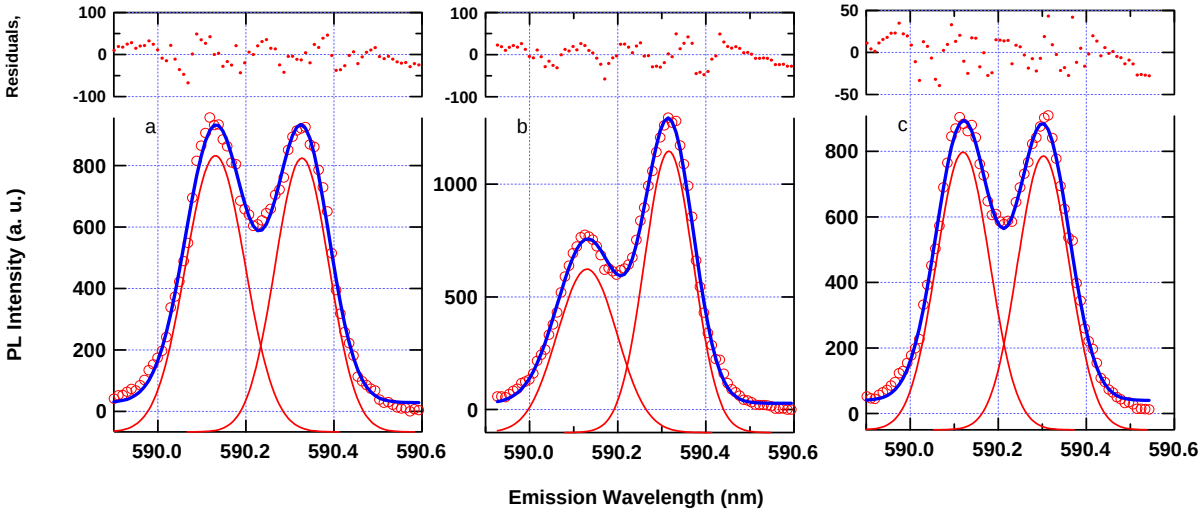

Fig. 5.24. Multi peak fitting of the I and the O centres in SL 3173; (a) before, (b) during and (c) after the UV excitation.

The time dependence effect of the UV excitation was studied by monitoring the peak PL intensity of each centre. The dye laser excitation was fixed at the I centre transition wavelength while UV excitation was controlled by a programmed shutter opened and closed sequentially. Once the monitoring was finished then the dye laser was tuned to the O centre transition, without moving the laser incident spot for either laser, and the monitoring continued using the same period for the mechanical shutter. The PL signals from each centre were selected by a SPEX 1700 spectrometer and were recorded by a PMT. Also the background was recorded to be subtracted from the raw data. Fig. 5.25

shows the observed monitoring of both centres in various SLs with respect to time of the UV exposure and recovery.

The successive monitoring of the I and the O centres in various SLs under additional UV excitation showed a very rapid PL intensity change when UV was incident onto SLs however upon stopping the UV excitation, PL behaviour was time dependent. For example, the PL intensity increase of the O centre in a 7 ML thick SL (SL3178) on UV excitation was almost step-like whereas the PL decrease of the same centre after UV excitation was stopped was best described as an exponential decay (fig. 5.25(a)). Similarly for the I centre the PL decrease immediately after UV excitation was almost a step function. However the recovery of PL intensity of the I centre was a rather slow process. It was also observed that the PL behaviour, for all investigated SLs, was repeated many times until gradual decrease of the PL signal due to the dye laser drift occurred. One can see clearly that the decrease of the I centre does not lead to 1:1 increase of the O centre provided by UV excitation. In addition the amount of PL decrease when the UV excitation was turned on was different in all SLs. It was observed that the PL decrease was smaller for thinner SLs.

In chapter 4 it was initially suggested that PL increase of the O centre is due to transformation of Eu^{2+} in a cubic centre into Eu^{3+} in that centre by an ionisation process. The above SLs, however, did not show any Eu^{2+} PL and hence no such decay of Eu^{2+} emission under UV excitation was observed. Yet increase of Eu^{3+} PL intensity in thin SLs under UV excitation was observed. Clearly the increase of the O centre is not fed by a decrease of divalent Eu. It is rather due to decrease of the I centre concentration. Fig. 5.25 evidently shows that the PL responses for both centres are repeatable. For instance, when PL of the O centre increases, that of the I centre decreases. Alternatively, when the O centre recovers its original intensity the I centre also recovers. However this is not the case for the Eu^{2+} and Eu^{3+} problem. The PL intensity of Eu^{2+} does not recover to its initial value (see fig. 4.17) while Eu^{3+} repeated in the pattern shown in fig. 5.25. Hence the PL behaviour of Eu^{3+} upon UV excitation discussed in chapter 4 is not related to a $Eu^{2+} \rightarrow Eu^{3+}$ transformation.

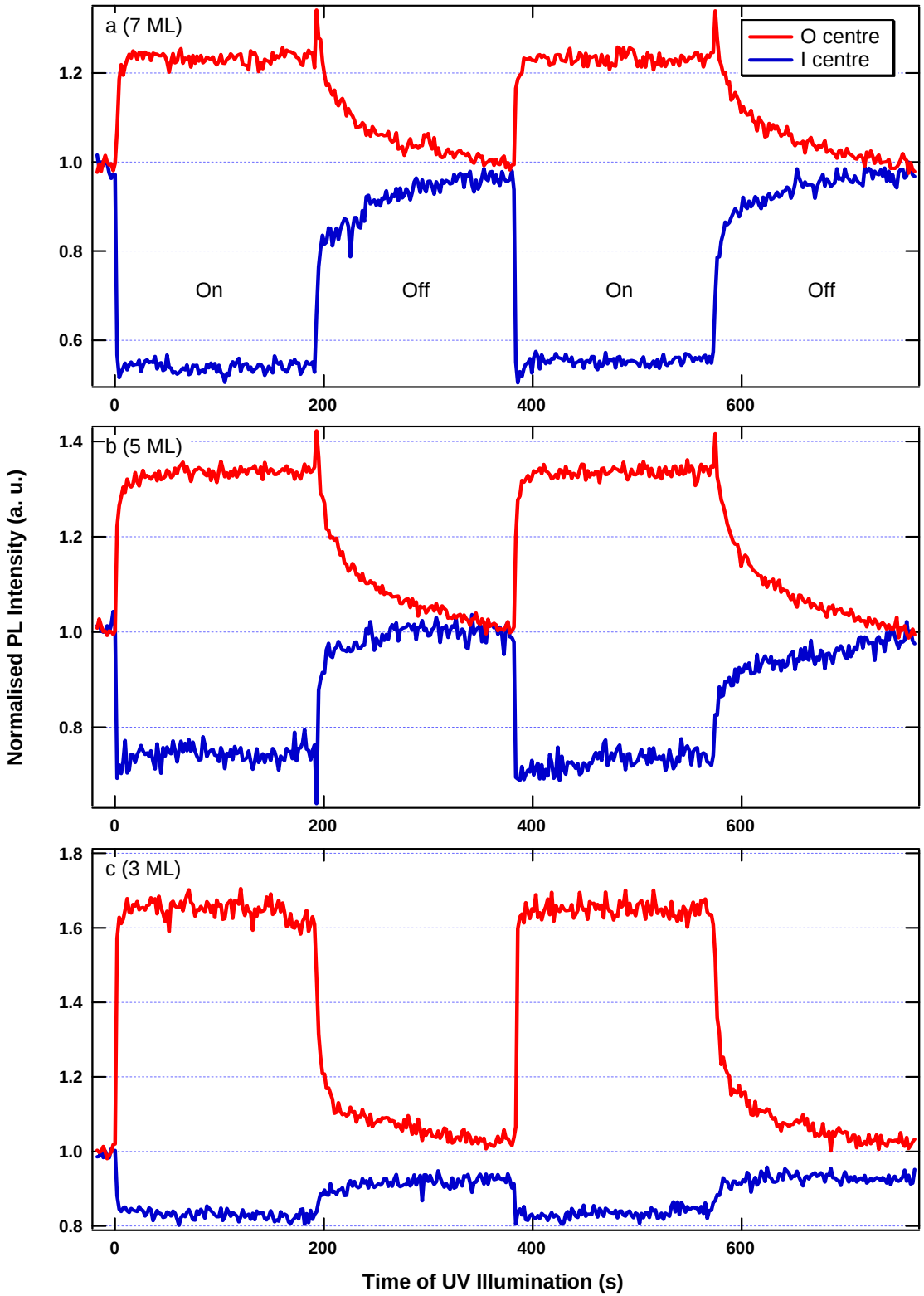

Fig. 5.25. The PL intensity monitoring of the I and the O centres in (a) 7 ML thick SL, (b) 5 ML thick SL and (c) 3 ML SL under the influence of additional UV excitation. Peak intensities were recorded by a PMT.

In general, assuming the thicknesses of the investigated SLs are correct, the amount of PL increase of the O centre is inversely proportional to the thickness of SLs. However this was the opposite for the I centre. In other words the thinner the SL the larger the PL increase of the O centre, but the smaller the PL decrease for the I centre.

Recalling equation (5.1) explains why the PL decrease of the I centre does not lead to 1:1 increase of the O centre during the UV excitation. The PL intensity of the I centre is proportional to *2N* while the PL intensity of the O centre is proportional to *(D-2)N* where *D* is the layer thickness as defined earlier. Only if *2N = (D-2)N* can one expect 1:1 PL behaviour, with initially equal concentrations of the O and the I centres.

Incorporating the previous proposal that electron binding energy is inversely proportional to thicknesses of SLs, the change in PL intensity under UV excitation can be explained in terms of thickness. Again, using (5.1), the PL intensity of the I centre before the UV excitation, $t = 0$, can be written as $PL_I \propto 2N$. Let us consider a coefficient, *A*, that describes the fractional PL decrease of the I centre provided by the UV excitation. The coefficient *A* is assumed to be thickness dependent. In practice *A* is measured to be 0.460, 0.256, 0.170, respectively for the 7 ML, 5 ML and 3 ML thick SLs from normalised PL decrease (fig. 5.25). Following the above trend one might expect a complete quenching ($A = 1$) of the I centre for thick SLs and change ($A = 0$) at all for thin SLs.

For $t > 0$, after the UV excitation is initiated, the PL intensity decrease of the I centre and its normalised PL intensity can now be written respectively as,

$$PL_I \propto 2N - 2NA, \quad (0 \le A \ge 1),$$
$$PL_I = 1 - A. \tag{5.6}$$

Similarly for the O centre the PL intensity as well as its normalised intensity increased by UV excitation can be written as below,

$$PL_O \propto (D-2)N + 2NA,$$

$$PL_O = \frac{\left((D-2)+2A\right)}{(D-2)}. \tag{5.7}$$

The normalised PL intensity of the O centre is obtained by dividing the first equation by the initial PL intensity of the O centre, $PL_O \propto (D\text{-}2)N$. Following the electron delocalisation model, the additional UV effectively delocalises electrons within the CaF_2-CdF_2 system. Given that delocalisation, a decrease of PL intensity of the I centre results as the trigonal symmetry no longer holds and therefore transforms to the O centre. One can see that the decrease in (5.6) is added in (5.7) reflecting transformation of the I centre to the O centre. Finally the ratio of the normalised PL intensities of the O and the I centre is written as below,

$$\frac{PL_O}{PL_I} = \frac{\left((D-2)+2A\right)}{(D-2)(1-A)}. \tag{5.8}$$

Taking the experimental observation of PL decrease coefficient A into a linear relationship with thickness of CaF_2, D, then A can be expressed as,

$$A = bD. \tag{5.9}$$

The proportionality constant b was found to be (0.060 ± 0.005) ML^{-1} by performing a linear fit as shown in fig. 5.26. In fact the upper limit of A should be 1 when $D \rightarrow \infty$. However within the three data points it was roughly taken as directly proportional to the thickness ranging between 2 ML and 10 ML. The nature of equation (5.8) prohibits inclusion of PL behaviour of the 2 ML thick SL (SL1885) since an infinite value of PL intensity ratio would occur as D reaches 2.

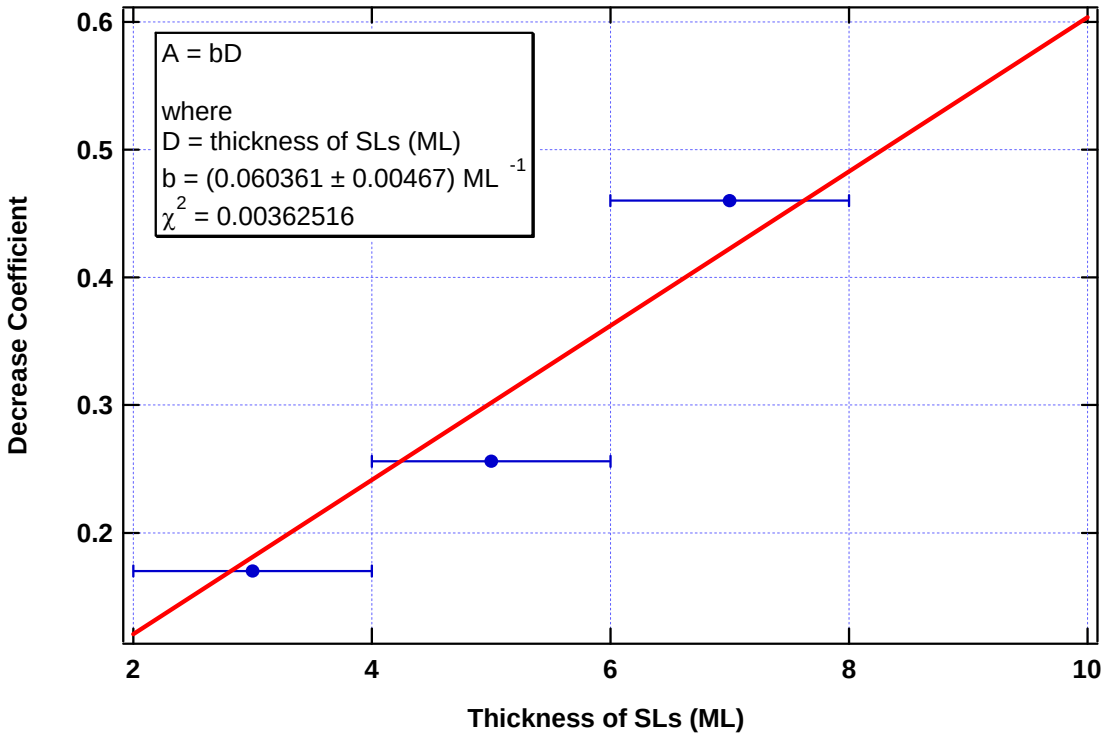

Fig. 5.26. Linear fitting of decrease coefficient A with thickness D of SLs. Inset shows the fitting results.

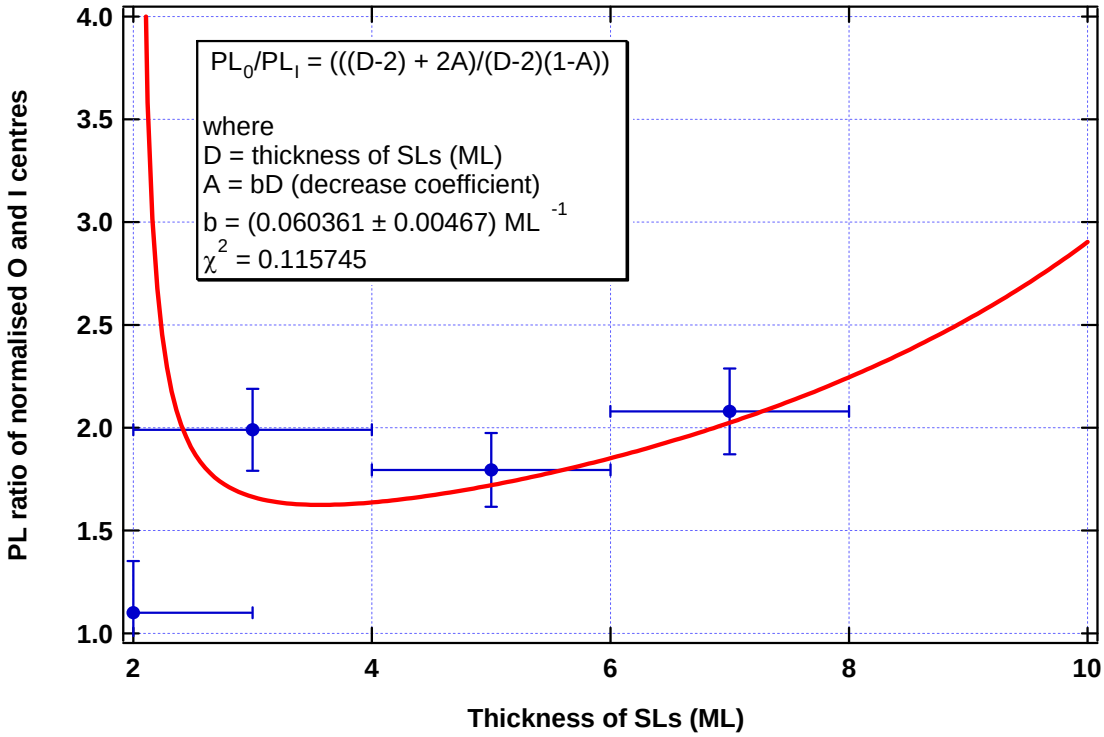

Fig. 5.27. PL ratio of normalised intensity of the O and the I centres during He-Cd laser excitation on top of the $^7F_0 \rightarrow {}^5D_1$ excitation and the $^5D_0 \rightarrow {}^7F_1$ emission of Eu^{3+}. Note that experimental result for 2 ML SL is also presented.

Now the normalised PL ratio can be readily expressed in terms of thickness *D* by substituting (5.9) into (5.8) and the function shows good agreement with the experimental data as shown in fig. 5.27.

It is important to consider the PL intensity changes for the I and the O centres in a 2 ML thick SL. The normalised PL ratio influenced by additional UV excitation for the 2 ML SL is also presented in the graph. The experimental value of normalised PL ratio for the SL is $PL_O/PL_I = 1.1 \pm 0.4 \left(= \left(\frac{PL_O/PL_I\,(t>0)}{PL_O/PL_I\,(t=0)} \right) \right)$ given by multi peak fittings as shown in fig. 5.28. Some influence of the UV excitation was observed (possibly 10% increase) however it does not make difference between the initial PL ratio within the limits of uncertainty. Although there is a $\pm$ 1 ML of MBE roughness there is a discrepancy raised from the SL. Also taking 2.37 ML as the corrected thickness for the 2 ML SL observed from the previous subsection, this sample did not follow the model. The additional UV excitation did not significantly influence PL behaviour of the I and the O centres in the 2 ML thick SL (SL1885).

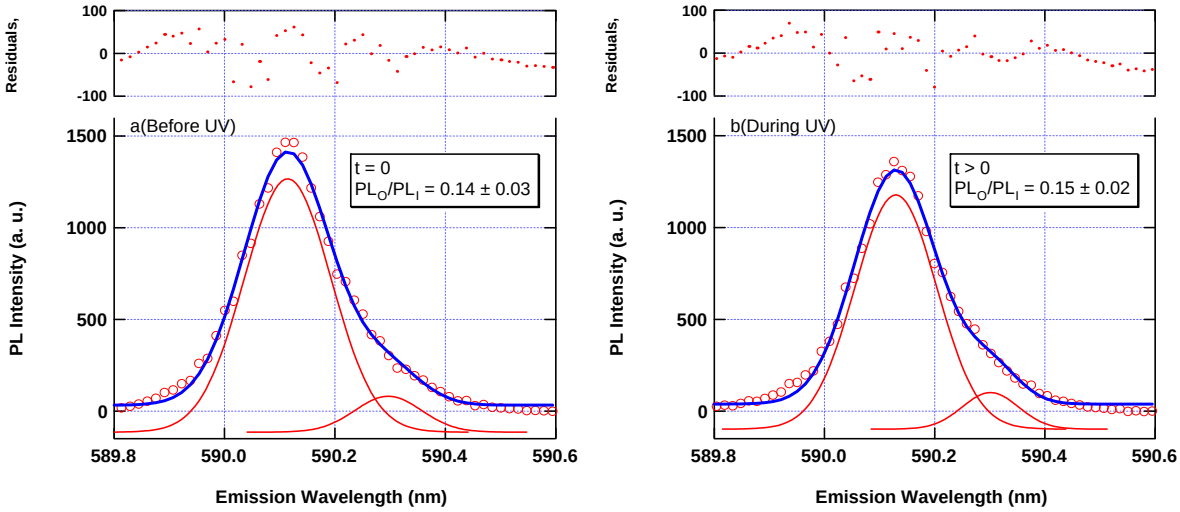

Fig. 5.28. PL behaviour of the I and the O centre of Eu^{3+} in a 2 ML thick SL (SL1885); (a) before UV excitation and (b) during UV excitation.

It has been suggested that the binding energy of electrons in a trap in CaF_2 or at the bottom of conduction band of CdF_2 is significantly altered in a 2 ML [16]. The binding energy does not seem to be inversely proportional to the thickness of SLs. For that reason

equation (5.8) possibly no longer holds for the 2 ML SL and hence no decrease in PL contributes to the growth of the O centre. Furthermore the growth of asymmetric SLs (ASL) is proposed to modify the binding energy of the electron in 2 ML thick SLs. It is expected that for a $(CaF_2:Eu)_2$-$(CdF_2)_4$ ASL, for example, that the transformation of the I centre to the O centre is possible if the charge compensating electron is in the CdF_2 layers. However if electrons are in the CaF_2 layers, then the PL behaviour of the I centre is expected to be the same as for the symmetric 2 ML SL.

5.3 Crystal field analysis

The energy levels of the O centre were calculated and compared to those of a CaF_2:Eu bulk crystal in this section. As described in chapter two, the crystal field parameters were added to the free ion Hamiltonian as a perturbation. We used an empirical programme, 'f-shell' [17]. An Eu^{3+} ion, which is a f^6 ion, has 3003 possible electronic states (14!/6!(14-6)!). However the entire f^6 configuration has been truncated to the lowest 40 multiplets as an approximation. For the bulk crystal field analysis, the results from Jouart *et al*. [2] were used and for the SLs (3 ML thick) the previous results were used [5]. The calculated energy levels and the estimated crystal field parameters are presented in table 5.3 and 5.4, respectively.

As a result, the energy level fitting gave the standard deviation values of σ = 16 cm^{-1} and σ = 13 cm^{-1}, respectively for the crystal and SLs. The B_c^4 and B_c^6 parameters for the cubic centre of SLs were increased from that of CaF_2:Eu crystal by 37 cm^{-1} and 58 cm^{-1}, respectively. However the changes in the parameters are well within the limits of uncertainties given by the calculation. It can be shown that similar fitting results are obtained when the individual parameters are varied as shown in fig. 5.29.

Table 5.3. Calculated energy levels of Eu^{3+} in cubic symmetry in a CaF_2 crystal and in CaF_2-CdF_2 SLs (cm^{-1} in air)

Multiplet	State and symmetry	O centre in CaF_2		O centre in SL	
		Calc.	Expt*.	Calc.	Expt.
$^7F_0$	A_{1g}	-1	0	3	0
$^7F_1$	T_{1g}	350	339	354	345
$^7F_2$	T_{2g}	800	812	805	815
	E_g	1326	1339	1330	1347
$^7F_3$	T_{1g}	1857	1855.5	1857	1861
	T_{2g}	1980	1968	1978	1968
$^7F_4$	T_{1g}	2884	2884	2896	2892
$^5D_0$	A_{1g}	17279	17275.5	17281	17281
$^5D_1$	T_{1g}	19024	19030	19031	19031
$^5D_2$	T_{2g}	21450	21428	21462	-
	E_g	21518	21538	21578	-

*The energy levels are obtained from Jouart *et al.* [2].

Table 5.4. Crystal field parameters estimated from f-shell programme (cm^{-1}).

Parameters	CaF_2:Eu^{3+} Crystal	CaF_2:Eu^{3+}-CdF_2 Superlattice
F_{tot}	87012.81	86929.09
α	20.16	20.16
β	-566.0	-566.0
γ	1500	1500
T^2	300	300
T^3	40	40
T^4	60	60
T^6	-300	-300
T^7	370	370
T^8	320	320
M_{tot}	2.1	2.1
ζ	1327.40	1328.80
B_c^4	-2010 $\pm$ 80	-1980 $\pm$ 70
B_c^6	900 $\pm$ 100	910 $\pm$ 90
σ	16	13

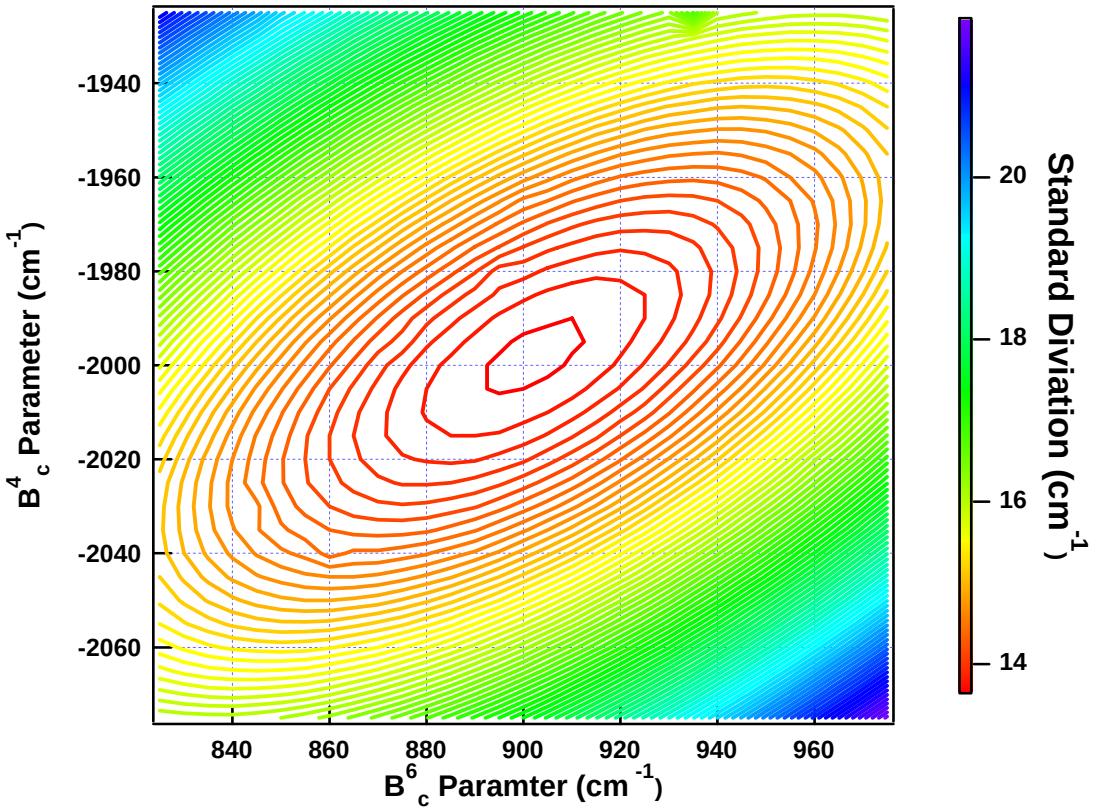

Fig. 5.29. Cubic parameter mapping of the energy level calculations. The height of the contour represents the standard deviations of the fitted results of the energy levels of Eu^{3+} in SLs.

We interpret the slight shift of the crystal field parameters as primarily due to the deformation of the crystal structure taking place in SLs. Another set of calculations were carried out to further the cubic crystal field analysis. As proposed in section 5.2, a distortion of the cubic symmetry as measured by XRD [10] was employed. Initially a cube in which the z axis is oriented along a [111] direction was considered. Due to the compressive planar strain for the 20 ML thick SL as discussed in the previous chapter, the entire cube is also compressed, for instance, along the [111] axis. However when the fluorine ions along the [111] axis are relatively less compressed than the other in-plane fluorine ions, then the cubic symmetry is reduced to three fold symmetry which results in the introduction of a B_c^2 parameter along with other parameters due to the change of the principal z axis. In the calculation of the parameters, based on a point charge model, also provided by the author of the 'f-shell' programme, a relatively larger distance (0.3%) of each fluorine ion that is in the [111] direction yielded the B_c^2 = -38cm^{-1} (otherwise zero

for a non distorted cube). It can be shown that the introduction of the B_c^2 parameter results in splitting of energy levels of Eu^{3+} centres. The magnitude of the parameter determines the degree of splitting and the sign of the parameter reflects the assignment of doublet and singlet, for example, for $J = 1$ multiplets the position of the doublet relative to the singlet is dependent on the sign of the parameter. The splittings of the cubic centre in thick SLs are considered here incorporating the distortion of the crystal structure. In section 5.2, the splittings of the cubic centre in thick SLs were found as 1.38 cm^{-1} and 6.4 cm^{-1}, respectively for the $^5D_1$ and the $^7F_1$ multiplets. Due to the distortion, the degeneracy of each multiplet breaks into a doublet (E_g) and a singlet (A_{2g}). The splittings of the multiplets are schematically shown in fig. 5.30. The B_c^2 parameter is added in the energy level calculations along with the appropriate C_{3v} symmetry crystal field parameters.

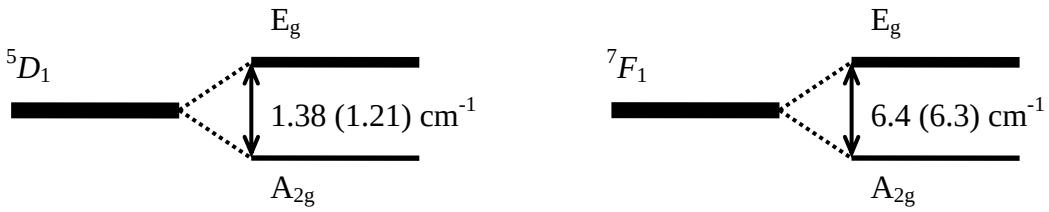

Fig. 5.30. The observed splitting of the cubic centre of Eu^{3+} in thick SLs (SL1649). The $^5D_1$ and the $^7F_1$ are both split into two levels separated by 1.38 cm^{-1} and 6.4 cm^{-1}, respectively. Inside the brackets are the calculated values.

Table 5.5. Crystal field parameters of the distorted cubic centre (C_{3v}).

Parameters (cm^{-1})	
B_c^2	-33
B_c^4	-820
B_a^4	2000
B_c^6	50
$B_{a'}^6$	510
B_a^6	870

As a result, the crystal field parameters governed by the distortion of the crystal structure gave the energy levels of the split cubic centre with $\sigma = 76$ cm^{-1}. With the C_{3v} parameters the splitting of the $^5D_1$ and the $^7F_1$ levels were accurately determined as 1.21 cm^{-1} and 6.3 cm^{-1}, respectively. However, as indicated by the increased value of the σ, the energy levels are less accurately predicted than previous calculation where no splitting is considered. The parameters used in these calculations are summarised in table 5.5.

As mentioned in chapter 4 the PL behaviour of the lanthanoids can reflect the local environment of the host effectively. The origin of the splitting of the cubic centre can be described as a distortion of the crystal due to the strain in SLs. The strain is possibly accumulated for thick SLs as no splitting is observed in thin SLs confirmed by polarisation anisotropy. A crystal field analysis was also carried out for the I centre. A set of crystal field parameters is obtained by using the already evaluated parameters as well as taking an extra electron along the z [111] axis. The calculated results for the I centre are discussed in chapter 7.

5.4 Summary

We have demonstrated a monolayer resolution spectroscopy of the Eu^{3+} centres in CaF_2:Eu-CdF_2 SLs. The Eu^{3+} centres in SLs are clearly influenced by the layer thickness. The novel interface centre is only observed from thin SLs and became dominant in 2 ML thick SL. It has been shown that the PL intensity ratio of the O and the I centres is quantised by the layer thickness for perfectly grown SLs. In connection with the PL bleaching of the Eu^{2+}, the PL behaviour of the I and the O centres was related to the possible transfer of electrons. Hence the nature of the I centre is the electron-charge compensated centre and the possible transformation to the O centre is expected upon the delocalisation of electron. In this chapter both thermal and the UV excitations were used to demonstrate the delocalisation. The PL ratios of the centres were significantly altered by the additional excitations. However not all SLs have shown a uniform transformation, suggesting different trapping energies for different thicknesses, with a 2 ML SL demonstrating the highest trapping energy.

The polarisation anisotropy revealed the symmetry of the I centre as C_{3V} in which the charge compensation was along the [111] direction. The O centre was confirmed as cubic centre as no further splittings were observed. However for thick SLs the O centre is split by a small degree and in the opposite sense to the I centre split. A crystal distortion was considered to produce the splitting of the O centre. A crystal field analysis supports that the crystal is slightly less compressed along the [111] direction as a result of strain associated with SLs.

The electron charge compensator is assumed to be localised in either CaF_2 or CdF_2. Since the trapping energies are somewhat thickness dependent, the growth of the asymmetric SLs (ASLs) are proposed. CEES investigation of ASLs is expected to demonstrate clear understanding of localised electrons and the exact position of the localisation. CEES of the ASLs is discussed in chapter 6.

References

[1] R. J. Hamers, J. W. Wietfeldt, J. C. Wright, "Defect chemistry in CaF_2:Eu^{3+}," *J. Chem. Phys.*, vol. 77 pp. 683-691, 1982.

[2] J. P. Jouart, M. Bouffard, G. Klein G. Mary, "Cubic Eu^{3+} centres in fluorite-type crystals," *J. Lum.*, vol. 50, pp. 273-277, 1991.

[3] K. M. Cirillo-Penn, J. C. Wright, "Laser spectroscopic measurement of point-defect dynamics in Eu^{3+}:CaF_2," *Phys. Rev. B*, vol. 41, pp. 10799-10807, 1990.

[4] L. R. Olsen, A. O. Wright, J. C. Wright, "Localized fluorite diffusion and equilibrium in CaF_2:Eu^{3+} using site-selective spectroscopy and high-pressure techniques " *Phys. Rev. B*, vol. 53, pp. 14135-14144, 1996.

[5] J. K. Choi, "Laser spectroscopy of Eu^{3+} ions in CaF_2/CdF_2 Super-lattices," in *M. Sc. Thesis*. Christchurch: University of Canterbury, 2004.

[6] J.-P. R. Wells, "Laser spectroscopy of Alkaline earth fluoride crystals doped with trivalent Samarium and Europium Ions," in *Ph. D. Thesis*. Christchurch: University of Canterbury, 1996, pp. 477.

[7] B. Henderson, R. H. Bartram, *Crystal-Field Engineering of Solid-state Laser Materials*: Cambridge University Press, 2000.

[8] R. J. Reeves, J. K. Choi, S. V. Gastev, A. V. Krupin, K. R. Hoffman, N. S. Sokolov, "Laser spectroscopy of Eu^{3+} centers in CaF_2:Eu–CdF_2 superlattices," *J. All. Com.*, vol. 451, pp. 84-87, 2008.

[9] J. D. Kingsley, J. S. Prener, "Free Charge Carrier Effect in Cadmium fluoride," *Phys. Rev. Lett.*, vol. 8, pp. 315-316, 1962.

[10] V. A. Chernyshev, A. V. Abrosimov, S. V. Gastev, A. V. Krupin, A. E. Nikiforov, J. K. Choi, R. J. Reeves, S. M. Suturin, N. S. Sokolov, "Energy structure of Eu^{3+} centres in CdF_2–CaF_2:Eu superlattices on silicon," *J. Phys.: Condens. Matter*, vol. 19, pp. 395023, 2007.

[11] V. Chakarian, T. D. Durbin, P. R. Varekamp, J. A. Yarmoff, "Formation of surface F centres on CaF_2/Si(111)," *Phys. Rev. B*, vol. 48, pp. 18332-18335, 1993.

[12] A. Izumi, K. Tsutsui, N. S. Sokolov, N. N. Faleev, S. V. Gastev, S. V. Novikov, N. L. Yakovlev, "High-quality CdF_2 layer growth on CaF_2/Si(111) " *J. Crystal Growth*, vol. 150, 1995.

[13] S. M. Suturin, S. A. Basun, S. V. Gastev, J. M. Langer, R. S. Meltzer, N. S. Sokolov, "Optical detection of electron transfer through interfaces in CaF_2:Eu-CdF_2 SLs," *Appl. Surf. Sci.*, vol. 162-163, pp. 474-478, 2000.

[14] N. S. Sokolov, S. V. Gastev, A. Y. Khilko, S. M. Suturin, I. N. Yassievich, J. M. Langer, A. Kozanecki, "Tunneling-assisted autoionization of the localized impurities in nanostructures," *Phys. Rev. B*, vol. 59, pp. R2525-R2528, 1999.

[15] S. V. Gastev, J. C. Alvarez, V. V. Vitvinski, N. S. Sokolov, A. Y. Khilko, "Bleaching Effects in Photoluminescence of Rare Earth ions in fluoride heterostructures," *Proc. SPIE*, vol. 2706, pp. 67, 1996.

[16] S. V. Gastev, *Private communication*. Ioffe Institute, Russia.

[17] M. F. Reid. University of Canterbury, New Zealand.

Chapter 6

Spectroscopy of trivalent Eu centres in asymmetric CaF_2:Eu-CdF_2 superlattices

6.1. Introduction

This chapter surveys laser spectroscopy of the Eu^{3+} centres in asymmetric SLs. It is of interest to consider whether the PL behaviour of the cubic and interface centres in asymmetric SLs are similar or different to that of the Eu^{3+} centres in symmetric SLs. The growth of the asymmetric SLs, henceforth ASLs, involves depositions of *m* mono layers (MLs) of CaF_2 and *n* MLs of CdF_2 where $m \neq n$.

The previous observations, as discussed in chapter 5, showed that the PL behaviour of the I and the O centres was influenced by the thickness of the host SLs and by external contributions such as thermal and UV excitation. For example, the I centre observed in the 2 ML thick SL was hardly influenced by additional UV excitation whereas the same centre observed in the thicker SLs was clearly influenced by the UV excitation. This puzzling behaviour of the I centre suggested that the electron binding energy is significantly altered for the 2 ML thick SL. However it is yet to be determined which material is responsible for such alteration. The symmetric SLs have limited ability to separate the CaF_2 and CdF_2 layers in terms of electron confinement.

Hence this chapter closely monitors the PL behaviour of the I and the O centres as to whether it follows the PL behaviour for equivalent thickness of the CaF_2 or CdF_2 layers.

Furthermore the location of the charge compensating electrons responsible for the formation of the I centre will be established with more confidence. Following a similar format to chapter 5, this chapter discusses the temperature dependence and the effect of additional UV excitation on the PL behaviour of the I and the O centres. The previous models are also tested for the ASLs and compared with the symmetric SLs.

6.2. Discussion of CEES results of Eu^{3+} centres in asymmetric superlattices

Two ASLs were mainly investigated and their CEES results are discussed in this section. These ASLs were $(CaF_2{:}Eu)_2$-$(CdF_2)_4$ and $(CaF_2{:}Eu)_4$-$(CdF_2)_2$ where the subscript represent thickness of the layers expressed in ML. The first ASL (ASL1982) gave an identical CEES result as the symmetric $(CaF_2{:}Eu)_2$-$(CdF_2)_2$ SL described in the earlier chapter. Again the I centre was the dominant peak and the O centre was observed as a weak shoulder, as shown in fig. 6.1(a). For the other ASL, which is [$(CaF_2{:}Eu)_4$-$(CdF_2)_2$], both centres were observed with comparable PL intensity and the pattern of the peaks was identical to the symmetric SLs as shown in fig. 6.1(b). The transition wavelengths for the ASLs and the symmetric SLs were in agreement.

It is clear that the Eu^{3+} centres in ASLs appeared to be the same as in the symmetric SLs. That is, the observed PL transitions for the I and the O centres between two hosts, symmetric SLs and ASL, are determined by the thickness of the CaF_2 layers regardless of the thickness of CdF_2. Recalling equation (5.2), the PL ratio between the O and the I centres was written in terms of the thickness of the host SLs, *D*, as follows

$$\frac{PL_O}{PL_I} = \frac{(D-2)C}{2} + B, \quad (2 \le D < \infty).$$

where *C* and *B* are as defined in chapter 5. *D* is considered as the thickness of CaF_2 layers here. It can be shown that the PL intensity ratio between the O and the I centres in ASLs also follows the above relation.

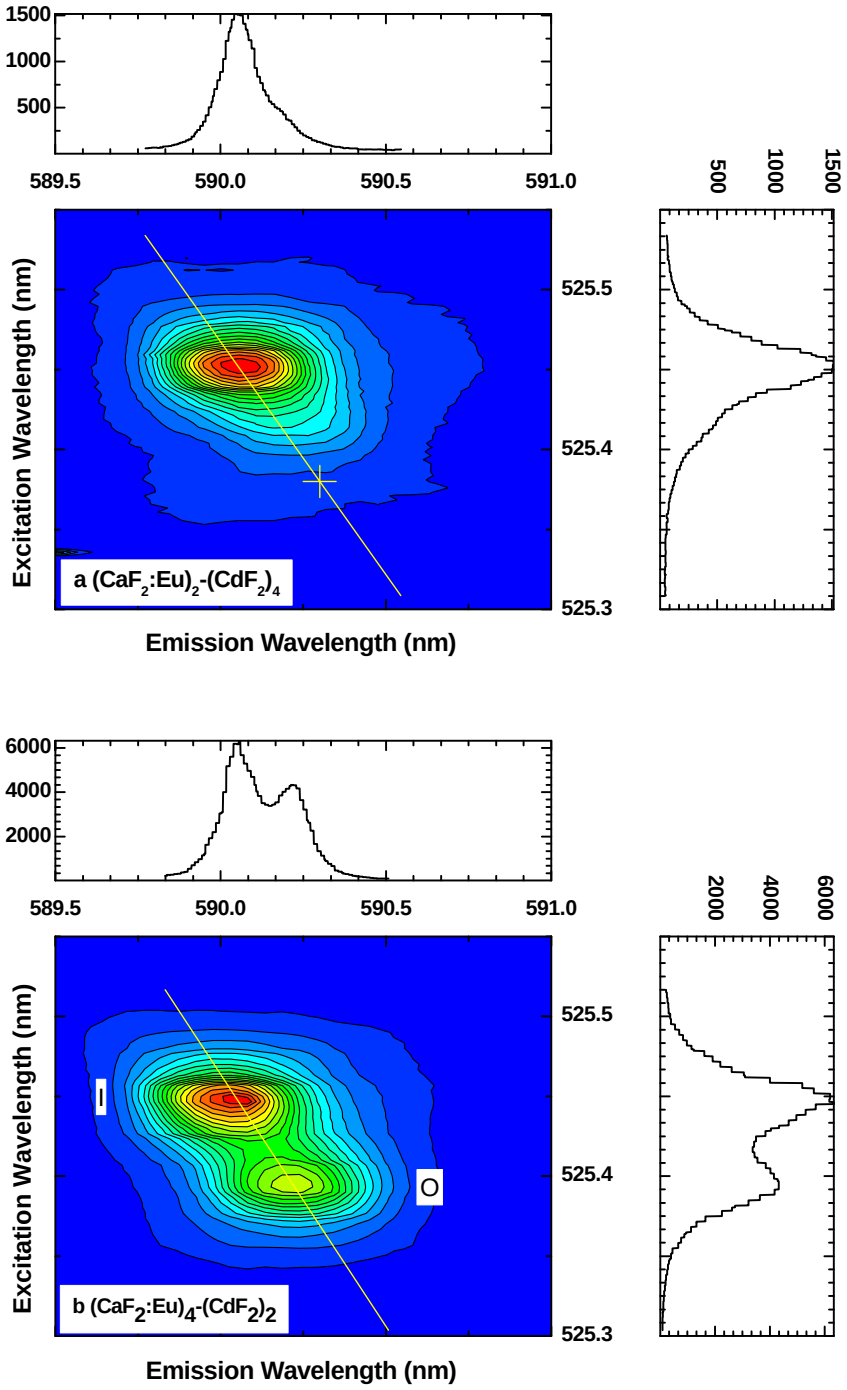

Fig. 6.1. Profile of the I and the O centre PL intensity for (a) ASL1982 $(CaF_2:Eu)_2$-$(CdF_2)_4$ and (b) ASL1980 $(CaF_2:Eu)_4$-$(CdF_2)_2$ at ~4 K. Note the cross mark in (a) represents the expected transition wavelengths of the O centre.

The PL ratios were obtained following the same analytical technique as that described in chapter 5. The data matrix elements profiling both centres (fig. 6.1) are selected from the raw data and re-plotted as shown in fig. 6.2. Two Gaussian curves, representing the I and the O centres, are used to fit the emission profile of the CEES of the centres. The PL intensity ratio of the centres, after the fitting, are given by 0.21 and 0.71, respectively for the ASL [$(CaF_2:Eu)_2$-$(CdF_2)_4$] and ASL 1980 [$(CaF_2:Eu)_4$-$(CdF_2)_2$].

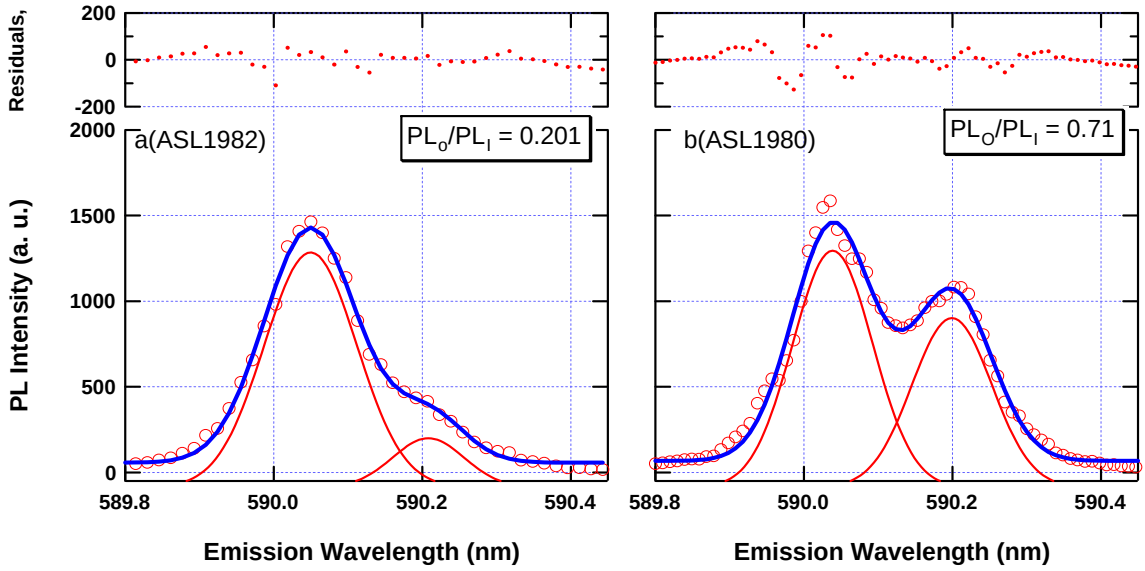

Fig. 6.2. Emission profile of ASLs, (a) ASL 1982 $(CaF_2:Eu)_2$-$(CdF_2)_4$ and (b) ASL1980 $(CaF_2:Eu)_4$-$(CdF_2)_2$. The PL intensity ratio (PL_0/PL_I) is given by 0.201 and 0.71, respectively, for ASL1982 and ASL1980.

As a result, the calculated PL intensity ratio of the O and the I centre (PL_O/PL_I) followed equation (5.2) (allowing for an MBE growth roughness of $\pm$ 1ML). The ASL1982 even has shown that the PL ratio is the same as the symmetric SL (SL1885). The above values are appended onto the previous graph (fig. 5.16) representing the PL intensity ratio with respect to the layer thickness and shown in fig. 6.3. Without further fitting, the PL intensity ratios in ASLs show good agreement with the ones in the symmetric SLs.

The parameter *D* was previously used to represent the layer thickness of the SLs. However the parameter could not separate CaF_2 and CdF_2 layers when it was associated with describing PL intensity ratios for symmetric SLs. By investigating the PL intensity ratios of the ASLs it was established that the appropriate parameter *D* governing the thickness-dependence of the PL intensity of the I and the O centres is due to the thickness

of the CaF_2. It is now feasible to investigate the effect of the additional thermal and UV excitation as described in earlier chapters. In the following subsections the PL behaviour of the I and O centres in ASLs under influence of thermal and UV excitation is discussed.

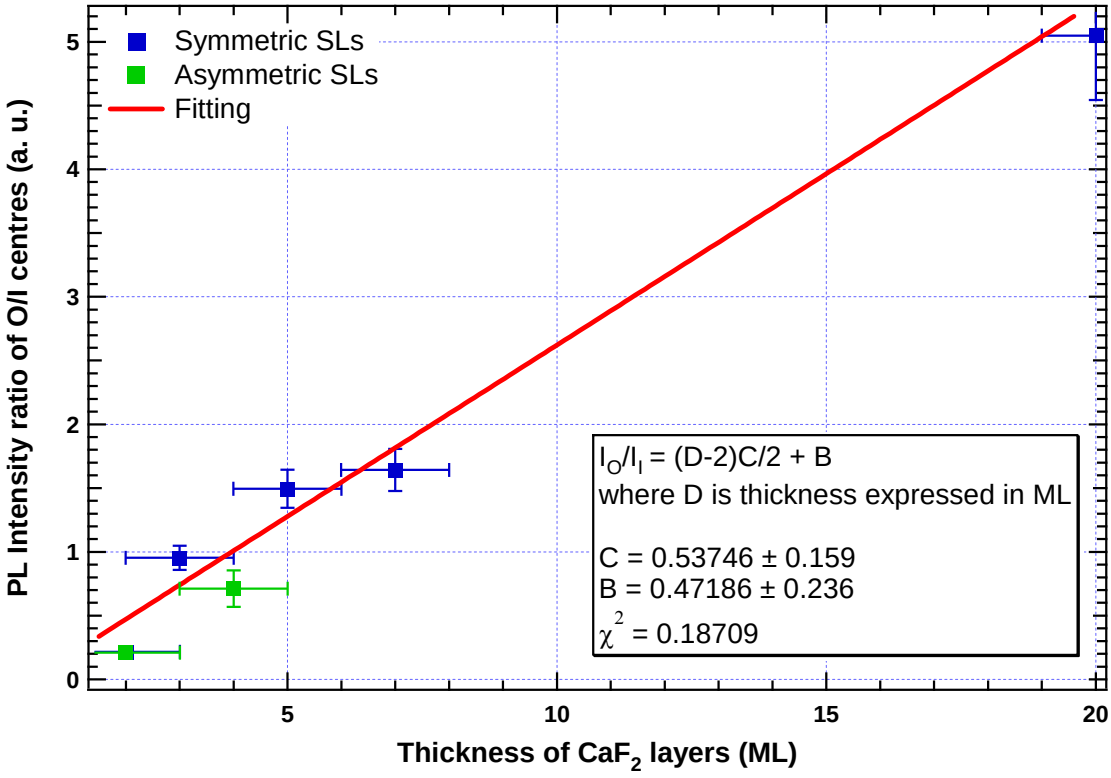

Fig. 6.3. Linear fitting of the PL intensity ratio of the O and the I centres with respect to the thickness of CaF_2 layers according to equation (5.2). The PL ratio values of the ASLs are only appended onto the graph for comparison. No further fitting including those points were performed.

6.2.1. Temperature dependence of Eu^{3+} photoluminescence in asymmetric CaF_2:Eu-CdF_2 superlattices

As mentioned in chapter 5, temperature dependent behaviour of the PL intensity of the I and the O centres was different. It was proposed that delocalisation of an electron in the vicinity of the I centre takes place at elevated temperature and therefore C_{3v} symmetry is diminished due to the removal of the electron. As a result, the quenching of the I centre was observed at lower temperature than that for the O centre. We further proposed a formation of a temperature-induced O centre upon the delocalisation of the electrons as

the electrons are the cause of the C_{3v} symmetry of the I centre. In other words transformation of the I centre into the O centre is expected to take place. No complete transformation was observed (fig. 5.18). However the PL intensity ratios between the O and the I centres were increased with respect to temperature for all SLs (fig. 5.22 (b)). This increase is interpreted as the indication of the decomposition of the I centre resulting in the transformation to the O centre. In addition to the transformation, it was concluded that the trapped electrons, either in the CdF_2 conduction band, or in CaF_2 in the vicinity of Eu^{3+}, have different thermal activation energy, E_b, depending on the thickness of the host SLs. For example, the calculated E_b for 5ML, 3ML, and 2ML symmetric SLs were 16 meV, 21.4 meV and 31 meV, respectively. Hence it was further concluded that the size confinement plays a deciding role in the depth of the electron trap.

The main purpose of the growth of ASLs is to to investigate this 'size confinement' for the trapped electrons. It was of interest to see how the thermal excitation would influence the size-induced binding energy, E_b, for the trapped electrons in $(CaF_2)_2$-$(CdF_2)_2$ SL and $(CaF_2)_2$-$(CdF_2)_{4L}$ ASL, for example. If the PL behaviour of Eu^{3+} in the latter host follows exactly the same as for the first one, then one can say that the electrons trapped in CaF_2 are responsible for such transformation. If there is a significant change, however, then it must be the electrons confined in the conduction band of CdF_2 which are responsible for the formation of the I centre. Fig. 6.4 and 6.5 show CEES results for $(CaF_2$:Eu$)_2$-$(CdF_2)_4$ (ASL1979) and $(CdF_2$:Eu$)_4$-$(CdF_2)_2$ (ASL1980) in temperature ranges from 4 K to 240 K.

For ASL 1979, up to room temperature, the O centre only appeared as a weak shoulder whereas the I centre was observable even at room temperature. This was almost the same for the $(CaF_2$:Eu$)_2$-$(CdF_2)_2$ symmetric SL (SL1885). Similarly the I centre in ASL1980 which has 4ML CaF_2 layers ($(CaF_2$:Eu$)_4$-$(CdF_2)_2$) followed an almost identical PL behaviour to that of symmetric 3ML, 5ML and 7ML thick SLs.

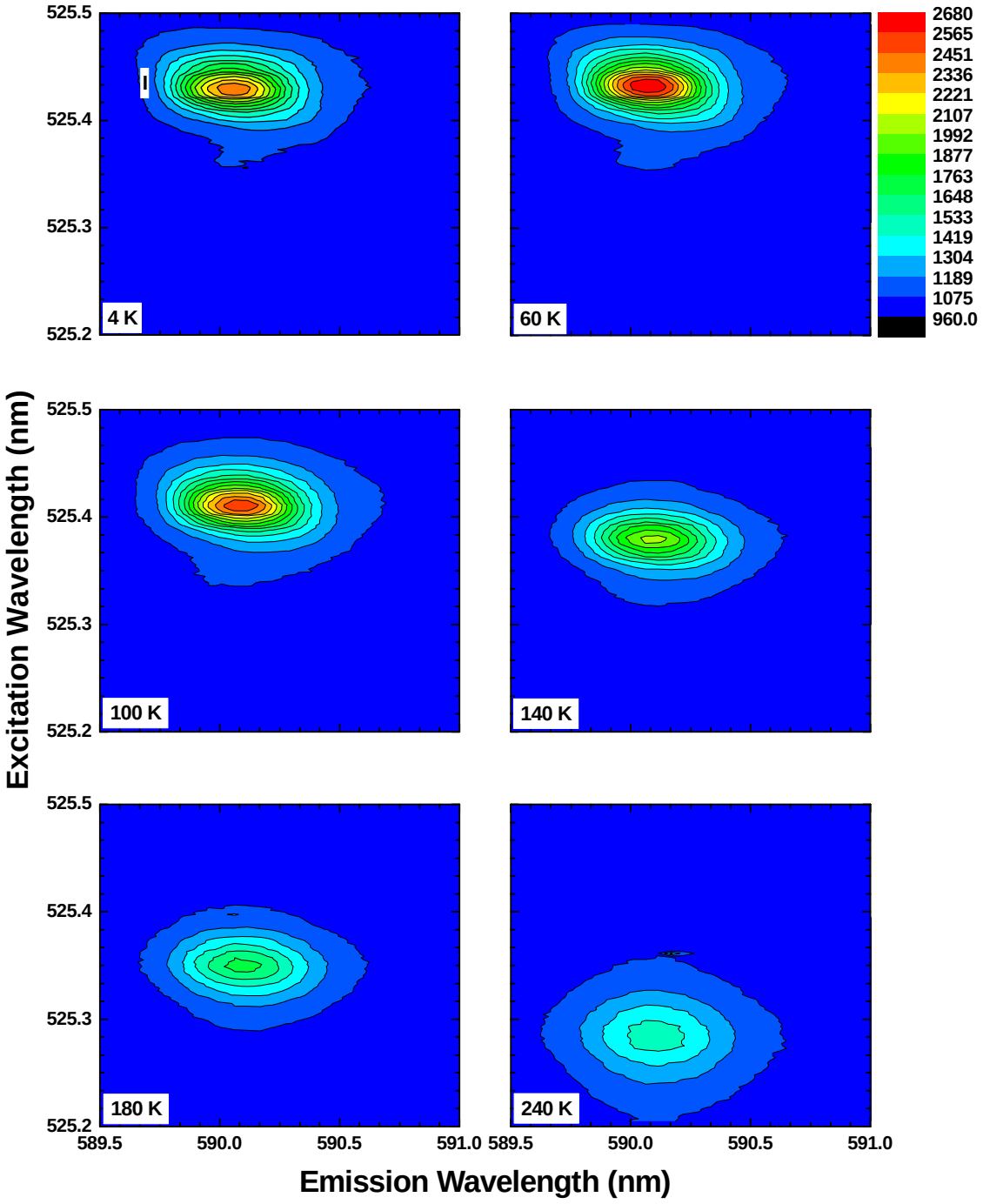

Fig. 6.4. CEES of the I centre in ASL 1979 $(CaF_2:Eu)_2$-$(CdF_2)_4$ in the temperature ranges between 4 to 240 K.

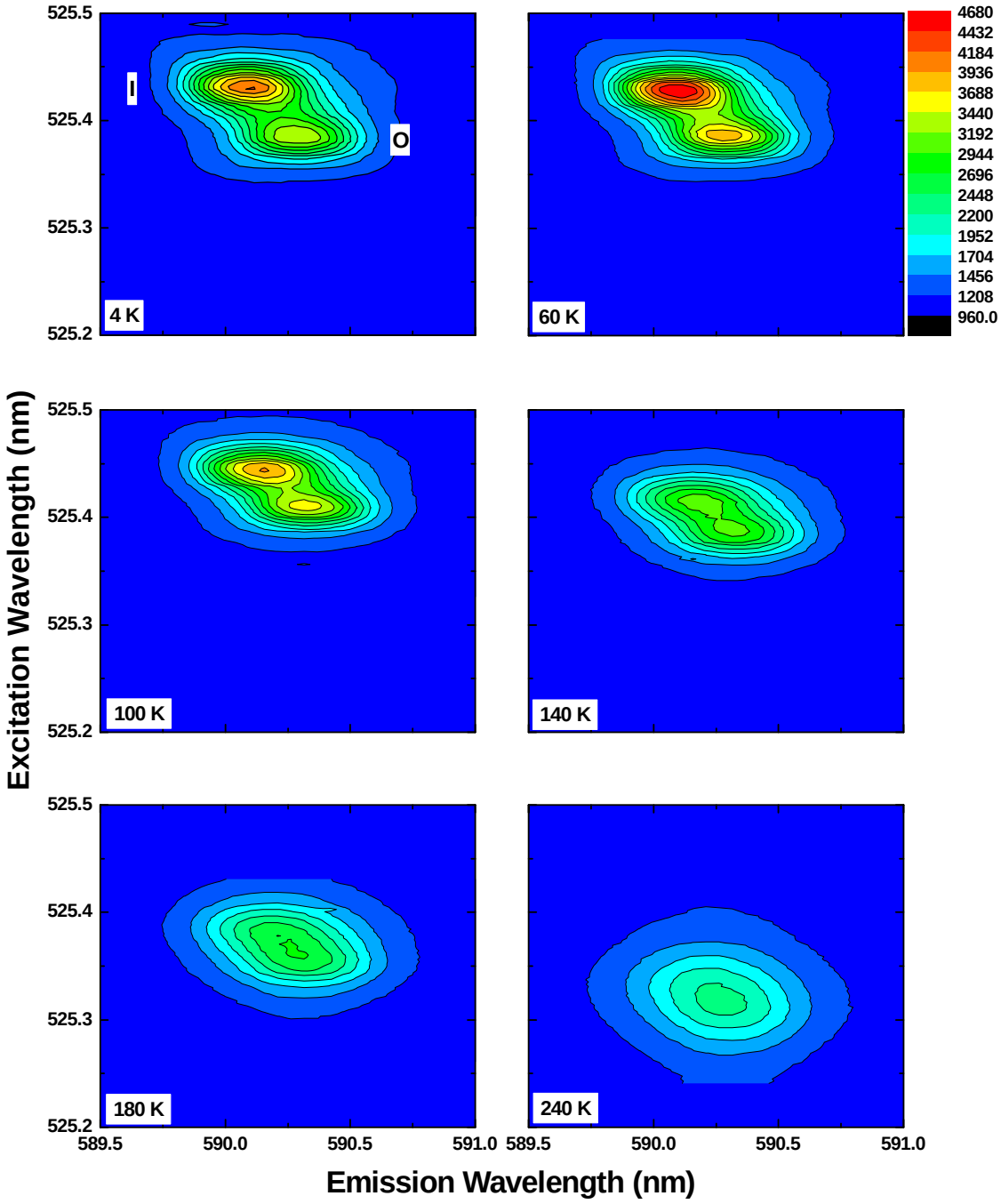

Fig. 6.5. CEES of the I and the O centres in ASL 1980 $(CaF_2:Eu)_4$-$(CdF_2)_2$ in the temperature range 4 to 240 K.

Recalling equation (5.5), the PL ratio of the O and the I centres with respect to temperature, *T*, is written as below,

$$\frac{PL_O}{PL_I} = \left\{ \frac{D}{2\left(1-\exp\left(-E_b / k_B T\right)\right)} \right\} - 1.$$

As defined earlier, *D* is the layer thickness of CaF_2 and E_b is the binding energy at low temperature. At each temperature step the PL intensities for the I and the O centre were estimated using Igor Pro. As for ASL1979 where the O centre is only observed as a weak shoulder, the expected profile of the the O centre is selected from the raw data as shown in fig. 6.1(a). As a result, the above model which describes the decomposition of the I centre and the growth of the O centre at elevated temperatures, agreed well with the ASLs results. The calculated PL intensity ratios and the experimental values are shown in fig. 6.6 and fig. 6.7, respectively for ASL1979 and ASL1980.

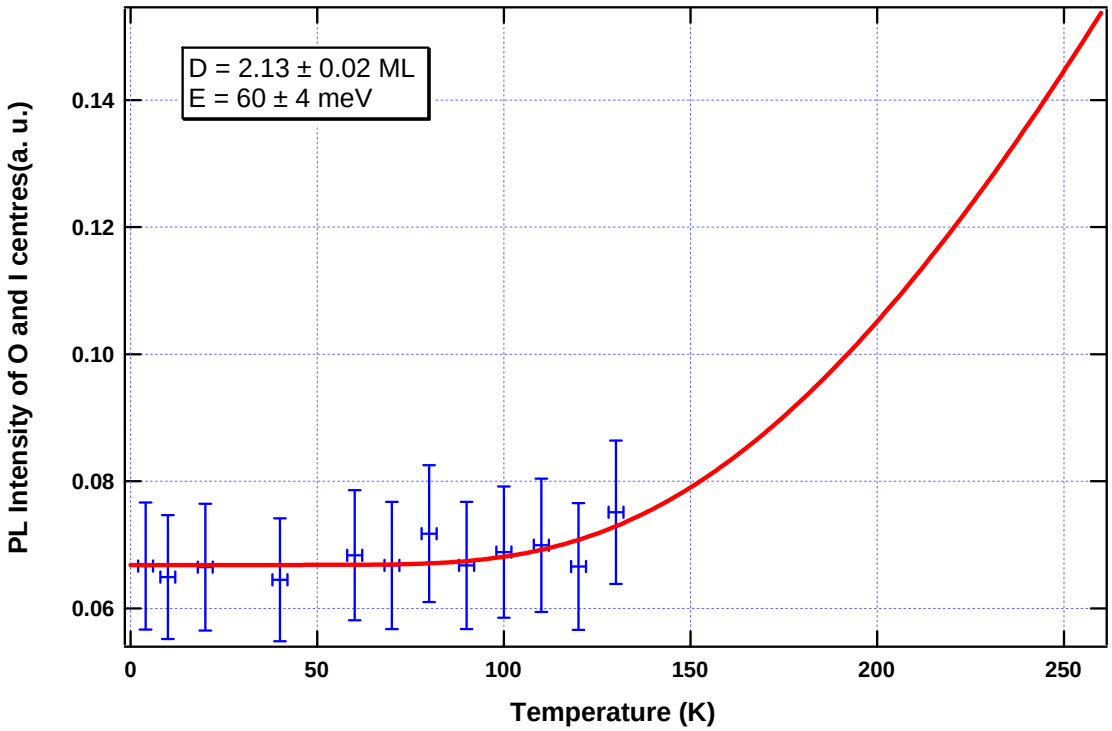

Fig. 6.6. The PL intensity ratio of the O and the I centres with respect to temperature for ASL1979 $(CaF_2:Eu)_2$-$(CdF_2)_4$. The solid line represents the calculated value using equation (5.5).

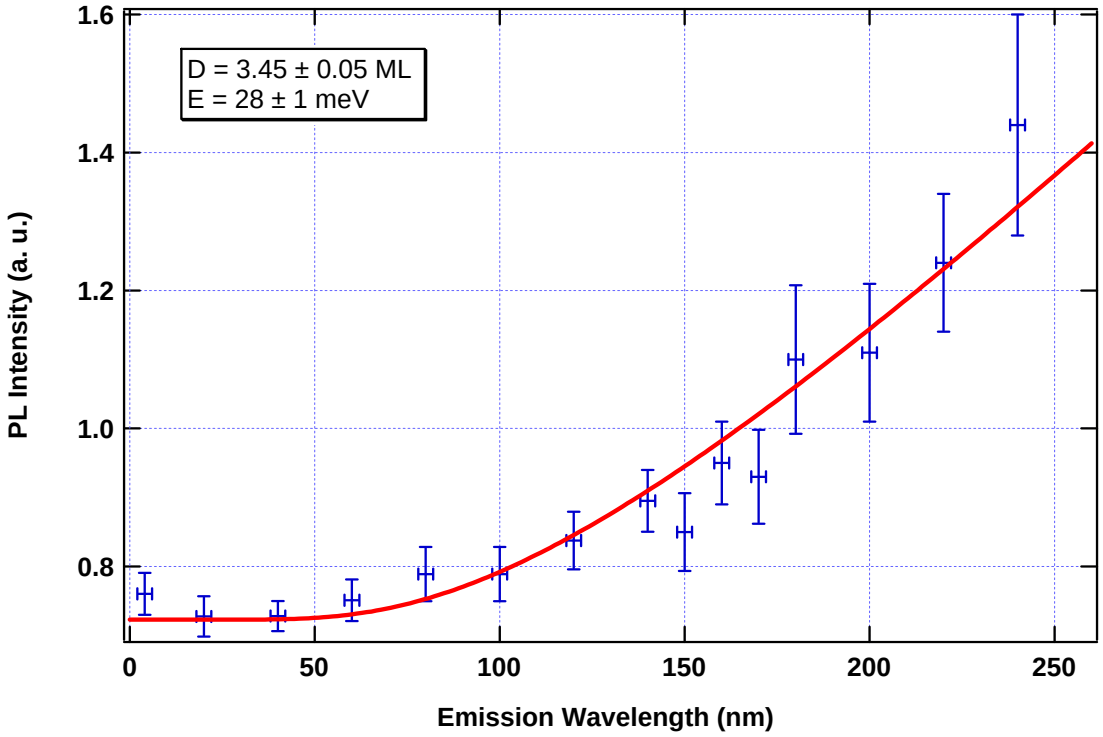

Fig. 6.7. The PL intensity ratio of the O and the I centres with respect to temperature for ASL1980 $(CaF_2:Eu)_4$-$(CdF_2)_2$. The solid line represents the calculated value using equation (5.5).

For ASL1979, the fitting was only carried out for temperature up to 130 K as the PL intensity of the O centre was very weak making a two peak Gaussian fit impossible. Using the available data points for the calculation of the binding energy, E_b, it was given by 60 ± 4 meV with corrected layer thickness of 2.12 ML. The χ^2 value of the fitting was 0.00005.

Relative to ASL1979, ASL1980 gave a smaller value of binding energy of 28 ± 1 meV with corrected thickness of 3.34 ML. The I centre was observed up to 140 K (fig. 6.5) and for temperatures past this point the measurement of peak PL intensity for the I centre became less accurate due to the thermal relaxation. Using the whole temperature range or the most accurate temperature range from 4 K to 140 K gave virtually no difference in the estimation of the binding energy. The χ^2 value for this fitting was 0.038.

It should be noted that the PL behaviour of the I and the O centre in ASLs exactly follows that of the SLs at elevated temperature. In other words, the delocalisation of the trapped electrons is closely related to the layer thickness of CaF_2. The behaviour is summarised in

fig. 6.8. Again due to the possible size confinement, the delocalisation of the electrons becomes less efficient in thinner CaF_2 layers.

In addition, there is no experimental evidence that the thickness of CdF_2 influences the delocalisation. The thermal delocalisation of the trapped electrons is possibly purely dependent on the thickness of CaF_2 layer regardless of the thickness of CdF_2. However this does not disprove any influences of electrons in the conduction band of CdF_2. We still assume that there are electrons in the conduction band but these electrons are not necessarily contributing to the formation of the I centre and hence the transformation of that centre to the O centre at elevated temperatures.

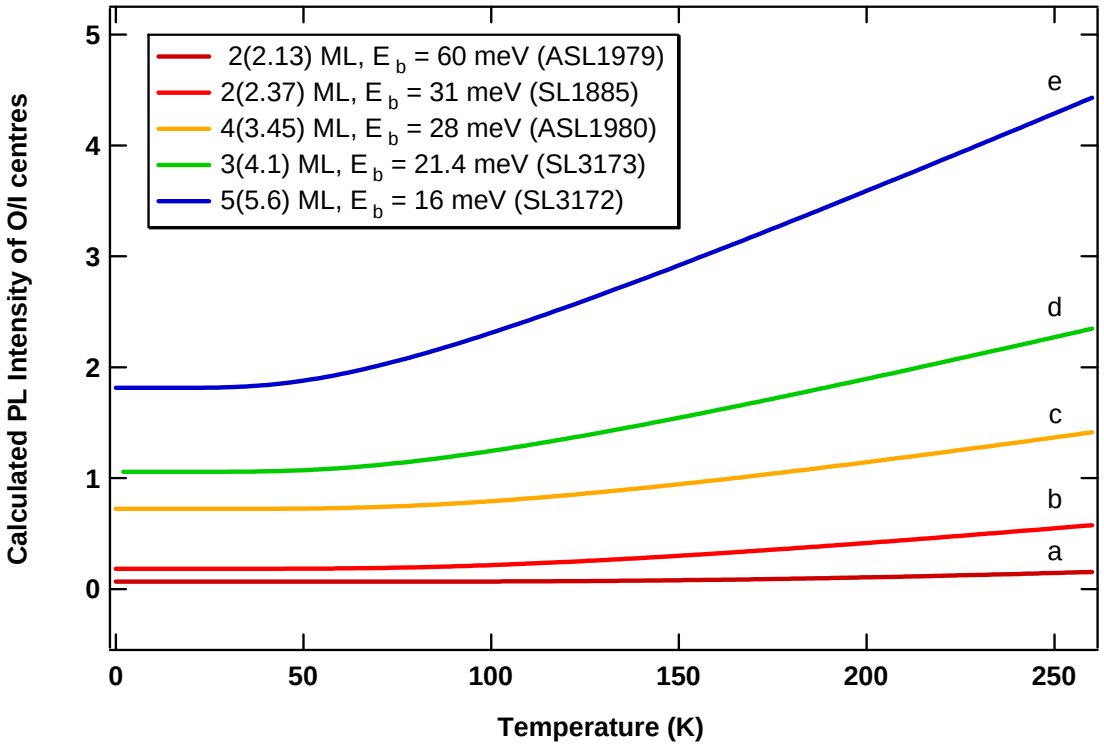

Fig. 6.8. Calculated PL intensity ratios of the O and the I centres in (a) ASL1979, (b) SL1885, (c) ASL1980, (d) SL3173 and (e) SL3172.

The binding energy should now be considered as the trapping of electrons in defect centres within CaF_2 layers in the vicinity of the cubic Eu^{3+} centre. Also the trapping of the electrons has some tendency of size confinement. Fig. 6.8 shows a graph of calculated electron delocalisation model equation (5.5) in SLs and ASLs. It clearly shows that the

thinner the CaF_2 layers, the greater the binding energy for the electrons. The binding energies for the investigated ASLs and the symmetric SLs are summarised in table 6.1.

Table 6.1. Binding energy of electrons in CaF_2 layers.

Thickness of CaF_2 (ML)	Corrected thickness (ML)	Binding energy (meV)
2 (ASL1979)	2.13	60 ± 4
2 (SL1885)	2.37	31 ± 1
4 (ASL1980)	3.45	28 ± 1
3 (SL3173)	4.1	21.4 0.7
5 (SL3172)	5.6	16 ± 2

6.2.2. PL behaviour of Eu^{3+} centres under additional UV excitation

In addition to the thermal delocalisation of the electrons, additional UV excitation was also provided to the ASLs to eventually delocalise the electrons as described in chapter 5. A He-Cd laser with an output wavelength of 325 nm was used as an additional source of excitation on top of the $^7F_0 \rightarrow {}^5D_1$ excitation of the Eu^{3+}. For each ASL, CEES of the I and the O centres was taken before, during and after the UV excitation as shown in fig. 6.9.

For ASL1982 [$(CaF_2{:}Eu)_2$-$(CdF_2)_4$], no visual observation of an increase of the O centre under the UV excitation was seen in the contour plot of the CEES. The influence of the UV excitation was further analysed by performing Gaussian fittings to the emission profile of fig. 6.9. Taking residuals of the fittings into an account as uncertainty in peak intensity, as shown in fig. 6.10, there is virtually no UV-induced effect on the PL intensities. Here the PL intensity ratio of the O and the I centres is an indicator of the influence of the UV excitation. The PL intensity ratios (PL_O/PL_I) before and during the UV excitation are estimated to be 0.21 ± 0.01 and 0.21 ± 0.01, respectively. Hence there

is no evidence to conclude that the delocalisation of the electron takes place in ASL1982 under UV excitation. Moreover, this is the same as for the symmetric $(CaF_2:Eu)_2$-$(CdF_2)_2$ SL (SL1885). In chapter 5 the PL ratios for the symmetric SL (SL1885) were observed as 0.14 ± 0.03 and 0.15 ± 0.02, respectively for before and during the UV excitation. These two results, once again, suggest that due to the possible size confinement the influence of the UV excitation is negligible and that confinement is due to the thickness of CaF_2 regardless of the CdF_2.

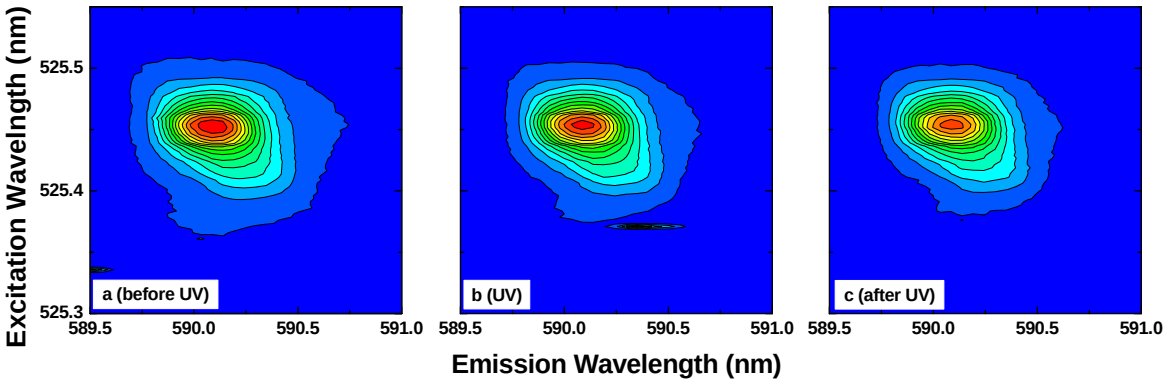

Fig. 6.9. CEES of ASL1982 $(CaF_2:Eu)_2$-$(CdF_2)_4$ (a) before, (b) during and (c) after UV excitation on top of the $^7F_0 \rightarrow {}^5D_1$ excitation of Eu^{3+}. All spectra were recorded at 4 K.

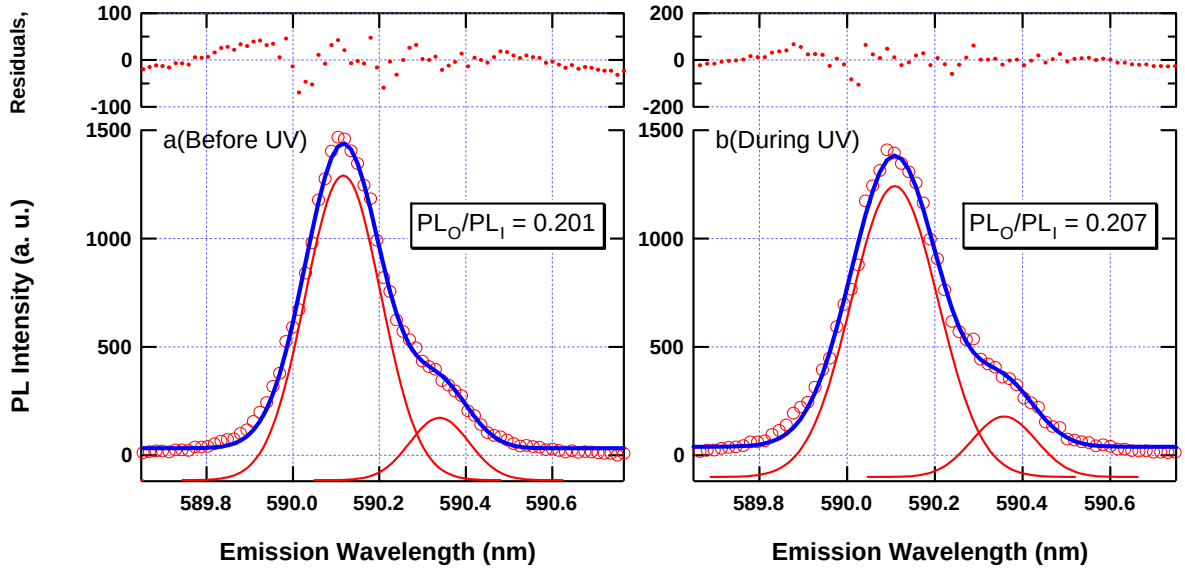

Fig. 6.10. Gaussian fittings of emission profiles of ASL1982; (a) before and (b) during the UV excitation. PL intensity ratios of the O and the I centres are 0.201 and 0.207, respectively.

On the other hand for ASL1980 [$(CaF_2:Eu)_4$-$(CdF_2)_2$] the additional UV excitation clearly changed the PL intensity of the I and the O centres. As shown in figs. 6.11 and 6.12, one can see that the PL intensity of the O centre is even higher than that of the I centre during the illumination of the UV laser. The PL ratios are estimated to be 0.71 ± 0.03 and 1.08 ± 0.05, respectively for before and during the UV excitation. Upon ceasing UV excitation the PL ratio of the O and the I centre returned to its original value within the limits of uncertainty. As discussed in chapter 5, the change in the PL intensity repeated over several cycles. Again, the PL intensity behaviour under the influence of the UV excitation seemed solely dependent on the thickness of CaF_2.

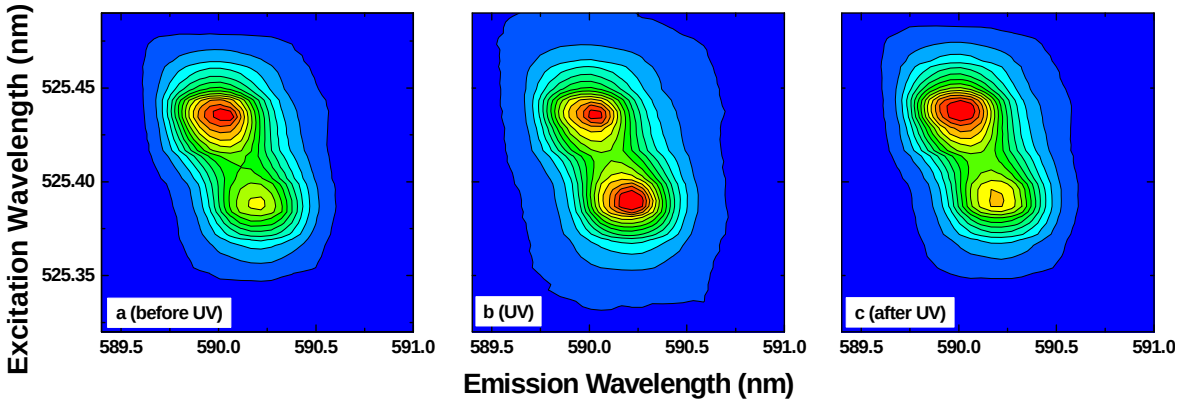

Fig. 6.11. CEES of ASL1980 $(CaF_2:Eu)_2$-$(CdF_2)_2$ (a) before, (b) during and (c) after UV excitation on top of the $^7F_0 \rightarrow {}^5D_1$ excitation of Eu^{3+}. All spectra were recorded at 4 K.

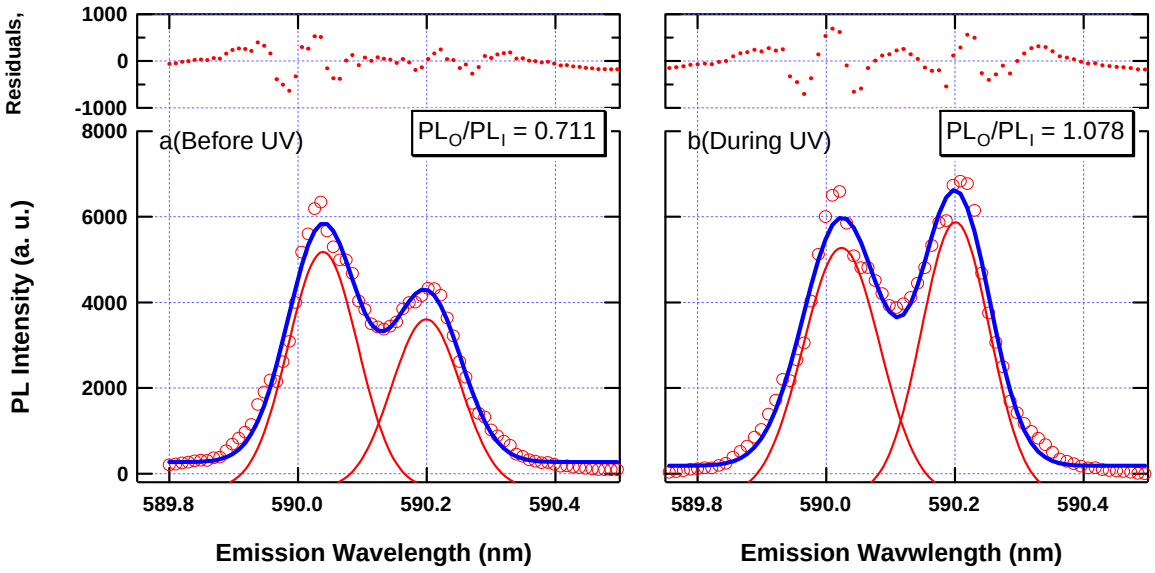

Fig. 6.12. Gaussian fittings of emission profiles of ASL1980; (a) before and (b) during the UV excitation. The PL intensity ratios of the O and I centres are 0.711 and 1.078, respectively.

Recalling equation (5.8) the ratio of normalised PL intensities of the O and the I centres can be rewritten as follows,

$$\frac{PL_O}{PL_I} = \frac{((D-2)+2A)}{(D-2)(1-A)}.$$

The parameter D is the layer thickness of CaF_2 and A is thickness dependent PL intensity decay coefficient as defined in chapter 5. This model says that the PL decay of the I centre due to the delocalisation of the electrons should be responsible for the growth of the O centre PL intensity. The ratios of the normalised PL intensity of the O and the I centres in ASLs were appended to the previous model fit. Without performing any modification to the fit, ASL1980 [$(CaF_2:Eu)_4$-$(CdF_2)_2$] shows good agreement with the other SLs and thus follows the model quite well as shown in fig. 6.13. However ASL1982 [$(CaF_2:Eu)_2$-$(CdF_2)_4$] did not follow the model. This is the same for the 2 ML thick symmetry SL as we observed earlier.

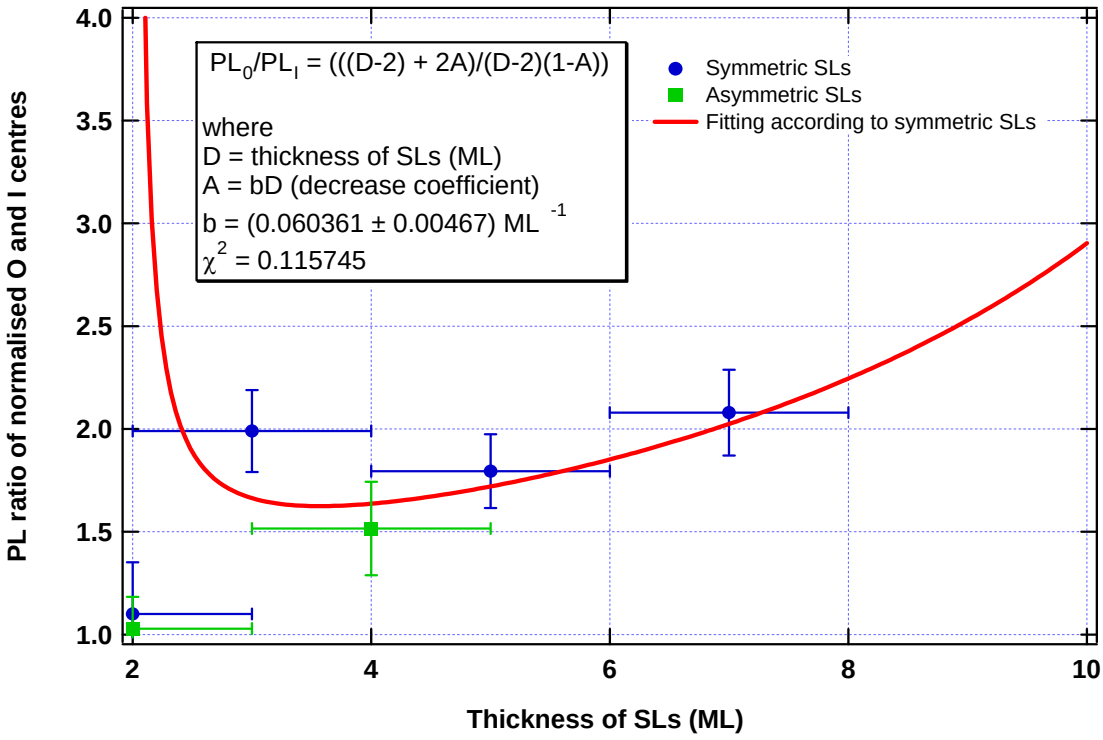

Fig. 6.13. Ratios of normalised PL intensities of the O and the I centres in various SLs and ASLs. The solid line represents the UV-delocalisation model.

It was suggested, in chapter 5, that the size confinement makes harder for UV light to delocalise electrons resulting in less transformation of the I centre to the O centre. For 2ML thick CaF_2 layers, *A* becomes negligible, or in other words there is insignificant possibility of electron delocalisation. It should be noted that there is no contribution from the thickness of CdF_2 for this transformation as there is no difference between the PL ratios for SL1885 and ASL1982. This similarity of PL behaviour of SLs and ASLs suggests that the transformation of the I centre is entirely caused by the electrons in the CaF_2 layers. In addition, the transformation is observable upon UV excitation and is reversible when the UV excitation stops.

6.3. Summary

Comparison of the PL results for ASLs and symmetric SLs appears to rule out one of our earlier assumptions; that electrons in the conduction band of CdF_2 are possibly responsible for the formation of the I centre (and that the thickness of the CdF_2 layers causes different confinement for the electrons). The PL behaviour of the I and the O centres in ASLs given by additional thermal and UV excitations was almost identical to that for symmetric SLs. The PL behaviour of the centres are dependent on the thickness of CaF_2 regardless of the thickness of CdF_2. It should be noted that the electrons trapped in CaF_2 layers are now thought to be mainly responsible for formation of the I centre and for the PL behaviour of the I and the O centres under thermal and UV excitations.

However the PL behaviour of the I and the O centres has still exhibited strong dependence on the thickness of the CaF_2 layers. For 2ML thick CaF_2 layers, for example, whether symmetric SLs or ASLs, it was almost impossible to transform the I centre to the O centre upon the UV excitation. In addition, the estimated binding energy for 2 ML thick CaF_2 is 60 meV which is almost as four times as larger than that for thicker CaF_2 layers.

Chapter 7

Discussion of the charge compensating electron for the novel I centre in CaF_2:Eu-CdF_2 SLs

7.1 Introduction

It is instructive to extend the analysis of the effective role of the charge compensating electrons for the 'Interface' centre of Eu^{3+} in SLs and ASLs. It was suggested from previous chapters that the PL intensity behaviour of the I centre is closely related to a neighbouring electron next to the Eu^{3+} centre and its possible delocalisation. In this chapter a crystal field analysis was carried out considering the crystal structure of the I centre. A localised electron in the [111] direction is incorporated into the previously considered distorted cubic centre of Eu^{3+}. The evaluated crystal field parameters are compared with that of the O centre in section 7.2. The PL behaviour of the I centre under additional excitation is also explored in this chapter. A broad range of additional excitations were tested using various laser lines and a lamp. The behaviour of the I centre PL intensity, relative to the O center, under the broad excitation, is thought to indicate the existence of an absorption band. The possible behaviour of the absorption band of the charge compensating electrons is discussed in section 7.3.

7.2 Crystal structure of the Interface centre of Eu^{3+} in CaF_2:Eu-CdF_2 SLs

To investigate the origin of the interface centre, a collaborative calculation was carried out to evaluate the energy level splitting of the $^5D_1$ and $^7F_1$ multiplets for Eu^{3+} in the I

centre using appropriate crystal field parameters [1]. The exchange model was used in the calculation. It was assumed that the I centre has three Cd^{2+} neighbouring ions as compared to the O centre which has twelve Ca^{2+} neighbours. It was further assumed that an electron, which is responsible for the Eu^{3+} charge compensation, is localised near the three Cd^{2+} ions. The crystal structure used in the calculation is depicted schematically in fig. 7.1(a). As a result, the calculated energy level splitting for the $^5D_1$ and $^7F_1$ multiplets are 7 cm^{-1} and 16 cm^{-1}, respectively. In chapter 5 the experimental values of the splitting for the I centre were 2.5 cm^{-1} and 13.2 cm^{-1}, respectively suggesting that the calculations are consistent with the experiment.

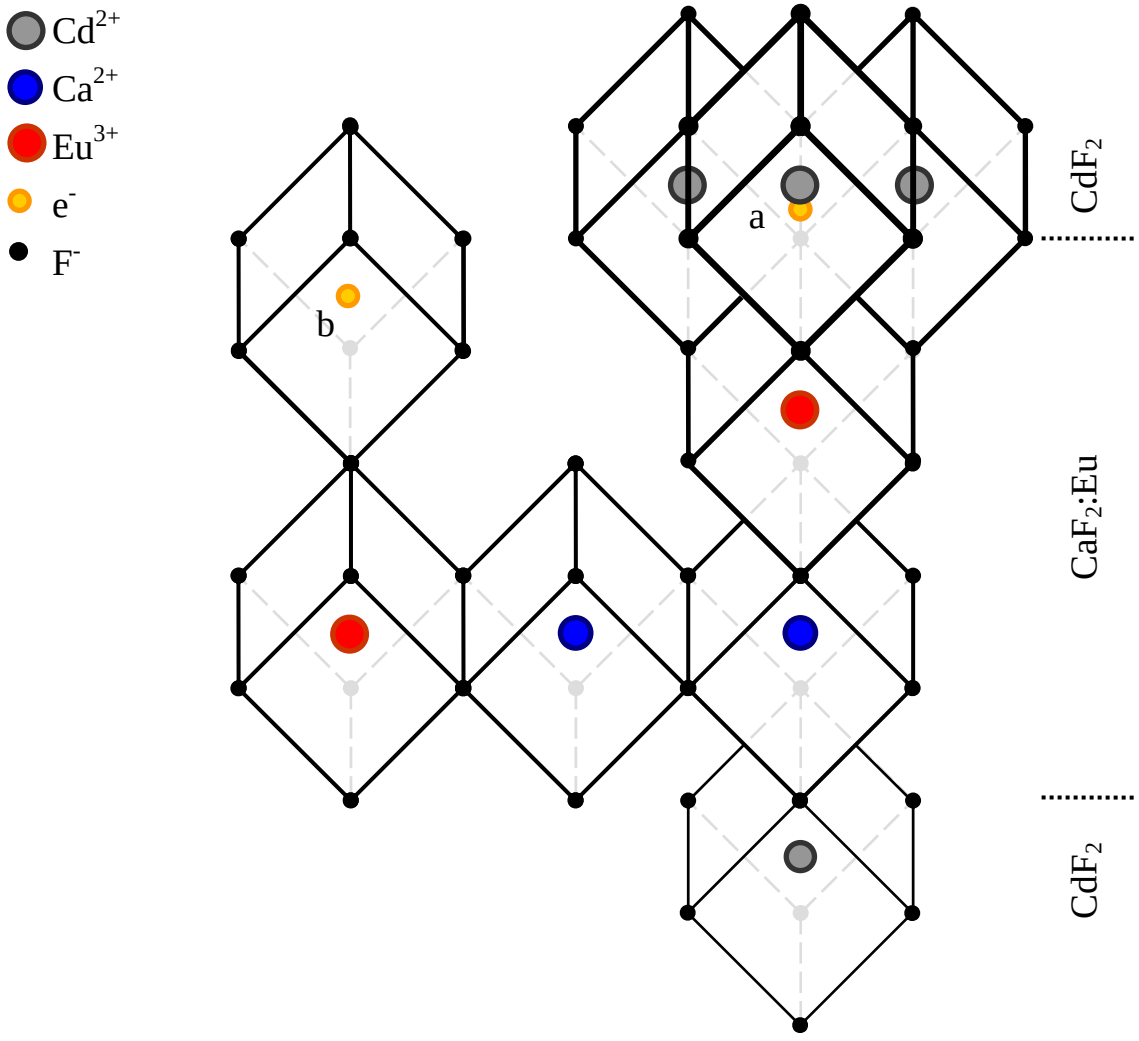

Fig. 7.1. Schematics of layer composition of a CaF_2:Eu-CdF_2 SL. Localisation of an electron takes place (a) near the three nearest Cd neighbouring ions or (b) at a corner of cube containing Eu^{3+}.

This attempt to incorporate the additional electron charge in the crystal structure for the calculation of energy levels splitting was considered successful. The predicted splittings are the same order of magnitude as the experimental values. However, some concerns arose in dealing with the transformation between the centres. It is evident that the I centre transforms to the O centre upon additional UV or thermal excitation as discussed in chapters 5 and 6. Using the above model, with the presence of the Cd^{2+} ions, it is difficult to show such transformation behaviour for the I centre. For instance, the calculated energy level splitting for the $^7F_1$ multiplet of the I centre is not necessarily the same as the splitting of the cubic centre [1] when the electron is removed from the I centre. Fig. 7.2 shows the difference in the degree of splitting of the $^7F_1$ multiplet. It should be noted when the electron is removed from the I centre (fig. 7.2(b)), the order of the doublet and singlet is reversed as the O centre polarisation showed. However the degree of the splitting for the multiplet is not equal to that of the O centre (fig. 7.2(c)). It is due to the fact that the crystal structure was assumed to be different in the first place. For the I centre the crystal field parameters are evaluated including the three Cd^{2+} ions which are, however, not concerned for the O centre. In other words, even when the electron is delocalised the crystal structure of the electron-removed I centre is not the same as the O centre.

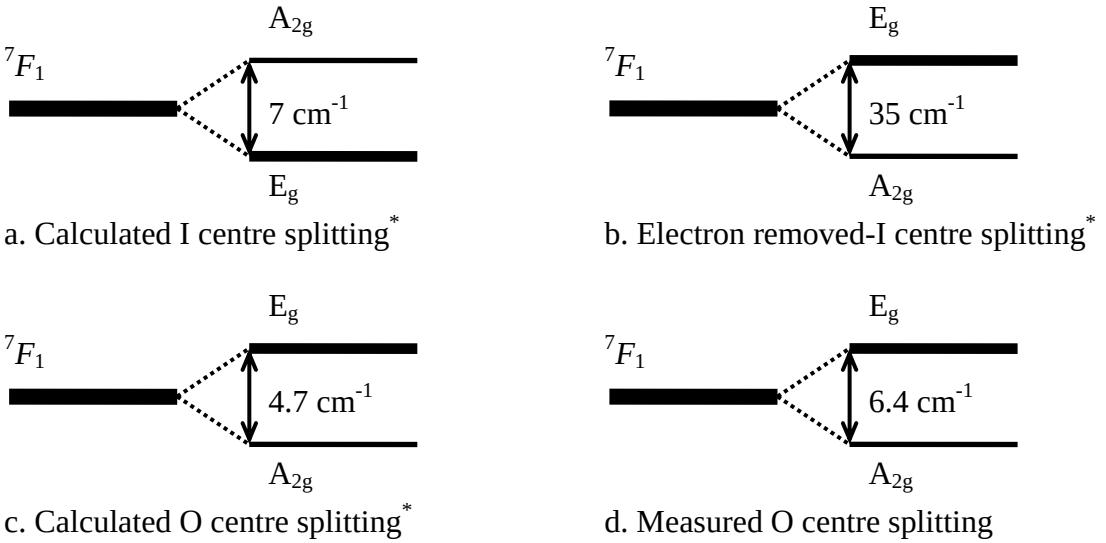

Fig. 7.2. The calculated energy level splitting of the $^7F_1$ multiplet of the (a) I centre, (b) electron-removed I centre, (c) O centre and (d) measured O centre. Note that the splitting in the O centre is due to the strain of SLs. In chapter 5 the splitting is calculated as 6.3 cm^{-1} using the point charge model. *The calculated values are from ref. [1].

Similar calculations are carried out using a point charge model [2]. An interstitial electron was placed in the [111] direction of the cubic centre as shown in fig 7.1(b). The model does not distinguish the charge of a fluoride ion and an electron. However upon the UV excitation at low temperature we observed the possible electron delocalisation which led us to eliminate the possibility for an interstitial fluoride ion acting as the charge compensator. In fact the mobility for F^- ions at low temperatures is considered as insignificant. We assumed that during the MBE process an electron enters interstitially in a cube which is in a [111] direction from the Eu^{3+} centre and becomes localised. As a result an electron charge compensated I centre is formed. This charge compensated centre only differs from the cubic centre by the presence of the electron localised in the [111] direction. Further this electron can be delocalised by an additional excitation which results in transformation of the charge compensated centre to the cubic centre. The experimental finding of the possible transformation of the I centre to the O centre is consistent with the above consideration. However this assumes that three neighbouring Cd^{2+} cations are not responsible for such formation of the I centre.

The empirical 'f-shell' programme was used for the calculation for the energy levels of the I centre. The crystal field parameters are firstly obtained using the point charge model for the distorted cubic centre as described in section 5.3. Then the appropriate crystal field parameters are further evaluated with the extra electron along the [111] direction. The energy levels of the I centre in C_{3v} symmetry are obtained with a standard deviation, σ = 73 cm^{-1} and are summarised in table 7.1. The splitting of the $^5D_1$ and the $^7F_1$ multiplets are also presented in fig. 7.3. It should be noted, as shown in table 7.2, that the crystal field parameter B_c^2 became positive when the electron is place along the [111] direction (as opposed to being negative for the distorted cubic crystal structure). The conversion of the sign is reflected in the symmetry assignments for the crystal field levels. In chapter 5, it was shown that the E_g doublet of the $^5D_1$ and the $^7F_1$ multiplets is energetically higher than the singlet A_{2g} (fig. 5.28). The doublet is now lower than the A_{2g} singlet in each case. Using the new set of parameters the calculated values for the splittings in the $^5D_1$ and the $^7F_1$ multiplets are respectively 2.69 cm^{-1} and 8.69 cm^{-1} which are somewhat closer to the experimental values; 2.5 cm^{-1} and 13.2 cm^{-1} than the earlier calculations [1].

Table 7.1. Calculated energy levels of Eu^{3+} in the I centre in CaF_2:Eu-CdF_2 SLs (cm^{-1} in air)

Multiplet	State and symmetry	I centre levels (cm^{-1})	
		Calc.	Expt.
$^7F_0$	A_{1g}	-44	0
$^7F_1$	E_g	321	335
	A_{2g}	331	348
$^7F_2$	T_{2g}	815	813
	E_g	1276	1335
$^7F_3$	T_{1g}	1852	1855
	T_{2g}	1971	1958
$^7F_4$	T_{1g}	2880	2890
$^5D_0$	A_{1g}	17286	17283
$^5D_1$	E_g	19076	19029
	A_{2g}	19079	19032
Std Dev	σ	73	

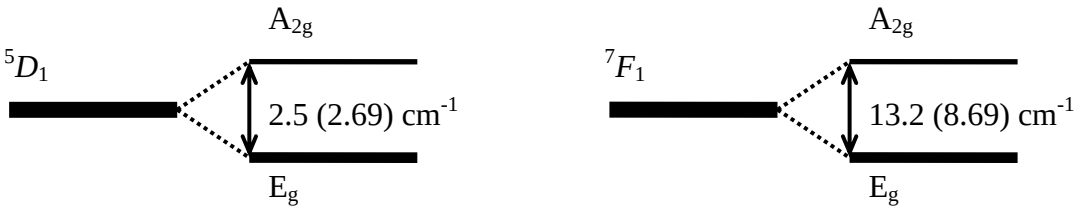

Fig. 7.3. The observed splitting of the I centre of Eu^{3+}. The $^5D_1$ and the $^7F_1$ are both split into two levels separated by 2.5 cm^{-1} and 13.2 cm^{-1}, respectively. Inside the brackets are the calculated values.

Table 7.2. Crystal field parameters for the distorted O and the I centres (cm^{-1}).

Parameters	Distorted O centre	I centre
B_c^2	-32	10
B_c^4	-820	-790
B_a^4	2000	1900
B_c^6	47	95
$B_{a'}^6$	510	490
B_a^6	870	930

As mentioned above, the major difference between the crystal field parameters for the I and the O centre is the conversion of the sign of the B_c^2 parameter. The rest of the parameters are optimised by the 'f-shell' programme to yield the minimum σ. However a small degree of change in the rest of the parameters are expected as they are weakly coupled with the B_c^2. The above model is consistent with the experimental findings. The presence of the charge compensating electron plays a deciding role which separates the I and the O centre transition energies and splitting. It can also show that when the electron is removed from the I centre, the resultant centre is the O centre.

7.3 Absorption band for the charge compensating electron

So far at low temperature only the UV laser was optically used to investigate the possible transformation of the I centre to the O centre as discussed in chapters 5 and 6. Some other laser lines which are energetically lower than the He-Cd laser were also used to monitor the PL intensity ratios of the O and I centres as described in the previous chapters. The reasons for that are to find the transformation threshold of the centres and more importantly to observed any absorption band behaviour from the localised electrons. In comparison with the absorption bands exhibited for a trapped electron in fluorine vacancy, (so called F-centre) a similar proposal can be made with the current study. For the F-

centres, the energy levels are present for the confined electron and hence one can observe optical transitions from the F-centres [3]. The absorption bands of the F-centres in CaF_2 crystals have been studied by many researchers over the past decades [4-10]. We might expect to observe somewhat similar absorption bands from the localised electrons in SLs. In the case of SLs, as we proposed in section 7.2, the electrons are localised interstitially in the cubic lattice as opposed to the F-centres in which electrons are localised in fluorine vacancies. This can be considered as the fundamental difference between the F-centre and the charge compensating electron centre in SLs. However, in both cases electrons are confined in a potential well provided by surrounding ions and therefore form energy levels.

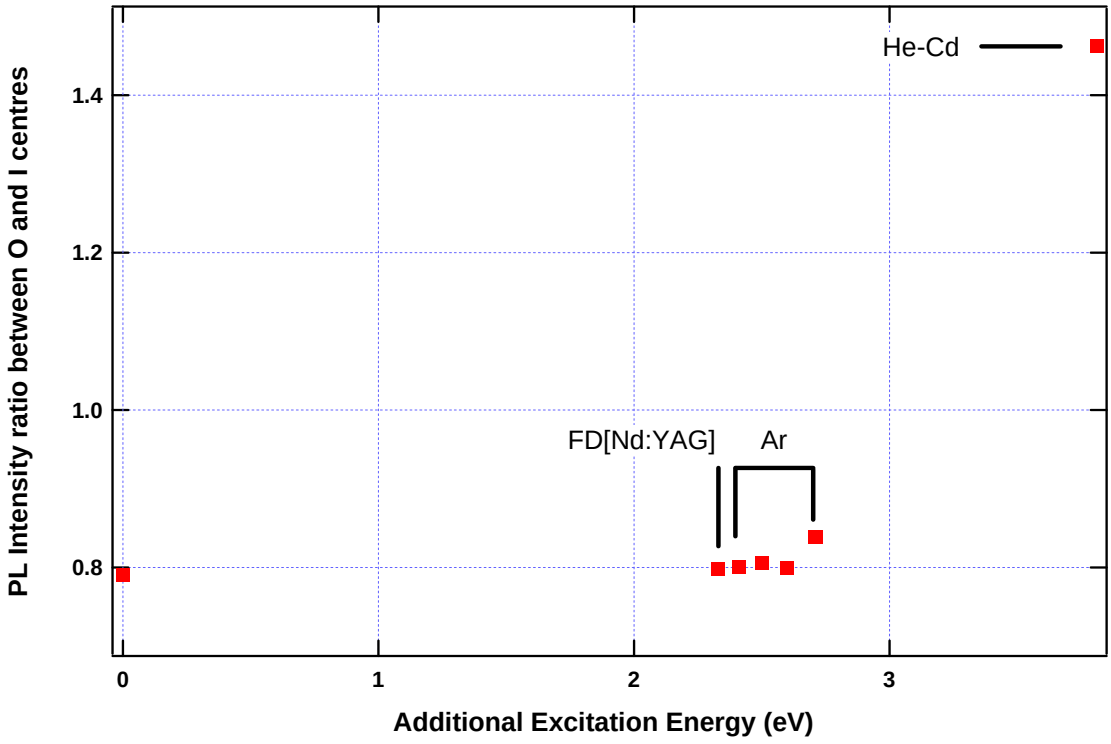

Fig. 7.4. PL intensity ratio of the O and the I centre without additional excitation and under various additional excitations. The SL3173 [$(CaF_2{:}Eu)_3$-$(CdF_2)_3$] was used for this experiment. All data were collected at 20 K.

Fig 7.4 shows the PL intensity peak ratios (O/I) of the O and the I centres in a 3 ML thick SL under various additional excitations at 20 K. On top of the dye laser excitation, a line from a frequency doubled Nd:YAG (532 nm) laser, four lines from an Ar laser (515 nm – 457 nm) and the He-Cd laser (325 nm) were used as the excitation sources. All the lines

were set at the same power using appropriate filters. The power of each line was measured with a wavelength calibrated ‘Field Master’ power meter and its value was 25 mW.

It is evident that the transformation of the I centre to the O centre is not observable for most of the additional excitations. The threshold for the transformation was about 2.7 eV (457 nm). This implies that the absorption band of the electron in SLs possibly exists in the 2.7 eV to 4 eV region. Unfortunately the SLs are all grown on Si substrates which are opaque to visible wavelengths. Hence the direct measurement of the absorption band was not available for UV-VIS wavelengths. For that reason, the investigation of the absorption band had to be purely dependent on the PL intensity ratios of the I and the O centres.

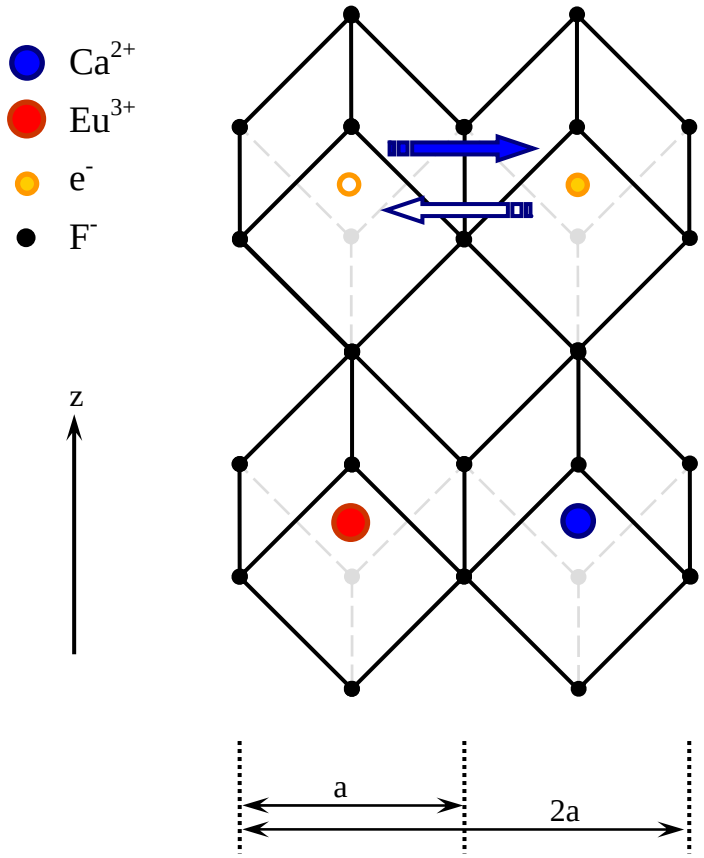

Fig. 7.5. Schematic of the electron delocalisation upon UV excitation. The symbol a is the lattice spacing.

The justification of the absorption band which explains the transformation of the I centre to the O centre is discussed in here. As we discussed in previous chapters, the electron which is responsible for the formation of the I centre must be delocalised in order to produce the O centre as a result. This requires an actual transfer of the electrons from one interstitial position to the other interstitial upon UV excitation as shown in fig. 7.5. However, when the UV excitation ceases the electron, or another nearby electron, must come back to the cube next to the Eu^{3+} interstitially to reproduce the I centre. The rates of transfer back and forth of the electrons are not necessarily the same as discussed in chapter 5 (fig. 5.25) with the recovery rate of the I centre (O center) seen to be slower than the initial decay (growth) rate.

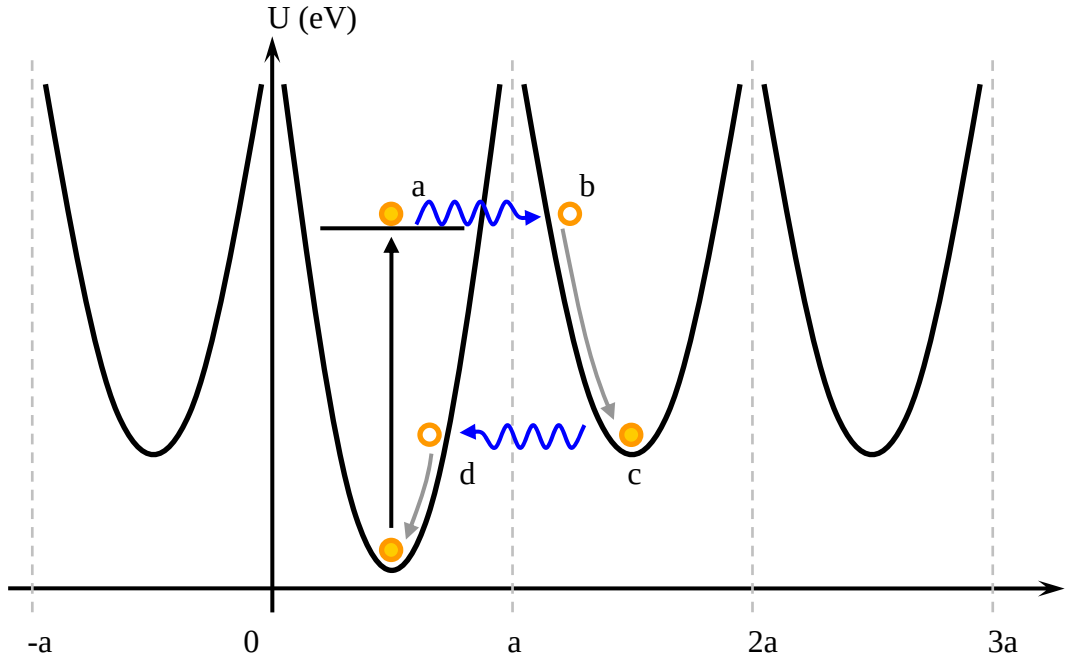

Fig. 7.6. One dimensional representation of energy barriers for the interstitial electron with respect to the lattice constant a. For the electron confined in $0 < x < a$, has a lower potential minimum than the others due to the stronger attraction from the Eu^{3+}.

Let us consider possible one-dimensional potential barriers (U) for the interstitial electron confined in a cube next to Eu^{3+} as shown in fig. 7.6. Assume that the minimum potential for the electron is lower than that of the rest of the interstitial cubes. This can be considered a result of stronger attraction from the Eu^{3+} ion than the Ca^{2+} ions. When the electron is excited by the UV laser a possible tunnelling is expected from an excited state of the electron (fig. 7.6 (a)) resulting in migration of the electron to a neighbouring cube

(fig. 7.6 (b)). At this stage the electron is physically far from the Eu^{3+} and hence the Eu^{3+} is left uncompensated during the UV excitation. After migration the electron energetically relaxes to the potential minimum (fig. 7.6 (c)). When the UV excitation ceases the electron can tunnel back with lower probability than the previous migration and localises interstitially in the cube to give the I centre (fig. 7.6 (d)). Let us further assume that the position of the excited state for the confined electron is dependent on the film thicknesses. The reason that no prominent transformation of the I centre to the O centre is observed in the 2 ML thick SL is possibly explained by this phenomenon. This is also consistent with the binding energy, E_b, for the localised electrons changing with the thickness of the SLs, as discussed in chapter 5. Because the excited level is influenced by the SL thickness the binding energies could also be affected.

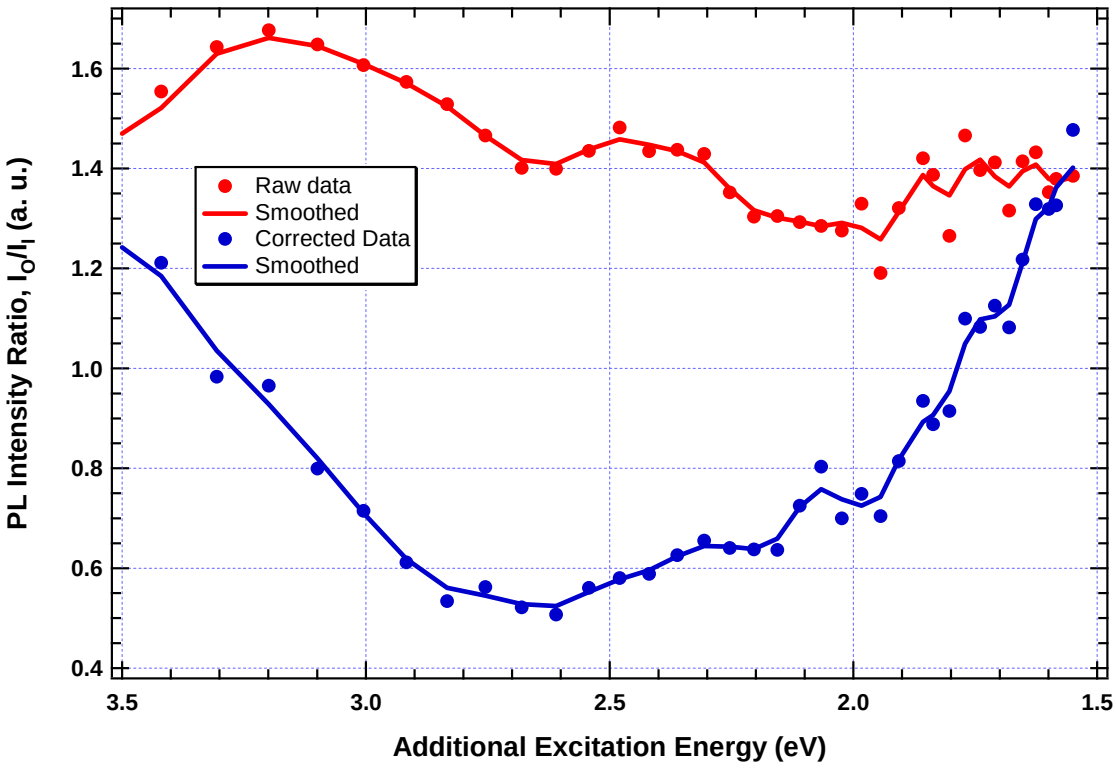

Fig. 7.7. PL intensity ratios of the O and the I centres in SL 3178 under additional excitation provided by a lamp.

To verify our hypothesis, a broad range of additional excitations were applied to the SLs and the PL intensity ratios are monitored. Selective excitation wavelengths from 350 nm to 800 nm were obtained using a tungsten coil quartz-iodine lamp with a small Bausch &

Lomb monochromator installed with a visible grating. Using appropriate lenses the excitation was focused onto the samples. The dye laser excitation was provided to excite the I and the O centres continuously as described in chapter 5. The peak intensity values of the centres were obtained by performing multi peak fittings and corresponding ratios are plotted against the additional lamp excitation wavelengths.

Fig. 7.7 shows the PL intensity ratio of the O and I centres under a broad range of excitation wavelengths. The blue line gives corrected data by taking into account the monochromator efficiency. The correction was carried out on the basis that the PL ratios of the O and the I centres exhibited a power dependency at 3.8 eV excitation using the He-Cd laser. Fig. 7.8 shows the PL ratios of the same sample under the 3.8 eV of an additional UV excitation. The PL ratios are almost linearly increased with decreasing UV laser power. This implies that, even at the same excitation energy, less transformation takes place with less power. Hence the efficiency of the monochromator governed by the grating performance had to be taken care of. The efficiency curve of the monochromator was found by comparing the theoretical blackbody radiation and the actual spectra from the monochromator using a calibration lamp. Then the efficiency curve was multiplied to the raw data.

It can be seen that transformation of the centres is taking place at two regions. It is evident that the UV laser used in chapters 5 and 6 (3.8 eV or 325 nm) is consistent with the trend given by the PL ratios. This reflects that there is an absorption band in higher excitation energy. There is also a possible absorption band peaking around 1.5 eV. However, due to the insignificant excitation power available with the visible grating of the monochromator the raw data were difficult to analyse in this low energy region. One can verify the presence of the absorption peak in the low energy region by employing an IR laser such as a tunable Ti:Sapphire laser. It has been shown that at fixed additional excitation wavelength, increasing the excitation power also increased the PL intensity ratio until saturation occurred. Hence employing powerful light sources in the low energy regions could establish the presence of an absorption band.

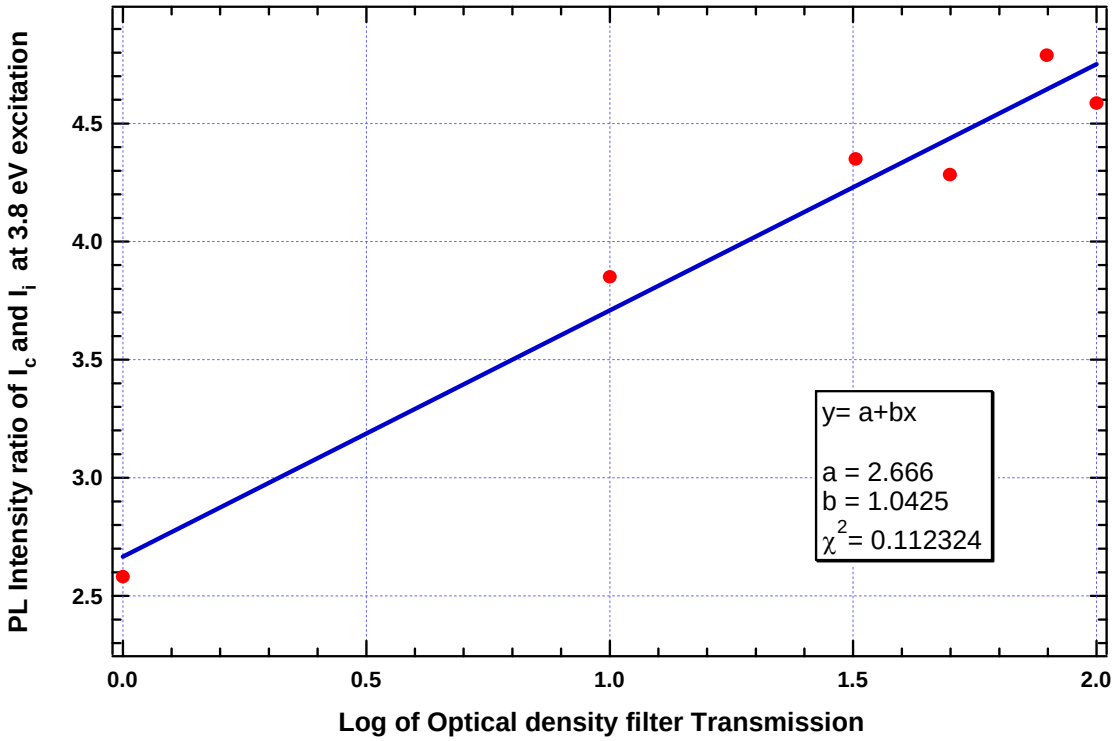

Fig. 7.8. PL ratios of the O and the I centres in SL 3178 with different power density of the He-Cd laser.

In summary, a model of crystal structure for the I centre is proposed incorporating a charge compensating electron localised interstitially in the [111] direction of the Eu^{3+} centre which is otherwise the cubic centre. The calculation carried out in this chapter agrees best with the splitting observed for the I centre in chapter 5 when the electron is along the [111] direction from the distorted cubic centre. The calculation also supports the delocalisation of the electron upon additional excitations. The removal of electron changed the sign and the magnitude of the B_c^2 parameter which is responsible for the opposite splitting for the I and the O centres.

Delocalisation of the electrons can be best described as tunnelling of the electrons through the potential barriers. To facilitate that, the existence of the absorption bands is proposed. The localised electrons are likely to form energy levels and tunnelling of the electron is more favourable from an excited level. The broad excitation suggests that there are possibly two absorption bands for the localised electrons.

References

[1] V. A. Chernyshev, A. V. Abrosimov, S. V. Gastev, A. V. Krupin, A. E. Nikiforov, J. K. Choi, R. J. Reeves, S. M. Suturin, N. S. Sokolov, "Energy structure of Eu^{3+} centres in CdF_2–CaF_2:Eu superlattices on silicon," *J. Phys.: Condens. Matter*, vol. 19, pp. 395023, 2007.

[2] M. F. Reid. University of Canterbury, New Zealand.

[3] N. W. Ashcroft, N. D. Mermin, *Solid State Physics*: Saunders College Publishing, 1976.

[4] T. Ewanizky, "Color center production in CaF_2:Eu^{3+} (Y^{3+}) by ultraviolet irradiation," *Phys. Rev.*, vol. 135, pp. A221-223, 1964.

[5] T. Kamikawa, Y. Kazumata, A. Kikuchi, K. Ozawa, "The F center in calcium fluoride," *Phys. Lett.*, vol. 21, pp. 126-128, 1966.

[6] D. A. Patterson, R. G. Fuller, "F Band in X and electron irradiated CaF_2," *Phys. Rev. Lett.*, vol. 18, pp. 1123-1124, 1967.

[7] D. L. Staebler, S. E. Schnatterrly, W. Zernik, "Linear dichroism in photochromic CaF_2," *IEEE J. Quantum Electronics*, vol. QE-4, pp. 575-578, 1968.

[8] R. C. Alig, "Theory of photochromic centers in CaF_2," *Phys. Rev. B*, vol. 3, pp. 536-545, 1971.

[9] D. L. Staebler, S. E. Schnatterrly, "Optical studies of a photochromic color center in rare-earth doped CaF_2," *Phys. Rev. B*, vol. 3, pp. 516-526, 1971.

[10] J. H. Beaumont, A. L. Harmer, W. Hayes, "An investigation of <100> and <110> oriented F_2 centres in CaF_2 and SrF_2," *J. Phys. C: Solid State Phys.*, vol. 5, pp. 1475-1488, 1972.

Chapter 8

Conclusion

8.1 Summary of results

Laser spectroscopy enabled the elucidation of physical properties of CaF_2:Eu-CdF_2 superlattices (SLs) and CaF_2:Eu thin films using Eu activators. For this study optical transitions of Eu^{2+} and Eu^{3+} were investigated using appropriate laser spectroscopic techniques.

The $4f^6 5d \rightarrow 4f^7$ transition of Eu^{2+} doped in CaF_2:Eu-CdF_2 SLs and CaF_2:Eu thin films exhibited a strain dependence behaviour. In particular, the zero phonon line (ZPL) of Eu^{2+} at low temperature showed that the peak is either blue or red shifted relative to the strain-free crystal. SLs and films under compressive planar strain exhibited the red shift while blue shift was observed for those under tensile stain. In fact, the ZPL shift is due to the uniaxial strain along [111] axis. For a CaF_2:Eu-CdF_2 SL which has 20 mono layers (ML) of each material, the planar strain is estimated as -0.35% (compressive). Also observed was that the shift tends to relax to the strain-free ZPL as the thickness of CaF_2 layers increases as reported in elsewhere. It is thought that this is because the strain is less effective once the film reached its critical thickness

Photoluminescence (PL) bleaching of Eu^{2+} was also investigated. The bleaching was observed from the $4f^6 5d \rightarrow 4f^7$ transition of Eu^{2+} doped in SLs and thin films. Bi-exponential decay was employed to describe the bleaching and the results fit well with the experimental data. Two channels of bleaching were initially considered; tunnelling and

trapping. Tunnelling is electron migration to the conduction band of CdF_2 while trapping is capture of electrons by defect centres in CaF_2. In either case the electrons are localised and do not recombine with Eu to sustain Eu^{2+} emission. The recovery of Eu^{2+} PL intensity was also observed by heating the SLs to higher temperatures. The activation energy was estimated as 70 $\pm$ 10 meV.

However direct evidence of Eu^{3+} being produced during the bleaching process of Eu^{2+} was not observed. It is therefore concluded that if Eu^{3+} is being produced then the centre of Eu^{3+} is either quenching or energetically remote from the detecting region of Eu^{3+} centres.

Combined excitation-emission spectroscopy (CEES) was employed to reveal Eu^{3+} centres in SLs. A novel I centre which is energetically close to the O centre was observed. The polarised excitation and emission spectroscopy confirmed that the $^5D_1$ and the $^7F_1$ multiplets are split into A_{2g} and E_g. The polarisation selection rules for trigonal C_{3v} symmetry matches exactly for the I centre. Hence the symmetry of the I centre is concluded as a trigonal. It is believe that an electron localised along [111] direction to Eu^{3+} in CaF_2 is responsible for the formation of the I centre. A possible transformation of the I centre to the O centre under additional thermal and UV excitation was also observed. This was interpreted as transfer of the electron to neighbouring cubes and this is supported by theoretical calculation. It appears that the I and the O centres are identical except for having an electron localised along the [111] direction for the I centre. Hence it is concluded that the site of Eu^{3+} is characterised by localised electrons. Sufficient information is not available on the inclusion of electrons in the SLs however the electrons are likely reside in the interface layers, that is the top and the bottom layers of CaF_2.

Based on the thermal excitation the thickness dependent delocalisation energies were calculated as between 16 $\pm$ 2 meV for 5 ML SL and 60 $\pm$ 4 meV for 2 ML SL. The delocalisation energy increased monotonically with decreasing thickness of CaF_2 layers. The delocalisation energy did not appear to be influenced by the thickness of CdF_2 layers as discussed in chapter 6. Accordingly it can be concluded that only the electrons inside CaF_2 are delocalised by additional thermal and UV excitation. Therefore the electrons in

CaF_2 layers are responsible for the formation of the I centre and contribute to the transformation of the I centre to the O centre.

A deformation of the crystal structure for thicker SLs was inferred from the observation of splitting in the O centre in the $^7F_0 \rightarrow {}^5D_1$ excitation of Eu^{3+}. The crystal field analysis suggests that the thick SLs (20 ML) are slightly distorted which allows for some mixture of trigonal symmetry to the O centre. However the splitting was not observed in thinner SLs. This was interpreted as the strain is being more effective for the 20 ML thick SLs.

8.2 Future work

It is apparent that the effective role of electrons is to primarily contribute to the formation of the I centre. However there is not sufficient information available on the incorporation of the electrons in the SL system. There are many factors that allow electrons to reside in CaF_2-CdF_2 SLs, such as annealing temperatures and even exposure to x-rays during XRD process. Hence it would be feasible to establish the growth parameters so that the electron incorporation is manipulated. CEES can follow to confirm that no I centre is observable when there are no electrons in the SL.

To verify the conclusion of the position of the electrons in CaF_2 layers, a series of isolated SLs (ISLs) can be grown. In such ISLs Eu^{3+} should be separated from the interface layers. For instance, for given CaF_2 layers, Eu^{3+} is only deposited in the middle of the layers and the interface layers contain no Eu^{3+}. As a consequence, only cubic centre of Eu^{3+} will be observed.

The absorption band of the electrons needs to be explored with more powerful light sources. As discussed in chapter 7, the absorption band peaking at 1.5 eV can be investigated by utilising the near IR Ti: Sapphire laser. Hence the position of the absorption bands with respect to the thickness of SLs will be determined. The transformation of the I and the O centre can also be verified in this region using the same laser.

The overall quality of the MBE grown samples was excellent. A mono layer thickness control of the growth technique enabled precise analysis of thickness dependent optical properties of the SLs. Further, without the powerful CEES technique the elucidation of the samples would not be possible. Throughout this study many questions were addressed regarding fundamental properties of SLs and thin films doped with Eu. Some further suggestions critical to understand the Eu^{3+} centres in SLs are also discussed. The author feels that successful research not only provides answers but poses questions so that research is stimulated and continued. In that sense this research was a success.

Appendix

Publications

1. V. A. Chernyshev, A. V. Abrosimov, S. V. Gastev, A. V. Krupin, A. E. Nikiforov, J. K. Choi, R. J. Reeves, S. M. Suturin and N. S. Sokolov. *Energy structure of Eu3+ centres in CdF_2–CaF_2:Eu superlattices on silicon*, J. Phys.: Condens. Matter **19** (2007) 395023 (9pp)

2. R. J. Reeves, J. K. Choi, S. V. Gastev, A. V. Krupin, K. R. Hoffman and N. S. Sokolov. *Laser spectroscopy of Eu^{3+} centers in CaF_2:Eu-CdF_2 Superlattices*, J. All. Comp. 451 (2008) 84-87

Appendix (1)

IOP PUBLISHING JOURNAL OF PHYSICS: CONDENSED MATTER
J. Phys.: Condens. Matter **19** (2007) 395023 (9pp) doi:10.1088/0953-8984/19/39/395023

Energy structure of Eu^{3+} centres in CdF_2–CaF_2:Eu superlattices on silicon

V AChernyshev[1], A V Abrosimov[1], S VGastev[2], A V Krupin[2], A E Nikiforov[1], J K Choi[3], R J Reeves[3], S M Suturin[2] and N S Sokolov[2]

[1] Ural State University, 51 Lenin Avenue, Ekaterinburg 620083, Russia
[2] A F Ioffe Physico-Technical Institute, 26 Polytechnicheskaya, St Petersburg 194021, Russia
[3] University of Canterbury, Rutherford Boulevard, Christchurch PB4800, New Zealand
E-mail: vladimir.chernyshev@usu.ru

Received 28 February 2007, in final form 1 May 2007
Published 30 August 2007
Online at stacks.iop.org/JPhysCM/19/395023

Abstract

Stark energy levels of Eu^{3+} ($4f^6$) ions in CdF_2–CaF_2:Eu epitaxial superlattices on Si have been measured by laser spectroscopy and calculated in an exchange charge model. Two types of centre have been considered in the CaF_2 layer: an 'interface centre', close to the CdF_2/CaF_2 interface, and a 'remote centre' located in the core of a layer. The influence of distortion, created by the silicon substrate, has been taken into consideration. The calculations confirmed a previously suggested 'electron' model of the interface centre.

Appendix (2)

Journal of Alloys and Compounds 451 (2008) 84–87

Laser spectroscopy of Eu^{3+} centers in CaF_2:Eu–CdF_2 superlattices

R.J. Reeves [a,*], J.K. Choi [a], S.V. Gastev [b], A.V. Krupin [b], K.R. Hoffman [c], N.S. Sokolov [b]

[a] *MacDiarmaid Institute for Advanced Materials and Nanotechnology, Department of Physics and Astronomy, University of Canterbury, New Zealand*
[b] *Ioffe Physico-Technical Institute, St Petersburg, Russia*
[c] *Department of Physics, Whitman College, Walla Walla, WA 99362, USA*

Available online 18 April 2007

Abstract

Combined excitation–emission spectroscopy was carried out to study Eu^{3+} centers in CaF_2:Eu–CdF_2 superlattices. Two distinctive centers were observed and assigned as remote (R) and interface (I). The energy level of the R center appeared to be close to the cubic center in a bulk crystal and mainly consists of Eu^{3+} ions located away from the SL boundaries. The relative intensity of the interface centers was very sensitive to the layer thickness and became more prominent in thinner layers indicating it is associated with Eu^{3+} ions in layers next to the SL boundary. A splitting of the $^5D_1$ manifold indicates the interface center has axial symmetry, which is suggested to come from a charge-compensating electron trapped in the conduction band of CdF_2 layer.

© 2007 Elsevier B.V. All rights reserved.

Keywords: RE^{3+}; Superlattices; Fluoride nanostructures

* Corresponding author.
E-mail address: roger.reeves@canterbury.ac.nz (R.J. Reeves).

0925-8388/$ – see front matter © 2007 Elsevier B.V. All rights reserved.
doi:10.1016/j.jallcom.2007.04.179